

nature
biomedical
engineering

**A wearable ultrasonic sensor
of blood pressure**

Monitoring of the central blood pressure waveform via a conformal ultrasonic device

Chonghe Wang^{1,10}, Xiaoshi Li^{2,10}, Hongjie Hu^{2,10}, Lin Zhang¹, Zhenlong Huang¹, Muyang Lin^{1,3}, Zhuorui Zhang¹, Zhenan Yin⁴, Brady Huang⁵, Hua Gong¹, Shubha Bhaskaran⁴, Yue Gu^{1,2}, Mitsutoshi Makihata⁶, Yuxuan Guo¹, Yusheng Lei¹, Yimu Chen¹, Chunfeng Wang^{1,7}, Yang Li¹, Tianjiao Zhang¹, Zeyu Chen⁸, Albert P. Pisano⁶, Liangfang Zhang¹, Qifa Zhou⁸ and Sheng Xu^{1,2,4,9*}

Continuous monitoring of the central blood pressure waveform from deeply embedded vessels such as the carotid artery and jugular vein has clinical value for the prediction of all-cause cardiovascular mortality. However, existing non-invasive approaches, including photoplethysmography and tonometry, only enable access to the superficial peripheral vasculature. Although current ultrasonic technologies allow non-invasive deep tissue observation, unstable coupling with the tissue surface resulting from the bulkiness and rigidity of conventional ultrasound probes introduces usability constraints. Here, we describe the design and operation of an ultrasonic device that is conformal to the skin and capable of capturing blood pressure waveforms at deeply embedded arterial and venous sites. The wearable device is ultrathin (240 μm) and stretchable (with strains up to 60%), and enables the non-invasive, continuous and accurate monitoring of cardiovascular events from multiple body locations, which should facilitate its use in a variety of clinical environments.

The variation of blood pressure (BP) waveforms contains abundant information about the dynamic cardiovascular status^{1,2}. Each one of the peaks and notches in the arterial BP waveform represents a specific left heart activity, and the characteristic morphology of the venous BP waveform is closely related to relevant right heart events³. Continuous monitoring of subtle changes in these vital signals can thus provide remarkable insights for cardiovascular disease diagnosis and prognosis⁴. Although monitoring vascular pulsation at peripheral sites is useful for specific symptoms, emerging evidence suggests that the central arterial and venous BP waveforms possess significantly more relevance to cardiovascular events than the peripheral BP (PBP)^{5–8}. First, major organs, including the heart, kidneys, lungs and brain, are directly exposed to the central arteries. Distending pressure in the large elastic arteries (such as the aorta and carotid arteries) is a vital determinant of the degenerative changes that characterize accelerated aging and hypertension⁹. Second, the amplification and reflection effect caused by the complexities of peripheral vascular resistance along the conduit artery (namely the stiffness mismatch between peripheral and central vessels) is hard to evaluate. This uncertainty often has an irregular and unpredictable influence on the PBP waveform, making it unsuitable for achieving reliable assessment of cardiovascular status¹⁰. Third, although the central blood pressure (CBP) waveform can sometimes be derived from the PBP waveform via a translational equation, demographic results indicate that clinical treatments, such as the use of BP-lowering drugs, can exert different effects on the PBP and CBP waveforms^{7,11}, leading to inaccurate recordings¹². This inaccuracy can cause errors in the assessment of

myocardial oxygen requirement¹³ and ventricular load and hypertrophy¹⁴, as well as disparities in the actions of different vasodilator agents¹⁵. Therefore, treatment decisions for cardiovascular diseases should be based on CBP rather than PBP waveforms¹⁶.

The gold standard for recording CBP waveforms in the carotid artery and jugular venous sites—cardiac catheterization (also known as cannulation)—involves implanting a fibre-based pressure sensor into the relevant vasculature¹⁷ (Supplementary Note 1). Despite its high accuracy, it causes patient suffering and increases the risk of infection, and thus is too invasive for routine inspections¹. Although there are several non-invasive methods, including the optical method (photoplethysmography (PPG) or volume clamp)¹⁸, tonometry^{4,19} and ultrasound wall-tracking, that can potentially monitor the CBP waveform, they suffer from a number of technical challenges. Specifically, PPG has insufficient penetration depth (<8 mm) for measuring the central vasculature, which is often embedded in a tissue thickness of more than 3 cm (ref. ²⁰). Other technical problems for PPG can be summarized as signal aliasing from venous and arterial pulsations²¹, susceptibility to heat and moisture²², and a high dependence on the blood composition being constant²³. Tonometry involves using strain sensors to detect vessel pulsation. This method relies on the efficiency of blood vessel flattening by the tonometer, so is only recommended for PBP measurements where a supporting bony structure is available that can provide a solid mechanical support²⁴. For this reason, its accuracy is largely degraded when measuring central vasculatures with no proximal supporting skeleton. This method is also adversely affected if the subject is obese, as this greatly dampens pulse wave propagation

¹Department of Nanoengineering, University of California San Diego, La Jolla, CA, USA. ²Materials Science and Engineering Program, University of California San Diego, La Jolla, CA, USA. ³School of Precision Instrument and Optoelectronic Engineering, Tianjin University, Tianjin, China. ⁴Department of Electrical and Computer Engineering, University of California San Diego, La Jolla, CA, USA. ⁵Department of Radiology, School of Medicine, University of California San Diego, La Jolla, CA, USA. ⁶Department of Mechanical and Aerospace Engineering, University of California San Diego, La Jolla, CA, USA. ⁷The Key Laboratory of Materials Processing and Mold of Ministry of Education, School of Materials Science and Engineering, School of Physics & Engineering, Zhengzhou University, Zhengzhou, Henan, China. ⁸Department of Ophthalmology and Biomedical Engineering, Viterbi School of Engineering, University of Southern California, Los Angeles, CA, USA. ⁹Department of Bioengineering, University of California San Diego, La Jolla, CA, USA. ¹⁰These authors contributed equally: Chonghe Wang, Xiaoshi Li, Hongjie Hu. *e-mail: shengxu@ucsd.edu

to the skin (Supplementary Notes 2 and 3 and Supplementary Figs. 1 and 2). The ultrasound wall-tracking technique, which has high penetrating capability, utilizes a high-speed imaging probe to track the pulsation of vasculature embedded in deep tissues²⁵. However, the imaging probe is highly sensitive to motion artefacts, which adds significant burden to its associated wall-tracking recognition algorithm (Supplementary Note 4 and Supplementary Fig. 3). Additionally, current ultrasound imaging probes are heavy and bulky, and to achieve a reliable acoustic coupling interface the probe must be held stable by the operator. This introduces inevitable compression to local vasculatures, changing their distension behaviour and leading to inaccurate recordings (Supplementary Fig. 4). Therefore, this method is not suitable for long-term monitoring.

Wearable devices with mechanical properties similar to the skin offer the capability for non-invasive, continuous monitoring of a variety of vital signs²⁶, including local field potentials²⁷, temperature²⁸, sweat content^{29,30} and skin hydration³¹. However, their applications have typically been limited to recording signals on the skin or in the shallow tissue under the epidermis. Here, we introduce an approach that allows the ultrasonic technology to be integrated in a wearable format. The ultrasonic waves can effectively penetrate human tissues up to a depth of 4 cm, which opens up a third dimension to the sensing range of current state-of-the-art wearable electronics. With similar mechanical properties to the skin and an ultrathin profile, the wearable ultrasonic device can ensure a conformal intimate contact with the curvilinear and time-dynamic skin surface, and continuously monitor the CBP of deep vasculatures without the operational difficulties or instabilities encountered by the other conventional approaches. This non-invasive, continuous and accurate monitoring of deep biological tissues/organs opens up opportunities for diagnosing and predicting a broad range of cardiovascular diseases in a wearable format.

Results

Device design and working principle. The device hybridizes high-performance rigid 1–3 piezoelectric composites with soft structural components (Fig. 1a and Supplementary Figs. 5 and 6). The anisotropic 1–3 composite possesses better acoustic coupling with the soft biological tissue than isotropic piezoelectric materials. By combining geometrical and electrical designs, our device can reach an ultrathin thickness of 240 μm , three orders of magnitude thinner than existing medical ultrasonic probes (Supplementary Note 5). The elastic and failure strain levels are up to 30% and 60%, respectively (Supplementary Figs. 7 and 8). The 1–3 piezoelectric composite with a thickness of 200 μm has a working frequency of 7.5 MHz (Supplementary Fig. 9), which enables a 400 μm axial resolution (see Methods and Supplementary Fig. 10) that is comparable with available medical ultrasonic probes at the same working frequency. The 1–3 composite has piezoelectric microrods embedded in a periodic configuration in a passive epoxy matrix, which substantially increases the longitudinal coupling coefficient k_{33} by suppressing shear vibrating modes. The rigid piezoelectric transducer element has a $0.9 \times 0.9 \text{ mm}^2$ footprint to allow sufficient penetration depth into the tissue, while adding minimal mechanical loading to human skin (Fig. 1b).

Bilayer stacking of polyimide (PI, 4 μm)/Cu (20 μm) (Fig. 1a, top left) was used to fabricate stretchable electrodes to interconnect a 4×5 array of transducers in the device (for the detailed fabrication process see Methods). The transducers can be individually addressed by 20 stimulating electrodes on the top and a common ground at the bottom. The array design aims to map the vessels' positions, thus enabling sensing and monitoring by a transducer overlying the targeted vessel, without tedious manual positioning (Supplementary Note 6 and Supplementary Fig. 11). The top stimulating electrodes and the bottom ground are routed to the same plane by a vertical interconnect access (VIA) for optimized mechanical robustness

and ease of electrical bonding (Fig. 1a, Supplementary Fig. 12 and Supplementary Note 7).

The working principle is illustrated in Fig. 1a bottom. Technically, the device can continuously record the diameter of a pulsating blood vessel, which can be translated into localized BP waveforms³². The BP waveform can be calculated as

$$p(t) = p_d \times e^{\alpha \left(\frac{A(t)}{A_d} - 1 \right)} \quad (1)$$

where p_d is the diastolic pressure, which is acquired on the brachial artery using a BP cuff, A_d is the diastolic arterial cross-section, and α is the vessel rigidity coefficient. Assuming that the artery is rotationally symmetrical, $A(t)$ can be calculated as

$$A(t) = \frac{\pi d^2(t)}{4} \quad (2)$$

where $d(t)$ is the diameter waveform of the target artery. The detailed working principle, resolution, calibration and validation of our device are described in the Methods and Supplementary Notes 8 and 9. When the device is softly laminated on the skin (Supplementary Fig. 13), each transducer can be individually activated and controlled with a power consumption of 23.6 mW. When the ultrasonic wave reaches interfaces, both transmission and reflection occur. The transmission wave with reduced intensity allows penetration into deeper layers of tissues. The reflection wave, which carries critical location information about the interfaces (for example, the anterior and posterior walls), can be sensed by the same transducer³³. The vessel diameter measurement results were validated by clinical ultrasonography (with excellent correspondence, 99.7%; Supplementary Fig. 14). At a high pulse repetitive frequency (2,000 Hz), time of flight (TOF) signals corresponding to the pulsating anterior and posterior walls can be accurately recorded by an oscilloscope with 2 GHz sampling frequency, which will appear as separate and shifting peaks in the amplitude mode (Fig. 1a, right bottom). The device can capture the pulsating blood vessel diameter dynamically with high spatial (axial resolution of 0.77 μm) and temporal (500 μs) resolution.

The entire device is encapsulated by a silicone elastomer with modulus on par with that of human skin. The elastomer is only 15 μm thick to provide a trade-off between mechanical robustness and sufficient acoustic emission performance (Supplementary Fig. 15 and Supplementary Note 5). The hydrophobic nature of the silicone elastomer provides a barrier to moisture, which protects the device from possible sweat corrosion (Fig. 1b). Owing to its soft mechanics, the as-fabricated ultrasound patch allows conformation to both developable (Fig. 1b, left) and non-developable (Fig. 1b, middle) surfaces. The device is also robust and can endure twisting and stretching (Fig. 1b, right), showing its high potential for skin integration applications.

Device characterization. The piezoelectric transducer converts electrical potential between the top and bottom electrodes to mechanical vibrations, and vice versa. The efficiency of this process is exhibited by the measured impedance and phase angle spectra in Fig. 2a, which show excellent piezoelectricity with a measured k_{33} value of 0.81, much higher than that of bulk PZT (~0.58)³³ due to its anisotropic high-aspect-ratio rod configuration (compared with isotropic bulk PZT³⁴). The transducer performance was evaluated on the wrist ulnar artery of a healthy male. The echo signal is shown in Fig. 2b, where the TOF of the two peaks corresponds to the positions of the anterior and posterior walls of the ulnar artery, respectively. Signal analysis in the time and frequency domains of the posterior wall is presented in Fig. 2c, which shows that the material has a central frequency of 7.5 MHz and has good sensitivity of

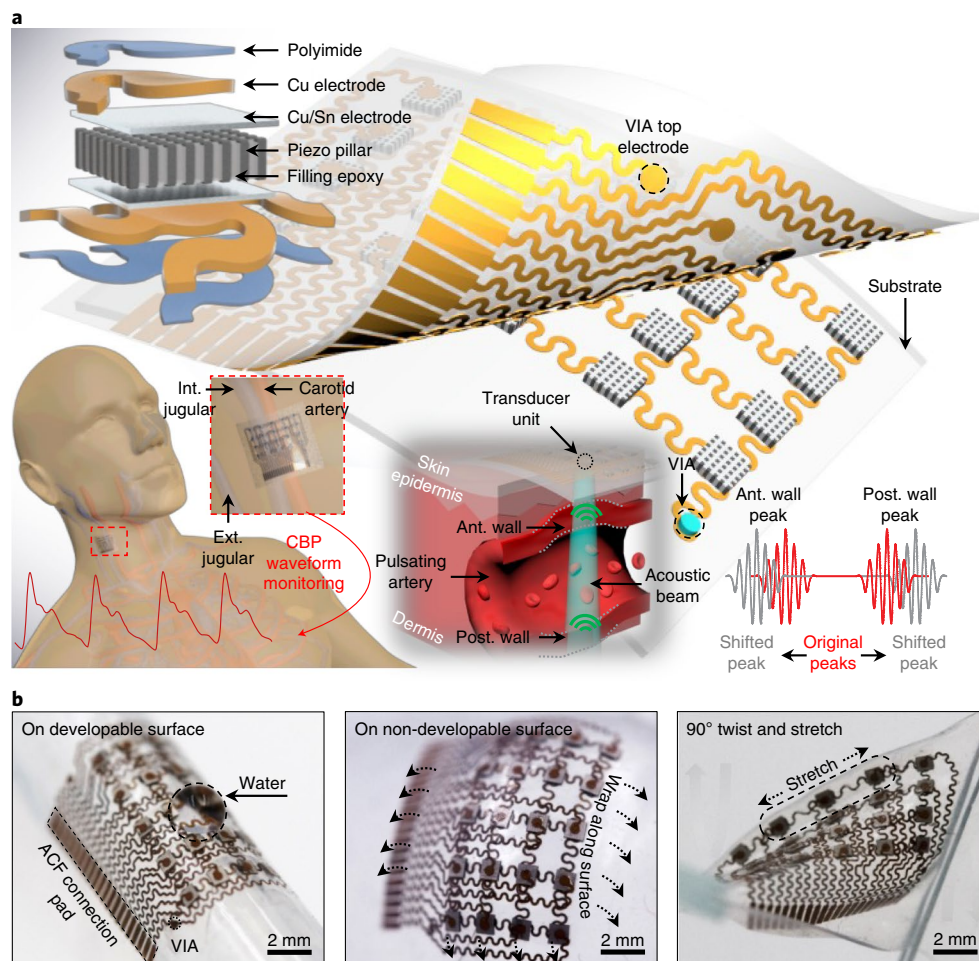


Fig. 1 | Design and working principle of the stretchable ultrasonic device. **a**, Schematics of the stretchable ultrasonic device, with key components labelled. The high-performance 1-3 composite with periodic piezoelectric rods embedded in an epoxy matrix suppresses shear vibration modes and enhances longitudinal ultrasonic penetration into the skin. The vertical interconnect access (VIA) connects the top and bottom electrodes, allowing co-planar anisotropic conductive film (ACF) bonding to the electrodes to enhance the robustness of the device. When mounted on the human neck, the device enables monitoring of CBP by capturing the pulsating vessel diameter of the carotid artery, internal jugular vein (int. jugular) and external jugular vein (ext. jugular) using the pulse-echo method, as illustrated in the bottom left graph. The device can locate the dynamic anterior (ant.) and posterior (post.) walls of the vessel using a high-directivity ultrasonic beam (bottom middle graph). The corresponding shifting echo radiofrequency signals reflected from the anterior and posterior walls are shown bottom right. **b**, The device conforming to complex surfaces and under mixed modes of stretching and twisting, demonstrating the mechanical compliance and robustness of the device. The large contact angle of the water droplet on the device in the left panel shows the hydrophobic properties of the silicone encapsulation materials that can be used as a barrier to moisture and sweat.

32% at -6 dB bandwidth (see Methods), with a peak to peak voltage of ~ 100 mV. Prediction of the beam pattern (Matlab R2016b, TAC_GUI toolbox) of our stretchable ultrasonic device is shown in Fig. 2d. The results show that, in the longitudinal direction, the conformal probe has excellent beam directivity and sufficient penetration for deep tissue detection, reaching a penetration depth of up to 40 mm (with a piezoelectric transducer size of 0.9×0.9 mm²). The larger the piezoelectric material size, the deeper the ultrasonic wave can penetrate (Supplementary Fig. 16). The 1-3 composite has low acoustic impedance (15.3 MRayl), which provides excellent acoustic coupling with the human skin. Additionally, the bottom circular electrode diameter is designed to be 0.6 mm to balance practical bonding robustness and impedance matching (Supplementary Fig. 17).

The elastomeric matrix with iterative stretchable circuit designs and ultrathin encapsulation assemblies provides exceptionally conformal contacts to the human skin under various deformation modes (Supplementary Fig. 18). The device can be reversibly stretched up to 30% in the x direction and 25% in the y direction. The maximum stretchability can reach up to 60% in the x

direction and 50% in the y direction (Fig. 2e). These mechanical characteristics enable robust and seamless contact with the skin (Supplementary Note 10), given the fact that the human skin typically exhibits a linear elastic response to tensile strain of $<20\%$ (ref. 35). The electrical performance of the device remains stable under stretching and in a moist environment (Supplementary Fig. 19). Cell viability testing under controlled ultrasound intensity is shown in Fig. 2f and Supplementary Fig. 20. The fibroblast cells (HFF-1) were cultured under ultrasonic wave emission from our conformal probe with a 100% survival rate after 16 h of continuous exposure, showing the excellent biocompatibility of our device (for detailed cell information see Methods).

Performance validation. A conformal and intimate contact between the device and the human skin is paramount for robust performance of the device. Figure 3a presents continuous measurements on the radial artery using our device and a commercial tonometer (the non-invasive gold standard for BP waveform measurements) with the wrist bent to different angles. In this scenario the tonometer

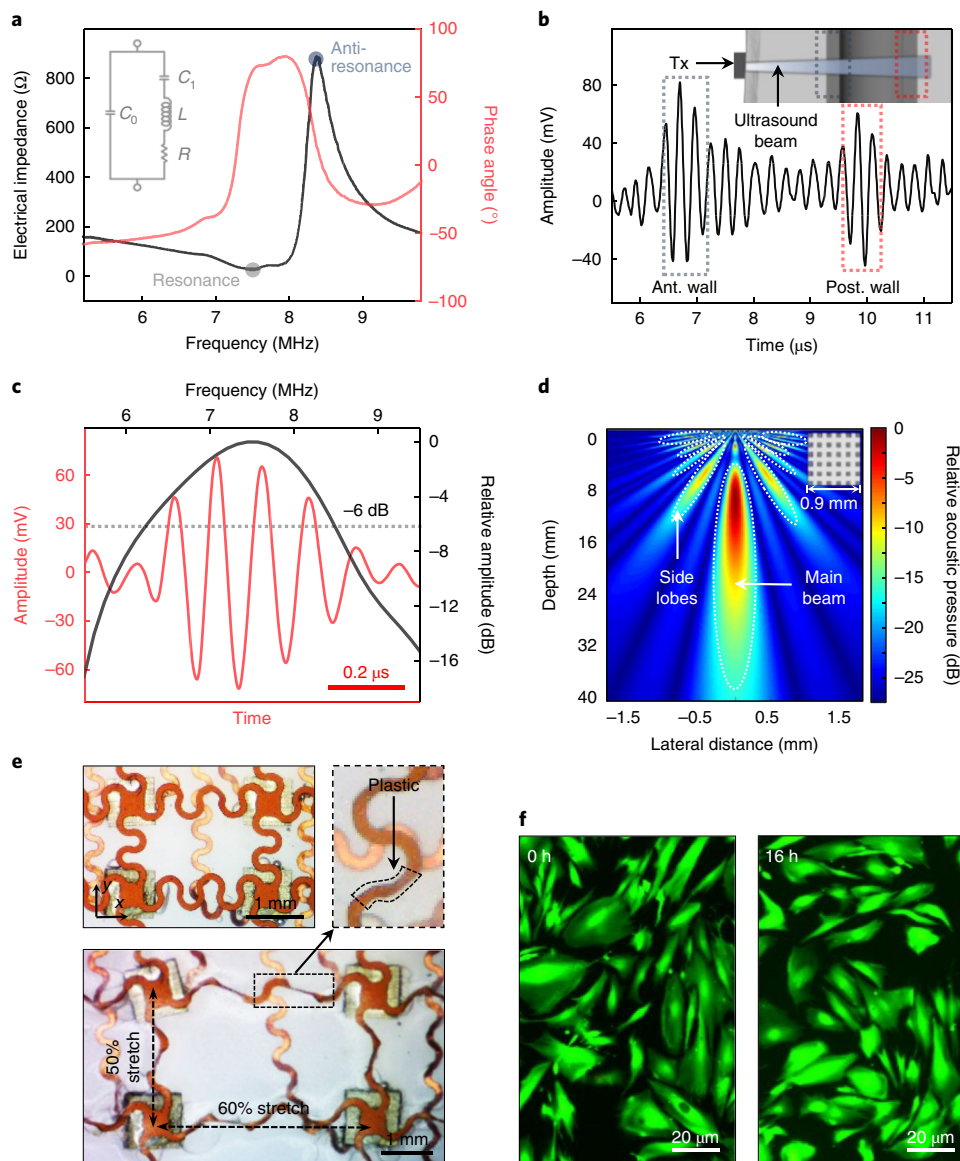


Fig. 2 | Electrical, mechanical, acoustic and biocompatibility characterizations of the conformal ultrasonic device. **a**, Impedance and phase angle spectra of the 1-3 composite, showing excellent piezoelectricity. The resonant and anti-resonant frequencies are labelled with shaded circles. Left inset: equivalent RLC circuit diagram of the piezoelectric transducer. At the resonant frequency, the impedance of the equivalent circuit is at a minimum, which will be the most power efficient. At the anti-resonant frequency, the impedance of the equivalent circuit is at a maximum, and the transducer will have the largest damping. **b**, Received ultrasonic signals on the ulnar artery, with two clear echo peaks from the anterior (ant.) and posterior (post.) vessel walls. Inset: schematic diagram representing the transducer and the ulnar artery to show echo peaks aligned with the anterior and posterior vessel walls. Tx, transducer. **c**, Time- and frequency-domain characterizations of the signal in **b** (posterior-wall peak), showing excellent signal quality and bandwidth (dashed line), indicating the high sensitivity of the transducer. **d**, Simulated acoustic emission profile of a piezoelectric material with a size of $0.9 \times 0.9 \text{ mm}^2$ (inset) with excellent beam directivity and penetration depth ($>4 \text{ cm}$). **e**, Biaxial tensile testing of the device with stretchability up to 60% in the x direction and 50% in the y direction without fracture. The zoomed-in image of the dashed box shows the slight plastic deformation when the biaxial strain is larger than 30% in the x direction. **f**, Fluorescent images of the fibroblast cells before (left) and after 16h continuous exposure to the ultrasound generated by the conformal ultrasonic device. The 100% survival rate of the cells proves the excellent biocompatibility of the conformal ultrasonic device.

needs to be held tightly by the operator to remain stable on the wrist, resulting in great pressure ($\sim 100 \text{ Pa}$) on the skin, which causes severe irritation (Fig. 3b) and also significant waveform distortion and erroneous readings (Fig. 3c). However, our device self-adheres to the skin and applies minimal pressure ($\sim 5 \text{ Pa}$) due to its ultralight weight (0.15g) and skin-like modulus. This enables the device to not only monitor over long periods without any discomfort, but also allows relatively stable and continuous recording, even during motion. Correlation curves of the two devices are shown in Fig. 3d. Most importantly, our device has smaller relative

measurement uncertainty (1%), higher measurement precision (within 2 mmHg) and higher accuracy (grade A) than the commercial equipment (Supplementary Note 11, Methods and Supplementary Figs. 21 and 22). Furthermore, the tonometer is highly operator-dependent, which is reflected by the fact that a tiny offset from the central arterial axis or moderate holding forces of the tonometer probe will introduce tremendous recording error into the BP waveform (Supplementary Figs. 23 and 24). Our conformal ultrasonic array with its ultralight weight and vessel positioning capability thus exhibits substantial advantages over applanation tonometry.

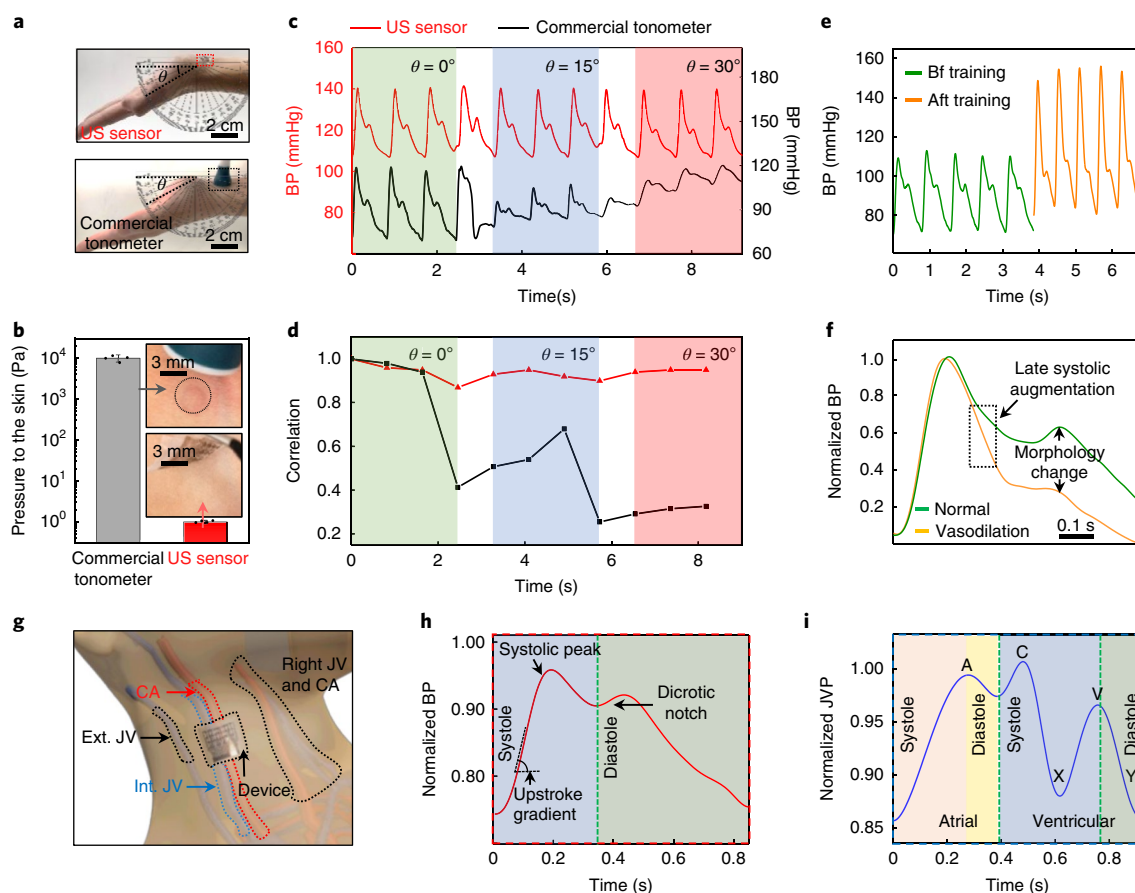


Fig. 3 | Comparison between the conformal ultrasound sensor and a commercial tonometer, exercise haemodynamics monitoring and central arterial and venous pulse measurements. **a**, Continuous measurements of radial pulse waveforms by both ultrasound (US) sensor (top) and a commercial tonometer (bottom) under the same conditions. **b**, Comparison of pressure levels applied to the skin during measurements. Insets: images showing skin irritation from the tonometer and conformal ultrasound sensor. Dots represent all data points. Error bars represent \pm s.d. ($N=4$). **c**, Comparison of BP waveforms measured continuously when the wrist is bent at a rate of $\sim 15^\circ \text{ s}^{-1}$, showing the robust performance of the conformal device. Different postures from 0° to 30° are shown in different shades. **d**, Autocorrelation of the waveforms in **c**, showing the conformal ultrasound device can maintain stable measurements during motion. **e**, Pulse waveforms on the radial artery before (bf) and after (aft) exercise, showing the changes in absolute pressure values and waveform morphologies. **f**, Pulse waveforms averaged from 10 continuous periods and normalized to the same diastolic and systolic pressure values to demonstrate the change in morphologies caused by vasodilation. **g**, Illustration of the ultrasound sensor measurement locations marked with arrows: left carotid artery (CA), external jugular vein (ext. JV) and internal jugular vein (int. JV). The right jugular vein and carotid artery are also highlighted. **h**, A typical pulse waveform measured from the carotid artery, directly correlated to the left atrial and ventricular events. Different phases and characteristic morphologies are marked. **i**, A typical pulse waveform from the internal jugular vein, directly correlated to the right atrial and ventricular activities. Different phases and characteristic morphologies are marked.

More interestingly, the conformal ultrasound probe enables a gel-free working mode. Traditional ultrasonic transducers rely on ultrasound gel to eliminate interfacial air gaps between the probe and the skin to achieve good acoustic coupling. The gel is unpleasantly cold and has to be reapplied frequently to prevent it from drying out. In this device, we add a thin layer of silicone as the acoustic coupling layer. The silicone is sticky and has an ultralow modulus ($\sim 5 \text{ kPa}$) to ensure intimate contact with the skin without applying any gel. The quality of the acquired signals and waveforms is comparable to those acquired with the gel (Supplementary Fig. 25 and Methods). Moisture and human sweat, which significantly influence PPG measurements, do not affect the performance of the conformal ultrasound device (Supplementary Fig. 26). The design leads to a device with remarkable durability, allowing highly reproducible testing results after four weeks (Supplementary Fig. 27).

Dynamic haemodynamics monitoring. Owing to its excellent mechanical compliance and light weight, our device can maintain

intimate and stable contact with the human skin, both mechanically and acoustically, in different body postures with pure van der Waals force (Supplementary Fig. 28). During exercise, muscles require increased delivery of nutrients and oxygen, and so the cardiac output increases to meet the need³⁶. On the one hand, the vessels dilate to increase delivery, so vascular resistance and reflection are reduced. On the other hand, the heart rate and systolic strength increase to boost the cardiac output. Heart rates measured on the radial artery during resting ($\sim 75 \text{ min}^{-1}$) and immediately after exercise ($\sim 112 \text{ min}^{-1}$) are shown in Fig. 3e. The BP waveform has a higher systolic peak due to the stronger ventricular systole required to obtain more substantial cardiac output³⁷. The averaged waveform morphology changes before and after intense exercise are presented in Fig. 3f (normalized to the same systolic and diastolic pressure values), which show a steep drop of the systolic peak after physical training due to the vasodilation-induced vascular resistance decrease. It is worth noting that we need to calibrate our device before and after any exercise that will significantly change the

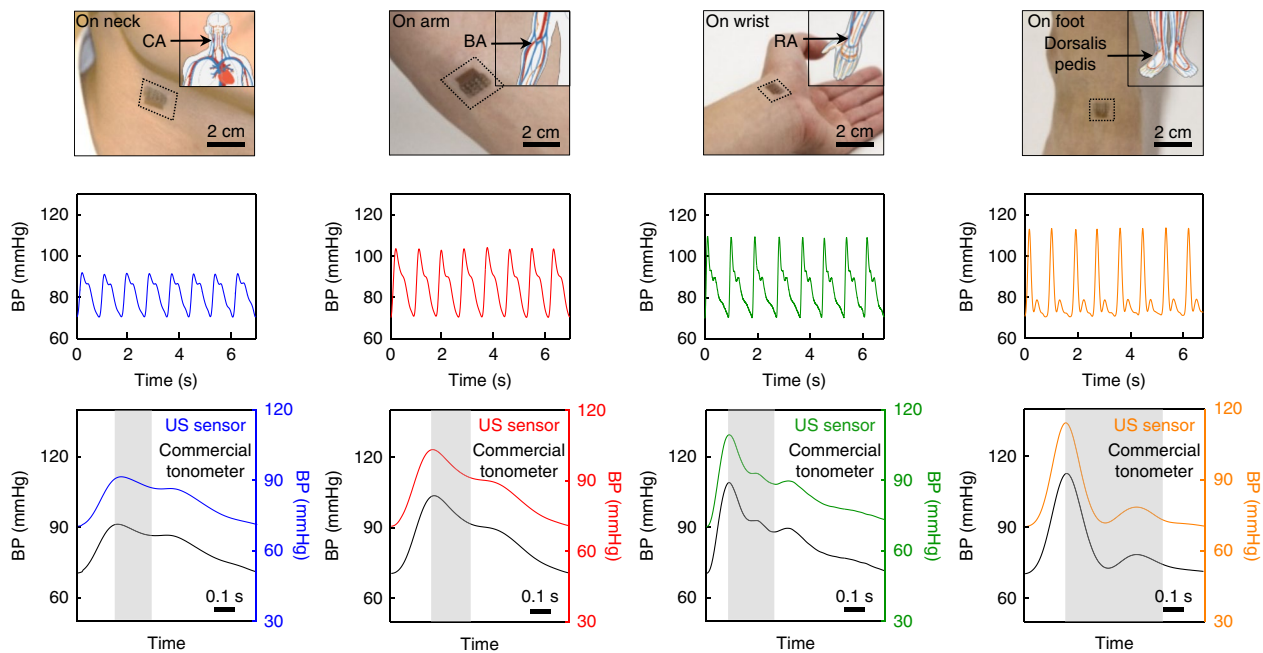


Fig. 4 | BP measurements from the central to peripheral arteries and validation using a commercial tonometer. Measurement positions (top row), collected arterial pressure waveforms (middle row) and the BP waveforms of one period compared with the results from the tonometer (bottom row). Columns (left to right): carotid artery (CA), brachial artery (BA), radial artery (RA) and pedal artery (dorsalis pedis), respectively, showing an increase in amplification effect by progressive vascular resistance, longer interval time between the systolic peak and the dicrotic notch (grey areas), higher systolic pressure and higher upstroke gradient (the slope of the BP waveform at the beginning of the upstroke).

diastolic pressure. However, we can observe the vessel dilation and vascular resistance decrease by comparing the normalized waveforms, regardless of the absolute BP values.

CBP recording. From a pathophysiological perspective, the CBP waveform is a crucial, and the most direct, predictor of main cardiovascular events⁵. Monitoring such events in a continuous and long-term manner can lead to remarkable advancements in cardiovascular disease diagnosis and prevention⁶, which are yet to be realized with existing medical tools (Supplementary Note 12). We demonstrate highly accurate direct measurements of central vasculature pulsating behaviour in deep tissues, including the carotid artery and internal and external jugular veins. Schematic illustrations of the measurement configuration are provided in Fig. 3g. The carotid artery (CA, ~25 mm under the skin, with slight individual variations³⁸, near the central aorta) carries a significant amount of blood from the left ventricle (LV) and left atrium (LA) to the rest of the body. A typical period of the carotid artery BP waveform measured by our device shows a clear systolic peak and a dicrotic notch (Fig. 3h). The former indicates ventricular systole and the latter suggests closure of the aortic valve. A detailed CBP measurement calibration is provided in Supplementary Note 9. The corresponding validation using a commercial tonometer exhibits remarkable correspondence (Supplementary Fig. 29). The blood flow sequence in the central cardiovascular system and direct relationship between the central vessels and heart are shown in Supplementary Fig. 30. A detailed clinical interpretation of arterial BP waveforms is illustrated in Supplementary Fig. 31 and discussed in Supplementary Note 13.

The internal jugular vein, carrying venous blood to the right atrium and right ventricle and finally to the lung, reflects the right heart activity. A typical jugular venous pressure waveform, measured by our device, is shown in Fig. 3i. The normalized pressure waveform was obtained by the volume assessment method³⁹. Associated algorithms and equations for this method are discussed in detail in Supplementary Note 9. The jugular venous waveform

comprises three characteristic peaks—A (atrial contraction), C (tricuspid bulging, ventricular contraction) and V (systolic filling of the atrium)—and two descents—X (atrial relaxation) and Y (early ventricular filling). These components correspond to various events during each cardiac cycle. The jugular venous waveform measured by a clinical colour Doppler imaging machine on the same subject is presented in Supplementary Fig. 32, and shows the corresponding A, C and V peaks and X and Y descents. The jugular venous distension (JVD), seen as a vessel bulging on the neck created by deep exhalation of the subject (Supplementary Fig. 33), can predict right-side heart failure⁴⁰. More detailed discussions are provided in Supplementary Note 13.

BP waveform monitoring from central to peripheral. Owing to the amplification effect—namely progressive vascular resistance, stiffness and impedance mismatch between central and peripheral vessels—the arterial pressure waveform varies from central to peripheral⁶. Although the diastolic and mean arterial pressures are relatively constant, systolic pressure can be up to 40 mmHg higher in the peripheral than the central artery⁴¹. This amplification effect on various parts of the body contains abundant information related to age, gender, height, heart rate and systematic diseases affecting the vasculature⁴². These data, if carefully collected, can be critical for improving the efficacy of diagnosis and prognosis of cardiovascular diseases⁴³. However, in current clinical settings, such valuable data and signals can only be obtained by a professional clinician in a quite infrequent manner. The challenges for existing approaches are discussed in Supplementary Note 12.

Our device allows observation of this intriguing phenomenon. The amplification effect will increase as we move from the large and highly elastic central arteries (for example, the carotid) to the small and stiff peripheral arteries (for example, the radial and dorsalis pedis) (Fig. 4, first row, and Supplementary Fig. 34). This phenomenon is due to backward propagation of pulse waves generated at arterioles. At central sites, the reflected pulses need to travel a long

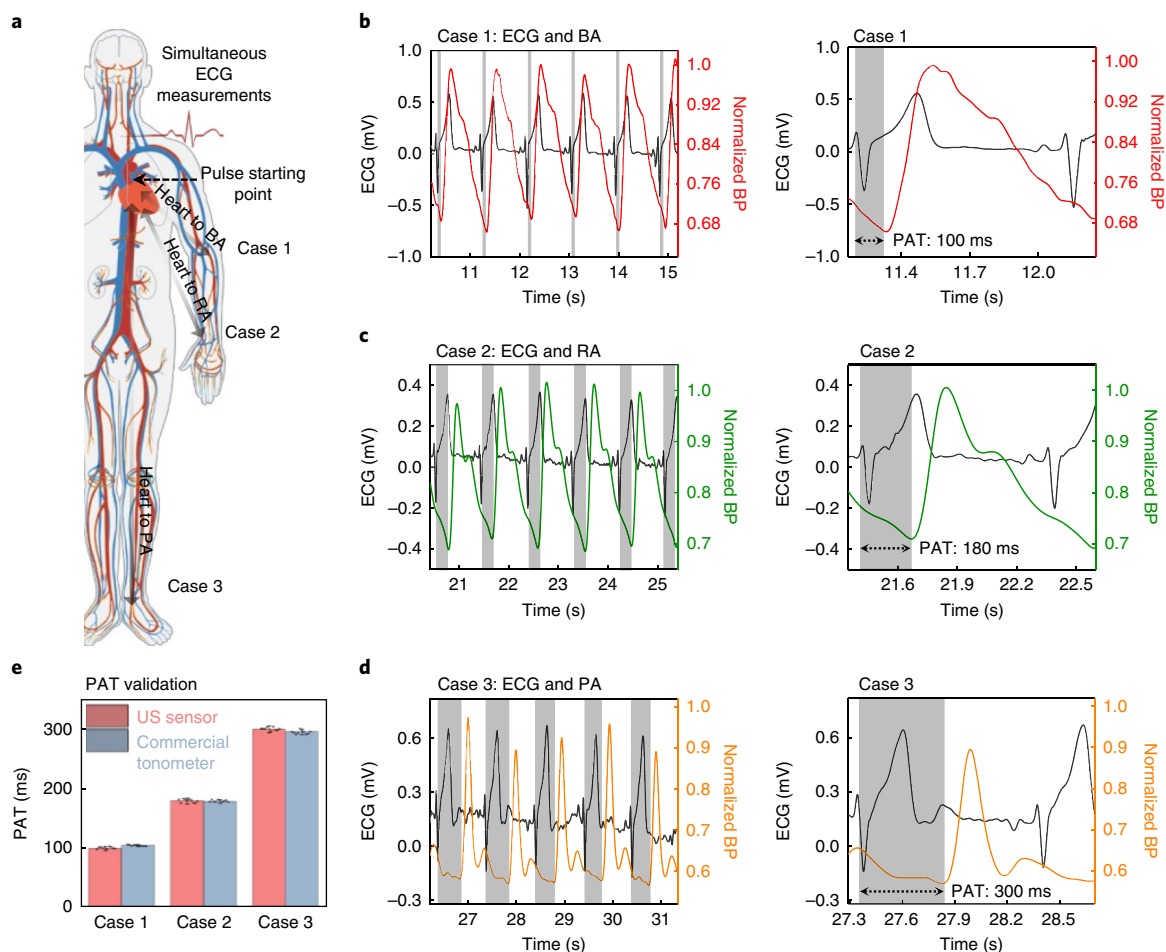


Fig. 5 | ECG correlation-based PWV calculation to evaluate arterial stiffness. **a**, Illustration of measurement positions for the three cases from the central to peripheral arteries, with simultaneous ECG measurements. BP waveforms are normalized based on systolic pressure. **b**, Case 1: simultaneous measurement of ECG and BP at the brachial artery (BA). **c**, Case 2: simultaneous measurement of ECG and BP at the radial artery (RA). **d**, Case 3: simultaneous measurement of ECG and BP at the pedal artery (PA, dorsalis pedis). The graphs in the right panels of **b–d** show the PATs, indicated by the grey areas, for each case. **e**, Comparison of PAT results for the conformal device and tonometer. Dots represent all data points. Error bars represent \pm s.d. ($N=10$).

distance, so they add to the CBP waveform in a misaligned manner. At peripheral sites, however, they travel a much shorter distance, so instantly contribute to the peripheral BP waveform in a way that is time-aligned. Therefore, the more peripheral the artery is, the higher the amplification/augmentation will be (Fig. 4, second row). To validate this amplification effect, we used a commercial tonometer to test the same subject. Remarkably corresponding results are shown in the third row of Fig. 4. An exciting feature contributed by this direct diameter measurement approach is that it allows observation of this amplification phenomenon and derivation of accurate pulse pressure values from multiple body parts simultaneously from diastolic pressure at only the brachial site, with no site mismatch (Supplementary Note 14 and Supplementary Fig. 35). The upstroke gradient increases as a result of the pressure amplification (Supplementary Fig. 36 and Supplementary Note 15).

Another notable feature of the BP waveforms is the progressive time interval between the systolic peak and the dicrotic notch, which is illustrated by the grey areas in Fig. 4. When the pressure wave travels down from the central arteries, its magnitude increases due to impedance mismatches encountered on the way, creating a reflected wave that travels back to the heart during late systole and early diastole. This reflection wave takes a longer time to travel from a location that is more distant from the heart, and thus contributes to an increase in the time interval between the systolic peak and the

dicrotic notch (grey areas in the waveforms in Fig. 4, third row)⁴⁴. The capability of capturing those systemic variations demonstrates the device’s potential for accurate clinically relevant diagnosis.

Electrocardiogram correlation for arterial stiffness calculation. The characteristics of arterial pulse propagation have a strong relationship with vascular stiffness, which is one of the key determinants of cardiovascular risks⁴⁵. Among the vascular parameters, pulse wave velocity (PWV) is the most accessible and reliable way to evaluate arterial stiffness (Supplementary Note 16) and can be calculated as⁴⁶

$$PWV = \frac{D}{PAT} \tag{3}$$

where D is the distance between the electrocardiogram (ECG) sensor and the ultrasonic sensor. Schematics of the measurements are presented in Fig. 5a, which shows simultaneous measurements of the ECG and pulse arrival times (PATs) at three different sites—brachial, radial and dorsalis pedis. Figure 5b–d presents the ECG correlation results for case 1 (brachial artery, Fig. 5b), case 2 (radial artery; Fig. 5c) and case 3 (pedal artery, Fig. 5d), where the ECG is measured on the chest for all cases (Supplementary Fig. 37). As seen in Fig. 5b–d, the PWV in case 1 is 5.4 m s^{-1} ($D = 54 \text{ cm}$, time difference = 100 ms),

in case 2 it is 5.8 m s^{-1} ($D=104 \text{ cm}$, time difference = 180 ms) and in case 3 it is 5.3 m s^{-1} ($D=159 \text{ cm}$, time difference = 300 ms). The PWV measurements are highly reproducible (Supplementary Fig. 38) and were validated by the commercial equipment, as shown in Fig. 5e and Supplementary Fig. 39 (for detailed testing conditions and measurement methods see Methods).

Discussion

We have demonstrated a new class of conformal and stretchable ultrasonic devices that offer non-invasive, accurate and continuous monitoring of vital signs from well below the human skin, adding a new dimension to the sensing range of conventional stretchable electronics. This device exploits strategic material integration and advanced microfabrication techniques to achieve both state-of-the-art functions and suitable mechanical compliance that allows intimate coupling with the human skin. This device can be used to capture a series of key features in the central blood vessels with reliable performance, and has strong clinical implications.

Device performance and functionality could be improved. The measurement of absolute blood pressure using PAT is feasible by ECG correlation, bypassing the need for recalibration with the BP cuff (Supplementary Note 16). Furthermore, ultrasonic imaging on the human body could provide accurate quantification for the vessel cross-sectional area to calculate the BP waveform, which is particularly valuable for CVP measurements on the irregularly shaped jugular veins. Additionally, integrating post-end functions such as electronic control, signal processing, waveform pattern recognition, wireless communications and power sources in a stretchable and lightweight format would significantly enhance device wearability. To reduce the system-level power consumption, a lower-sampling-rate analog-to-digital converter could be used to decrease the power budget of data transmission. A phased-array control algorithm could also be implemented to allow focusing and steering of the ultrasonic beam inside the human body.

Methods

Fabrication of the stretchable ultrasonic device. The fabrication can be summarized into three parts: (1) stretchable circuit patterning; (2) transfer printing; (3) soft elastomeric packaging (Supplementary Fig. 40). First, a Cu foil ($20 \mu\text{m}$ thick, MicroThin) was spin-coated with PI from poly(pyromellitic-dianhydride-co-4,4'-oxydianiline)-amic acid solution. This process was performed at 4,000 r.p.m. for 60 s. The foil was soft baked on a hotplate at 110°C for 3 min and 150°C for 1 min, and then cured in a nitrogen oven at 300°C for 1 h. A glass slide coated with a layer of polydimethylsiloxane (PDMS, Sylgard 184 silicone elastomer, 20:1) served as the substrate to laminate the Cu foil with the PI layer in contact with the PDMS. UV ozone surface activation for 3 min was used to increase the bonding between the PI and PDMS. A laser ablation system (Supplementary Fig. 41; 0.342 mJ power, 900 kHz pulse repetition frequency, 300 mm s^{-1} laser cutting speed and 241 ns pulse width) was then utilized to create the circuit pattern with the highest resolution (Supplementary Fig. 42). Using water-soluble tape (AquaSol), the circuit was transferred onto a $15\text{-}\mu\text{m}$ -thick Eco-flex (0030, Smooth-On) substrate spin-coated on a poly(methyl methacrylate)-decorated glass slide (Supplementary Fig. 43). After removing the water-soluble tape, the circuit surface was cleaned using flux to remove surface oxidation (Supplementary Fig. 44) created during the laser ablation process to increase the welding strength. Welding to the top and bottom electrodes was achieved with solder paste at 150°C for 5 min. The device was encapsulated with Eco-flex. Curing was performed at room temperature for 2 h, and the glass slides were then peeled off. Finally, spin-coating an additional layer of Silbione on the Ecoflex substrate facilitated removal of the interfacial gaps and thus the necessity for the gel during testing.

Poling of the 1–3 composite. Poling the 1–3 composite (Smart Material Corp.) increased its piezoelectric coefficient and the electromechanical coupling factor of the composite⁴⁷. Poling involved using an electric field to align the dipoles of the piezoelectric materials, which enhanced the piezoelectricity and performance of the device⁴⁸. The polarizing hysteresis loop (Supplementary Fig. 45) was measured in silicone oil. Poling of the device was implemented at 1.2 kV cm^{-1} (d.c.) for 15 min. An excessive poling electric field caused breakdown of the piezoelectric materials, thus reducing the signal strength (Supplementary Fig. 46).

Measurement and data analysis of the BP waveforms. The BP waveform measurement was carried out on a healthy male aged 22 years, under the approval by the Institutional Review Board (IRB) of the University of California, San

Diego (IRB no. 170812). Written informed consent was obtained from all human subjects. All measurements were carried out on the same subject when sitting. The measurement set-up is illustrated in Supplementary Fig. 47. A layer of Silbione was applied to the bottom of the device surface to enable gel-free measurements. Signal analysis was based on the TOF, which was a gauge of the time interval between the signal peak and zero time point. The TOF was used to calculate the propagation distance by multiplying by the speed of ultrasound in the specimen. The device was activated by an ultrasonic pulser (Olympus 5077 PR) at 100 V, using the transmit/receive mode. The pulse repetitive frequency was 2,000 Hz. The echo signal was received by an oscilloscope (Picoscope 6404) with a temporal resolution of $500 \mu\text{s}$, which allowed precise vessel wall-tracking (Supplementary Note 8). Discussions of the measurement principle, resolutions, uncertainty, accuracy and precision are provided in Supplementary Notes 8 and 11 and Supplementary Figs. 22 and 48–50. The circuit enabling simultaneous measurement of pulse pressure on various sites is described in Supplementary Note 14 and Supplementary Fig. 51. A clinical colour Doppler machine (Mindray DC 7) was used to confirm the characteristic peaks in the venous waveform. The BP waveform measurement results were validated by a SphygmoCor EM3 tonometer.

ECG correlation. The ECG correlation to the BP waveforms at different locations was assessed on the same subject (when sitting), consecutively, with a 2 min interval, to guarantee the subject had a relatively constant BP value and arterial stiffness. The longest duration of skin integration on the same skin region was $\sim 2 \text{ h}$. No allergic reactions, redness or damage to the skin was observed in any of our studies. The diastolic pressure was calibrated using a commercial BP cuff (Smart Logic Technology, 6016) before each monitoring period. The tested subject maintained a stable physiological and psychological status to guarantee stable levels of BP and vasculature stiffness. A detailed discussion of PAT, pulse transit time (PTT) and PWV is provided in Supplementary Fig. 52 and Supplementary Note 16.

Transducer selection, bandwidth and resolution characterization. We chose piezoelectric ultrasound transducers (PUTs) instead of capacitive micromachined ultrasound transducers (cMUTs) or piezoelectric micromachined ultrasound transducers (pMUTs), because of the low cost and ease of fabrication of PUTs. More detailed considerations are presented in Supplementary Note 5 and Supplementary Fig. 53. The transducer bandwidth (32%) was calculated by dividing the frequency range (2.4 MHz) by the central frequency (7.5 MHz). The axial resolution characterization exploited a thin metal wire suspended at the centre of a beaker filled with water. A 1×10 linear array of transducers was fabricated and attached to the beaker wall parallel to the ground. All signals from the ten transducer elements were acquired and combined with one transducer as the transmitter and the other as the receiver (for example, 1T2R, 1T3R... 1T10R; 2T1R, 2T3R... 2T10R;...; 10T1R, 10T2R... 10T9R). A total of 90 signals were used with the delay-and-sum algorithm to reconstruct the image (Supplementary Fig. 10c). The obtained image had low-level side lobes resulting from the reconstruction algorithm and the limited number of elements used for imaging.

Cell viability assay under ultrasound exposure. The HFF-1 cells were purchased from American Type Culture Collection (ATCC) and cultured in Dulbecco's modified Eagle's medium (DMEM, Gibco) supplemented with 10% fetal bovine serum (FBS, Gibco) and 1% penicillin/streptomycin (Gibco) at 37°C and 5% CO_2 . The HFF-1 cells were subcultured and seeded into a 24-well plate at a density of $1 \times 10^4 \text{ ml}^{-1}$ and incubated for another 24 h. No antibodies were used in the experiment. An ultrasound beam at a frequency of 7.5 MHz was applied to the bottom of the culture plate. After 2, 6 and 16 h of ultrasound exposure, the cells were stained with calcein AM (Invitrogen, 3M, excitation/emission = 488 nm/525 nm) and propidium iodide (Invitrogen, 3M, excitation/emission = 530 nm/620 nm) for 15 min, and then imaged under fluorescence microscopy (EVOS, ThermoFisher Scientific). For the positive control group, the cells were treated with 75% ethanol for 10 min.

Reporting Summary. Further information on research design is available in the Nature Research Reporting Summary linked to this article.

Data availability

The main data supporting the findings of this study are available within the Article and its Supplementary Information. The raw data generated in this study are available from the corresponding author upon reasonable request.

Received: 21 November 2017; Accepted: 3 August 2018;
Published online: 11 September 2018

References

- McGhee, B. H. & Bridges, E. J. Monitoring arterial blood pressure: what you may not know. *Crit. Care Nurse* **22**, 60–79 (2002).
- Avolio, A. P., Butlin, M. & Walsh, A. Arterial blood pressure measurement and pulse wave analysis—their role in enhancing cardiovascular assessment. *Physiol. Meas.* **31**, 275–290 (2009).

3. Kumar, A. et al. Pulmonary artery occlusion pressure and central venous pressure fail to predict ventricular filling volume, cardiac performance, or the response to volume infusion in normal subjects. *Crit. Care Med.* **32**, 691–699 (2004).
4. Dagdeviren, C. et al. Conformable amplified lead zirconate titanate sensors with enhanced piezoelectric response for cutaneous pressure monitoring. *Nat. Commun.* **5**, 4496–4506 (2014).
5. Safar, M. E. et al. Central pulse pressure and mortality in end-stage renal disease. *Hypertension* **39**, 735–738 (2002).
6. Trudeau, L. Central blood pressure as an index of antihypertensive control: determinants and potential value. *Can. J. Cardiol.* **30**, 23–28 (2014).
7. McEniery, C. M., Cockcroft, J. R., Roman, M. J., Franklin, S. S. & Wilkinson, I. B. Central blood pressure: current evidence and clinical importance. *Eur. Heart J.* **35**, 1719–1725 (2014).
8. Ding, F.-H. et al. Validation of the noninvasive assessment of central blood pressure by the SphygmoCor and Omron devices against the invasive catheter measurement. *Am. J. Hypertens.* **24**, 1306–1311 (2011).
9. Agabiti-Rosei, E. et al. Central blood pressure measurements and antihypertensive therapy. *Hypertension* **50**, 154–160 (2007).
10. Bruyndonckx, L. et al. Methodological considerations and practical recommendations for the application of peripheral arterial tonometry in children and adolescents. *Int. J. Cardiol.* **168**, 3183–3190 (2013).
11. Avolio, A. P. et al. Role of pulse pressure amplification in arterial hypertension. *Hypertension* **54**, 375–383 (2009).
12. Williams, B. et al. Differential impact of blood pressure-lowering drugs on central aortic pressure and clinical outcomes. *Circulation* **113**, 1213–1225 (2006).
13. Moffitt, E. A. et al. Rate-pressure product correlates poorly with myocardial oxygen consumption during anaesthesia in coronary patients. *Can. J. Anaesth.* **31**, 5–12 (1984).
14. Roman, M. J. et al. Relations of central and brachial blood pressure to left ventricular hypertrophy and geometry: the Strong Heart Study. *J. Hypertens.* **28**, 384–388 (2010).
15. Chen, C.-H. et al. Different effects of foscipril and atenolol on wave reflections in hypertensive patients. *Hypertension* **25**, 1034–1041 (1995).
16. Pini, R. et al. Central but not brachial blood pressure predicts cardiovascular events in an unselected geriatric population: the ICARE Dicomano Study. *J. Am. Coll. Cardiol.* **51**, 2432–2439 (2008).
17. Langewouters, G., Settels, J., Roelandt, R. & Wesseling, K. Why use Finapres or Portapres rather than intraarterial or intermittent non-invasive techniques of blood pressure measurement? *J. Med. Eng. Technol.* **22**, 37–43 (1998).
18. Kim, J. et al. Battery-free, stretchable optoelectronic systems for wireless optical characterization of the skin. *Sci. Adv.* **2**, e1600418 (2016).
19. Schwartz, G. et al. Flexible polymer transistors with high pressure sensitivity for application in electronic skin and health monitoring. *Nat. Commun.* **4**, 1859–1870 (2013).
20. Sandberg, M., Zhang, Q., Styf, J., Gerdle, B. & Lindberg, L. G. Non-invasive monitoring of muscle blood perfusion by photoplethysmography: evaluation of a new application. *Acta Physiol.* **183**, 335–343 (2005).
21. Hertzman, A. B. The blood supply of various skin areas as estimated by the photoelectric plethysmograph. *Am. J. Physiol. Cell. Physiol.* **124**, 328–340 (1938).
22. Maeda, Y., Sekine, M. & Tamura, T. Relationship between measurement site and motion artifacts in wearable reflected photoplethysmography. *J. Med. Syst.* **35**, 969–976 (2011).
23. Xing, X. & Sun, M. Optical blood pressure estimation with photoplethysmography and FFT-based neural networks. *Biomed. Opt. Express* **7**, 3007–3020 (2016).
24. Drzewiecki, G. M., Melbin, J. & Noordergraaf, A. Arterial tonometry: review and analysis. *J. Biomech.* **16**, 141–152 (1983).
25. Howard, G. et al. Carotid artery intimal-medial thickness distribution in general populations as evaluated by B-mode ultrasound. *Stroke* **24**, 1297–1304 (1993).
26. Rotenberg, M. Y. & Tian, B. Bioelectronic devices: long-lived recordings. *Nat. Biomed. Eng.* **1**, 48–50 (2017).
27. Kim, D.-H. et al. Epidermal electronics. *Science* **333**, 838–843 (2011).
28. Yokota, T. et al. Ultraflexible, large-area, physiological temperature sensors for multipoint measurements. *Proc. Natl Acad. Sci. USA* **112**, 14533–14538 (2015).
29. Gao, W. et al. Fully integrated wearable sensor arrays for multiplexed in situ perspiration analysis. *Nature* **529**, 509–514 (2016).
30. Martín, A. et al. Epidermal microfluidic electrochemical detection system: enhanced sweat sampling and metabolite detection. *ACS Sens.* **2**, 1860–1868 (2017).
31. Huang, X. et al. Materials and designs for wireless epidermal sensors of hydration and strain. *Adv. Funct. Mater.* **24**, 3846–3854 (2014).
32. Arndt, J. O., Klauske, J. & Mersch, F. The diameter of the intact carotid artery in man and its change with pulse pressure. *Pflugers Arch.* **301**, 230–240 (1968).
33. Zhou, Q., Lam, K. H., Zheng, H., Qiu, W. & Shung, K. K. Piezoelectric single crystal ultrasonic transducers for biomedical applications. *Prog. Mater. Sci.* **66**, 87–111 (2014).
34. Sun, P. et al. High frequency PMN-PT 1–3 composite transducer for ultrasonic imaging application. *Ferroelectrics* **408**, 120–128 (2010).
35. Arumugam, V., Naresh, M. & Sanjeevi, R. Effect of strain rate on the fracture behaviour of skin. *J. Biosci.* **19**, 307–313 (1994).
36. Kitamura, K., Jorgensen, C. R., Gobel, F. L., Taylor, H. L. & Wang, Y. Hemodynamic correlates of myocardial oxygen consumption during upright exercise. *J. Appl. Physiol.* **32**, 516–522 (1972).
37. Ishibashi, Y., Duncker, D. J., Zhang, J. & Bache, R. J. ATP-sensitive K⁺ channels, adenosine, and nitric oxide-mediated mechanisms account for coronary vasodilation during exercise. *Circ. Res.* **82**, 346–359 (1998).
38. Wain, R. A. et al. Accuracy of duplex ultrasound in evaluating carotid artery anatomy before endarterectomy. *J. Vasc. Surg.* **27**, 235–244 (1998).
39. Donahue, S. P., Wood, J. P., Patel, B. M. & Quinn, J. V. Correlation of sonographic measurements of the internal jugular vein with central venous pressure. *Am. J. Emerg. Med.* **27**, 851–855 (2009).
40. Butman, S. M., Ewy, G. A., Standen, J. R., Kern, K. B. & Hahn, E. Bedside cardiovascular examination in patients with severe chronic heart failure: importance of rest or inducible jugular venous distension. *J. Am. Coll. Cardiol.* **22**, 968–974 (1993).
41. Mukkamala, R. & Xu, D. Continuous and less invasive central hemodynamic monitoring by blood pressure waveform analysis. *Am. J. Physiol. Heart Circ. Physiol.* **299**, 584–599 (2010).
42. Camacho, F., Avolio, A. & Lovell, N. Estimation of pressure pulse amplification between aorta and brachial artery using stepwise multiple regression models. *Physiol. Meas.* **25**, 879–889 (2004).
43. Williams, B. et al. Differential impact of blood pressure-lowering drugs on central aortic pressure and clinical outcomes: principal results of the Conduit Artery Function Evaluation (CAFE) study. *Circulation* **113**, 1213–1225 (2006).
44. Shirwany, N. A. & Zou, M.-h. Arterial stiffness: a brief review. *Acta Pharmacol. Sin.* **31**, 1267–1276 (2010).
45. DeLoach, S. S. & Townsend, R. R. Vascular stiffness: its measurement and significance for epidemiologic and outcome studies. *Clin. J. Am. Soc. Nephrol.* **3**, 184–192 (2008).
46. Mukkamala, R. et al. Toward ubiquitous blood pressure monitoring via pulse transit time: theory and practice. *IEEE Trans. Biomed. Eng.* **62**, 1879–1901 (2015).
47. Ren, K., Liu, Y., Geng, X., Hofmann, H. F. & Zhang, Q. M. Single crystal PMN-PT/epoxy 1–3 composite for energy-harvesting application. *IEEE Trans. Ultrason. Ferroelectr. Freq. Control* **53**, 631–638 (2006).
48. Hu, H. et al. Stretchable ultrasonic transducer arrays for three-dimensional imaging on complex surfaces. *Sci. Adv.* **4**, eaar3979 (2018).

Acknowledgements

The project was supported by the National Institutes of Health (NIH, grant R21EB025521) and the Center for Wearable Sensors at the University of California, San Diego. The content is solely the responsibility of the authors and does not necessarily represent the official views of the NIH. All bio-experiments were conducted in accordance with the ethical guidelines of the NIH and with the approval of the Institutional Review Board of the University of California, San Diego (IRB no. 170812). The authors thank K. Anagnostopoulos and H. Kim for discussions and advice regarding Picoscope DAQ, A. Kahn for discussions on PWV measurements, E. Topol, S. Steinhilbl and E. Muse for stimulating discussions on ambulatory BP measurement, Q. Yang and R. Lal for mechanical vibration characterization of the 1–3 composite material, and S. Xiang for constructive feedback on manuscript preparation.

Author contributions

Chonghe Wang and S.X. designed the research. Chonghe Wang, X.L., M.L., Z.Z. and H.H. performed the experiment. Chonghe Wang performed the simulation. Chonghe Wang, M.L., Z.Z. and X.L. analysed the data. Chonghe Wang, Z.Z. and S.X. wrote the paper. All authors provided active and valuable feedback on the manuscript.

Competing interests

The authors declare no competing interests.

Additional information

Supplementary information is available for this paper at <https://doi.org/10.1038/s41551-018-0287-x>.

Reprints and permissions information is available at www.nature.com/reprints.

Correspondence and requests for materials should be addressed to S.X.

Publisher's note: Springer Nature remains neutral with regard to jurisdictional claims in published maps and institutional affiliations.

Life Sciences Reporting Summary

Nature Research wishes to improve the reproducibility of the work that we publish. This form is intended for publication with all accepted life science papers and provides structure for consistency and transparency in reporting. Every life science submission will use this form; some list items might not apply to an individual manuscript, but all fields must be completed for clarity.

For further information on the points included in this form, see [Reporting Life Sciences Research](#). For further information on Nature Research policies, including our [data availability policy](#), see [Authors & Referees](#) and the [Editorial Policy Checklist](#).

Please do not complete any field with "not applicable" or n/a. Refer to the help text for what text to use if an item is not relevant to your study. [For final submission](#): please carefully check your responses for accuracy; you will not be able to make changes later.

▶ Experimental design

1. Sample size

Describe how sample size was determined.

The blood-pressure-waveform sampling was taken on the same subject at different body parts (three measurements for each). Owing to the high reproducibility of the measurements, the chosen sampling size was determined to be sufficient.

2. Data exclusions

Describe any data exclusions.

No data were excluded from the analyses.

3. Replication

Describe the measures taken to verify the reproducibility of the experimental findings.

The blood-pressure waveform was taken on the same subject (with stable physiological condition). All the sampling positions were measured in 4 discrete periods of time. All the measurement were taken within the same 2 weeks. The high similarity of the results showed good reproducibility of the blood-pressure-waveform acquisition. All attempts at replication were successful.

The ECG correlation was taken on the same subject (with stable physiological condition). Measurements were carried out in 3 discrete periods of time. All attempts at replication were successful.

4. Randomization

Describe how samples/organisms/participants were allocated into experimental groups.

The device type was tested in the same participant. Randomization was therefore not relevant to the study.

5. Blinding

Describe whether the investigators were blinded to group allocation during data collection and/or analysis.

Not relevant, because a blinding process wouldn't influence the sampling result.

Note: all in vivo studies must report how sample size was determined and whether blinding and randomization were used.

6. Statistical parameters

For all figures and tables that use statistical methods, confirm that the following items are present in relevant figure legends (or in the Methods section if additional space is needed).

n/a Confirmed

- The exact sample size (n) for each experimental group/condition, given as a discrete number and unit of measurement (animals, litters, cultures, etc.)
- A description of how samples were collected, noting whether measurements were taken from distinct samples or whether the same sample was measured repeatedly
- A statement indicating how many times each experiment was replicated
- The statistical test(s) used and whether they are one- or two-sided
Only common tests should be described solely by name; describe more complex techniques in the Methods section.
- A description of any assumptions or corrections, such as an adjustment for multiple comparisons
- Test values indicating whether an effect is present
Provide confidence intervals or give results of significance tests (e.g. P values) as exact values whenever appropriate and with effect sizes noted.
- A clear description of statistics including central tendency (e.g. median, mean) and variation (e.g. standard deviation, interquartile range)
- Clearly defined error bars in all relevant figure captions (with explicit mention of central tendency and variation)

See the web collection on [statistics for biologists](#) for further resources and guidance.

► Software

Policy information about [availability of computer code](#)

7. Software

Describe the software used to analyze the data in this study.

Origin 2018. Matlab 2016b.

For manuscripts utilizing custom algorithms or software that are central to the paper but not yet described in the published literature, software must be made available to editors and reviewers upon request. We strongly encourage code deposition in a community repository (e.g. GitHub). [Nature Methods guidance for providing algorithms and software for publication](#) provides further information on this topic.

► Materials and reagents

Policy information about [availability of materials](#)

8. Materials availability

Indicate whether there are restrictions on availability of unique materials or if these materials are only available for distribution by a third party.

No unique materials were used.

9. Antibodies

Describe the antibodies used and how they were validated for use in the system under study (i.e. assay and species).

No antibodies were used.

10. Eukaryotic cell lines

a. State the source of each eukaryotic cell line used.

The HFF-1 cell line was purchased from ATCC.

b. Describe the method of cell line authentication used.

The human skin fibroblast cells HFF-1 were first purchased from American Type Culture Collection (ATCC) (product number is ATCC SCRC-1041) and cultured in Dulbecco's Modified Eagle's Medium (DMEM, Gibco) supplemented with 10% fetal bovine serum (FBS, Gibco) and 1% penicillin/streptomycin (Gibco) under 37 °C within 5% CO₂.

c. Report whether the cell lines were tested for mycoplasma contamination.

The cell lines were not tested for mycoplasma contamination.

d. If any of the cell lines used are listed in the database of commonly misidentified cell lines maintained by [ICLAC](#), provide a scientific rationale for their use.

No commonly misidentified cell lines were used.

► Animals and human research participants

Policy information about [studies involving animals](#); when reporting animal research, follow the [ARRIVE guidelines](#)

11. Description of research animals

Provide all relevant details on animals and/or animal-derived materials used in the study.

No animals were used.

Policy information about [studies involving human research participants](#)

12. Description of human research participants

Describe the covariate-relevant population characteristics of the human research participants.

The human participant was a healthy male of age 22, with no cardiovascular abnormalities

In the format provided by the authors and unedited.

Monitoring of the central blood pressure waveform via a conformal ultrasonic device

Chonghe Wang^{1,10}, Xiaoshi Li^{2,10}, Hongjie Hu^{2,10}, Lin Zhang¹, Zhenlong Huang¹, MUYANG Lin^{1,3}, Zhuorui Zhang¹, Zhenan Yin⁴, Brady Huang⁵, Hua Gong¹, Shubha Bhaskaran⁴, Yue Gu², Mitsutoshi Makihata⁶, Yuxuan Guo¹, Yusheng Lei¹, Yimu Chen¹, Chunfeng Wang^{1,7}, Yang Li¹, Tianjiao Zhang¹, Zeyu Chen⁸, Albert P. Pisano⁶, Liangfang Zhang¹, Qifa Zhou⁸ and Sheng Xu^{1,2,4,9*}

¹Department of Nanoengineering, University of California San Diego, La Jolla, CA, USA. ²Materials Science and Engineering Program, University of California San Diego, La Jolla, CA, USA. ³School of Precision Instrument and Optoelectronic Engineering, Tianjin University, Tianjin, China. ⁴Department of Electrical and Computer Engineering, University of California San Diego, La Jolla, CA, USA. ⁵Department of Radiology, School of Medicine, University of California San Diego, La Jolla, CA, USA. ⁶Department of Mechanical and Aerospace Engineering, University of California San Diego, La Jolla, CA, USA. ⁷The Key Laboratory of Materials Processing and Mold of Ministry of Education, School of Materials Science and Engineering, School of Physics & Engineering, Zhengzhou University, Zhengzhou, Henan, China. ⁸Department of Ophthalmology and Biomedical Engineering, Viterbi School of Engineering, University of Southern California, Los Angeles, CA, USA. ⁹Department of Bioengineering, University of California San Diego, La Jolla, CA, USA. ¹⁰These authors contributed equally: Chonghe Wang, Xiaoshi Li, Hongjie Hu. *e-mail: shengxu@ucsd.edu

Table of Contents

Supplementary Notes	5
Supplementary note 1: Comparison to the catheter.	5
Supplementary note 2: Comparison to the commercial PPG.....	6
Supplementary note 3: Comparison to the commercial tonometer.	8
Supplementary note 4: Comparison to the ultrasound wall tracking.	10
Supplementary note 5: Device design strategy.	11
Supplementary note 6: Vessel position alignment and blood vessel mapping.	15
Supplementary note 7: VIA design and electrical connection.	16
Supplementary note 8: Measurement principle and resolution.	17
Supplementary note 9: BP waveform calibration and validation.	19
Supplementary note 10: Strain on the skin.....	22
Supplementary note 11: Measurement uncertainty, accuracy, and precision.	23
Supplementary note 12: Challenges of current approaches for BP waveform monitoring.	27
Supplementary note 13: Clinical significance of BP waveform.	29
Supplementary note 14: Simultaneous measurement of pulse pressure.	33
Supplementary note 15: Medical value to measure the progressive change of BP waveforms.	34
Supplementary note 16: Pulse arrival time, pulse transit time and pulse wave velocity.	35
Supplementary Figures	36
Supplementary Fig. 1. Comparison of BP measurement using different approaches in different situations.	36
Supplementary Fig. 2. The anatomic structure of BP waveform testing spots.	37
Supplementary Fig. 3. The effect of tiny operator movement on the image reconstruction quality using an ultrasound imaging probe	38
Supplementary Fig. 4. Vessel compression from holding the rigid ultrasound probe	39
Supplementary Fig. 5. Comparison of the probe structure between the rigid and conformal ultrasonic devices.	40
Supplementary Fig. 6. Device schematics and design layout.	41
Supplementary Fig. 7. Photographs of the uniaxial tensile test.	42
Supplementary Fig. 8. Photographs of the bi-axial tensile test.	43
Supplementary Fig. 9. Spatial pulse length of reflected signals.....	44

Supplementary Fig. 10. Axial resolution characterization of the stretchable ultrasonic device.	45
Supplementary Fig. 11. Transducer array and vessel line mapping.	46
Supplementary Fig. 12. Double-layered electrode with a vertical interconnect access (VIA) under tensile strain.....	46
Supplementary Fig. 13. Photographs of the process of using the conformal device.	47
Supplementary Fig. 14. Diameter measurement validation using the commercial ultrasonographic probe.	49
Supplementary Fig. 15. The damping effect of the Ecoflex.	50
Supplementary Fig. 16. Acoustic field simulation for 1-3 piezoelectric composites with different sizes.....	51
Supplementary Fig. 17. Acoustic emission performance comparison of devices with different diameters of the circular bottom electrode.....	52
Supplementary Fig. 18. Photographs of the device integrated on the skin, demonstrating its outstanding mechanical compliance.	53
Supplementary Fig. 19. Electrical performance of the device under various levels of tensile strain and moisture conditions at room temperature.	54
Supplementary Fig. 20. Cell viability assay.	55
Supplementary Fig. 21. Comparison of measurement uncertainty between the commercial tonometer (SphygmoCor EM3 [®]) and our ultrasonic device.....	56
Supplementary Fig. 22. The measured BP waveform using our device and its uncertainty range.	57
Supplementary Fig. 23. Operator dependency of the commercial applanation tonometry system (SphygmoCor EM3 [®]) measuring the radial artery (peripheral).....	58
Supplementary Fig. 24. Operator dependency of the gold standard applanation tonometry system (SphygmoCor EM3 [®]) measuring the carotid artery (central).	59
Supplementary Fig. 25. Comparison of the device acoustic emission performance with and without ultrasonic gel.....	60
Supplementary Fig. 26. Signal qualities of the conformal ultrasound device with different coupling agents.....	61
Supplementary Fig. 27. Reusability test of the device	62
Supplementary Fig. 28. Conformability and self-adhesion of the device on the neck under different postures	63
Supplementary Fig. 29. CBP measurement results and their validation.	64

Supplementary Fig. 30. The anatomical structure of the human heart and associated blood flow sequence.	65
Supplementary Fig. 31. BP waveform illustration.	66
Supplementary Fig. 32. A Doppler ultrasound image of an internal jugular vein and its associated Doppler waveform.	67
Supplementary Fig. 33. JVD monitoring by the conformal ultrasound device.	68
Supplementary Fig. 34. Grayscale images of blood vessels from central to peripheral measured by Doppler ultrasound.	69
Supplementary Fig. 35. Measurement validation using a commercial equipment of pulse pressure amplification from the central artery (CA) to the peripheral arteries (BA, RA, and PA).....	70
Supplementary Fig. 36. Comparison of the upstroke gradient from the central to peripheral arteries.	71
Supplementary Fig. 37. Testing conditions for ECG correlation.	72
Supplementary Fig. 38. Testing robustness of the ECG correlation.	73
Supplementary Fig. 39. The commercial CBP monitoring tonometer: SphygmoCor EM3 [®] (AtCor Medical, Sydney, Australia) with ECG patches for PWV measurements.....	74
Supplementary Fig. 40. Stretchable ultrasound device fabrication flow chart.	75
Supplementary Fig. 41. Photographs of Cu patterns processed under different levels of laser power.	76
Supplementary Fig. 42. Photographs of the Cu serpentine patterns with different widths.	77
Supplementary Fig. 43. Relationship between Ecoflex thickness and spin speed on a glass slide.	78
Supplementary Fig. 44. Photographs of the Cu pattern (a) before and (b) after surface oxide removal using flux.....	79
Supplementary Fig. 45. The polarization hysteresis loop, illustrating the switchable dipole alignment of the piezoelectric materials under an electrical field.	80
Supplementary Fig. 46. Acoustic emission performance comparison between normal polarization and breakdown.	81
Supplementary Fig. 47. The experimental setup for BP measurement.....	82
Supplementary Fig. 48. Schematic illustration of the activating and the receiving signals during the wall-tracking process.....	83
Supplementary Fig. 49. Schematic illustration of the vessel wall-tracking system designed in this work.	84

Supplementary Fig. 50. Influence of the PRF on BP waveform morphology.....	85
Supplementary Fig. 51. The circuit diagram for multi-channel sensing.....	86
Supplementary Fig. 52. Illustration of the PAT and PTT calculated from ECG and BP waveforms.	87
Supplementary Fig. 53. Schematic illustration of piezoelectric ultrasound transducers (PUTs) and micromachined ultrasound transducers (MUTs).....	88

Supplementary Notes

Supplementary note 1: Comparison to the catheter.

The arterial catheter, as known as cannulation, is the most accurate method for measuring CBP, which is needed for all-cause cardiovascular mortality prediction. This method requires the injection of the pressure sensor into the arterial line and directly record the intravascular pressure. However, this technique is too invasive, and patients may easily get infections during and after testing. Therefore, arterial catheterization is not suitable for frequent and routine CBP measurements.

The conformal ultrasound device in this work can provide a penetration depth of 4 cm, which is sufficient for CBP monitoring continuously and non-invasively.

Supplementary note 2: Comparison to the commercial PPG.

PPG is an optically obtained plethysmography method to measure the volume changing of an organ (e.g., the artery or vein). The change in volume caused by the pressure pulse is detected by illuminating the skin through LED light and then measuring the light either transmitted or reflected to a photodiode. However, there are four significant disadvantages of the PPG, which are summarized as follows.

First, the most significant challenge is that the LED has relatively limited light penetration depth (~8 mm). Thus, PPG is only useful for superficial arteries, e.g., radial arteries (even with challenges) and peripheral arterioles in fingers and ear lobes¹. However, pulsation from brachial and carotid arteries cannot be obtained by PPG. What's more, for obese subjects, the fat layer in their tissue will be much thicker than normal people, and their arteries may be embedded very deep. As illustrated in Supplementary Fig. 1, the light cannot reach the target artery due to the absorption by the fat layer above. The same circumstance occurs when we measure the central arteries. For example, the carotid artery is embedded in a depth of around 3 cm, which is beyond the penetration depth of PPG. Therefore, this device is only suitable for limited measuring spots.

The conformal ultrasound device in this work can provide a penetration depth of 4 cm. This penetration capability is sufficient for any of the aforementioned blood vessels such as radial, brachial, and carotid arteries, and the jugular vein since all those vessels locate in depth within 3 cm. The penetration property of our device is comparable to the existing clinical equipment. As Supplementary Fig. 1 illustrates, the ultrasound beam can reach and realize the wall-tracking function even with thick tissue on top of the vessel. Also, our device is not confined to measure specific peripheral arteries. Instead, all major arteries, as long as they are not surrounded by a substantial bony structure such as the central cerebral artery surround by the skull and the central aorta enclosed by the sternum, can all be monitored by our conformal device.

Second, PPG can't extract accurate BP waveforms from arteries adjacent to veins. Because when the measurement is implemented in those arteries, the volumetric circulatory change in the artery will easily interfere with that in the vein². The PPG will sense both the arterial and venous pulses at the same time due to the non-directional characteristics of the light. Human anatomical structures around the testing spot of radial (Supplementary Fig. 2a), brachial (Supplementary Fig. 2b), and carotid (Supplementary Fig. 2c) show veins are incredibly close to the target arteries. For example, Supplementary Fig. 2a shows the radial testing spot, where the radial artery and radial vein are very close to each other. The brachial artery testing spot, as illustrated in Supplementary Fig. 2b, are overlapping with the brachial vein. This trend is the same when performing the test on the carotid artery. In which, the internal jugular vein overlays on the carotid artery (Supplementary Fig. 2c). Those anatomic configurations will significantly limit the application of PPG. Therefore, PPG has to work based on a weak assumption that the pulsatile component in the signals reflects solely the arterial blood volume changes². As a result, PPG can only perform rough measurements when the surrounding vasculature and anatomy are complicated.

Ultrasound is well-known for its high beam directivity. Our device can generate a highly directional ultrasound beam, with a thin beam width of 1 mm, which is smaller than the size of those aforementioned arteries/veins. Therefore, our device can selectively penetrate the target vessel without interfering with the adjacent ones. In the scenario when artery and vein are overlapping with each other at a certain point (e.g., Supplementary Fig. 2b at the brachial measurement site), the ultrasound beam will penetrate the artery and vein

simultaneously. The device can differentiate the arterial and the venous signals. Each transducer in the densely distributed stretchable array can be individually addressed. The most suitable measuring point can be located by actuating the transducer one by one and calculate the vessel distension quantity. This mapping function will guarantee only the target vessel is exposed to the ultrasound beam and avoid measuring any spots where the target vessels overlap together. The demonstration of blood vessel differentiation is illustrated in Supplementary Fig. 11. The element with optimal position will have the largest vessel distension quantity. The deep-tissue penetration capability of the ultrasound enables our device to locate and track vessels buried underneath the skin with a depth up to 4 cm.

Third, PPG has been reported of practical disadvantages that measurement should be conducted in an environment with constant ambient temperature and humidity³ since PPG is sensitive to heat and moisture⁴. Unfortunately, human epidermis on the finger is ever-changing brought by thermoregulation⁵ and sweat⁶. Those two factors will both contribute to the complexity of the measurement, especially when the subjects have some diseases. For instance, Primary Raynaud's Phenomenon will lead to a substantial seasonal thermal difference on the skin⁷. A heart attack will cause the patient to sweat severely⁸, thus bringing artifacts and incorrect results.

In our case, none of those factors will introduce any influence to the performance of conformal ultrasound devices. To be more specific, our conformal ultrasound probe is not susceptible to skin hydration because the material for electronic encapsulation, Silicone, is hydrophobic. All piezoelectric elements are protected in a moisture-free environment. Interestingly, a moderate quantity of water/sweat outside the epidermis will improve the acoustic coupling by eliminating the small air bubbles at the device/skin interface. The measurement result using conformal ultrasound device under skin moisture is shown in Supplementary Fig. 26. With comparable SNR to the acoustic coupling condition provided by the ultrasound gel, our method can do the measurement with the moisture. Additionally, our device will not be influenced by human skin temperature either. As long as the temperature is below 80 degrees Celsius, the 1-3 composite material will maintain its stable sensitivity even during long-term high-temperature (<80 degrees Celsius) exposure.

Finally, PPG is based on the weak assumption that the blood has a constant light absorptivity, which highly relies on the blood composition⁹, especially the substances (e.g., the hemoglobin) having high absorptivity at near infrared¹⁰. Otherwise, the volume flow rate measured by the plethysmographic method is not reliable. Counterexamples include after an IV injection and undergoing a large hemodynamic fluctuation such as severe edema and blood clot¹¹. Those conditions will significantly reduce the ratio of the hemoglobin in the blood, and cause incorrect measurements.

In our cases, accurate wall-tracking does not depend on the blood composition or the hemoglobin concentration. Therefore, our device is not susceptible to those uncontrollable conditions.

Supplementary note 3: Comparison to the commercial tonometer.

The tonometry obtains the BP waveform using a pressure sensor that senses the arterial pulse, i.e., the mechanical vibration propagated from the vessel to the epidermis. The pulsating behavior of the blood vessel can be recorded and translated to BP waveforms. This technique is highly operator-dependent, creating significant challenges for a normal individual to use. Two aspects are discussed here to reflect the operator-dependency:

First, tiny offset from the central arterial axis will introduce significant distortion to the waveform acquisition. The standard and correct measurements are performed in Supplementary Fig. 24a. The distorted measurement results using the tonometer with a tiny offset from the carotid are shown in Supplementary Fig. 24b.

Our ultrasound device design is based on an array of transducers, which possesses the capability to locate the best spot for BP waveform recording. Each transducer is addressed individually first to record the signal for post-processing and analysis. After comparing the 20 translated waveforms obtained, the correct waveform can be defined as the one best related to the waveform obtained by the commercial gold standard, indicating the appropriate measurement spot. In this way, we can acquire the BP waveform using that particular transducer to ensure there is no offset from the sensor to the target artery. This process can eliminate the requirement of finding the correct position by the operator. The blood vessel positioning data is demonstrated in Supplementary Fig. 11.

Second, excess holding forces on the tonometer probe will introduce tremendous recording error of the BP waveform due to the closure of the artery, as shown in Supplementary Fig. 24c. Also, due to the large holding pressure of the probe to the skin, long-term recording by the tonometer will cause skin irritation to the subject. After conducting standard measurement by the tonometer for 10 minutes, severe indentation is observed at the skin surface as shown in Fig. 3b.

With only 150 mg in weight, 240 μm in thickness, and similar elastic modulus to the skin, the conformal device is mechanically invisible to the testing subject. It will induce negligible pressure (3.68 Pa) to the skin surface. Comparing to the tonometer, by which the operator usually exerts $9 \times 10^4 \sim 1.1 \times 10^5$ Pa to the human skin, this method leads to four orders of magnitude lower in mechanical loading. It can therefore perform reliable measurements for long term without any skin irritation.

Third, accurate BP measurement using tonometer requires tests conducted at spots close to a supporting bony structure. At these spots, tonometer can sense the pulsating signal by efficiently flattening the artery¹². The requirement is easily met when conducting BP measurement at peripheral arteries. For example, the radial artery is supported by the radius. The brachial artery is supported by the humerus. However, when one moves from the peripheral sites to the central artery sites, collecting accurate and reliable BP waveforms is challenging since there is no proximal bony structure as shown in Supplementary Fig. 1. Also, as shown by the anatomical structure in Supplementary Fig. 2, arteries are usually close to the veins at all measurement spots. Therefore, the mixed pulsation of arteries and veins will distort the captured waveform even though the venous pulsation is much weaker than the arterial pulse. The mixture of the arterial and venous pulses will cause distortions in the waveform recording¹³.

The ultrasonic device does not need any supporting structure to pick up the vessel pulsation, by actively sending and receiving acoustic waves that allow capturing the dynamic diameter change of the vessels.

Finally, BP measurements by the tonometer are accurate only under the circumstances with stable contact between the probe and the skin of the subject. In standard measurements, this requirement can be easily met. However, if the subject undergoes a tremble or a posture change, the recording will be interrupted due to the poor skin contact.

The unique advantage brought by the stretchable device is that its similar mechanical properties to the human skin can ensure conformal and stable contact to the skin, by van der Waals forces alone. This feature can significantly minimize the clinician dependency. Even during slight motion, our device can stay on the skin with intimate interfacial contact and thus can reduce the motion artifacts. We measured the same site under wrist movement by our conformal device and the commercial tonometer. The testing subject underwent an intentional tremble and changed the wrist angle from 0° to 15° and 30°. Continuous measurement results and the associated correlation curve show our device could maintain relatively more stable measurements.

Supplementary note 4: Comparison to the ultrasound wall tracking.

The ultrasound wall tracking requires using ultrasound B mode scanning to locate and track the blood vessel pulsatile behavior during cardiac cycles, in which, blood vessel diameter waveforms will be recorded and translated to BP waveforms using the translational algorithm as detailed in the Supplementary note 8. However, the wall-tracking method using conventional ultrasound probes has several drawbacks.

First, the image quality is easily degraded due to the poor contact between the skin and the rigid and bulky ultrasound probe. Conventional ultrasound probes for B mode imaging are usually thicker than 10 cm. To conduct accurate measurements, the clinician should hold the probe stably and guarantee a good contact between the probe and skin. Thus, this method is highly operator dependent and very sensitive to non-standard operations. For example, as illustrated in Supplementary Fig. 3, the reconstructed image will be significantly blurred by tiny motions from the operator. The top picture shows a standard image scanning. The bottom picture is acquired with tiny movements of the operator. This blurry image will introduce inaccuracy in the computerized wall-tracking algorithm.

With conformal contact with the human skin, our device can self-adhere to the skin and do the measurement without any manual holding. Therefore, no shaking, vibration or other motion artifacts will be introduced by the operator.

Secondly, although the operator has a standardized operation during measurement. There is still high chance for the vessel to be compressed slightly, as illustrated in Supplementary Fig. 4. It is challenging for the clinician to hold the probe steady with moderate force. As a consequence, compressive interruption to the vessel is inevitable. If this happens, the pulsatile behavior and local hemodynamics will be changed, introducing erroneous recording.

With only 150 mg in weight, our device has only 3.68 Pa pressure to the skin. This level of stress is comparable to that a piece of printing paper exerted to the table, which is nearly mechanically invisible to human tissue. With this unique strength, our device can perform accurate and reliable measurement without changing the natural behavior of the blood vessel distension.

Through this device design, it is possible to achieve ultrasonography for imaging and BP measurements and with reduced operator-dependency. One potential technical problem is to incorporate transducers with an ultra-small footprint and a high resonance frequency. Imaging ultrasonography typically requires a resonant frequency of 15 MHz or higher, resulting in much smaller footprint and pitch of the transducer. And, to avoid side lobes, the transmitting apertures and pitches need to be decreased to near half of the wavelength. Integrating these small transducers into stretchable devices by the "island-bridge" layout requires advanced microfabrication techniques, which will be systematically studied in our future work.

Supplementary note 5: Device design strategy.

5.1 Choice of the transducer.

The piezoelectric ultrasound transducers (PUTs) is adopted in this work as the basic functional unit. All of the components in PUTs are illustrated in Supplementary Fig. 53. The PUTs can generate ultrasound waves by extensional vibrations of the piezoelectric material. The frequency of the transducer is decided by the thickness of the piezoelectric material. Thinner material gives higher frequency. The performance, e.g., transmission, sensitivity, and bandwidth, can be tuned by the matching and backing layers¹⁴. The acoustic impedance can be tuned by different types of piezoelectric materials¹⁴. However, PUTs has significant challenges for high-frequency transducer array applications. To be more specific, high frequency phased array imaging (over 50 MHz) requires ultrathin piezoelectric layer (below 20 μm). Additionally, the pitch of the transducer must be smaller than 0.6λ , requiring the footprint to be below 18 μm ¹⁵. Both the thickness and the footprint are challenging for PUTs fabrication¹⁵. Take the matching layer for example. In high-frequency applications, the corresponding matching layer below $\frac{1}{4} \lambda$ in thickness becomes too thin to be practically handled using existing dicing and cabling technologies¹⁶.

The micromachined ultrasound transducers (MUTs) has special and unique strengths to solve the challenges for the high frequency phased array system¹⁷⁻¹⁹. The MUTs are investigated for miniaturized transducers that can overcome the frequency-thickness dependency by designing its structural layout. The MUTs can be designed for different frequencies and performances by controlling its element width and layer structure²⁰. Specifically, with proper selection of the radius of the diaphragm with tailored effective mechanical stiffness, its bandwidth, sensitivity, and acoustic impedance can be tuned¹⁶. This leads to better design flexibility regardless of any thickness restrictions of the piezoelectric layer. Various types of fabrication methods have been reported to achieve this small footprint (10~750 μm), which can be suitable for the frequency range of 1~100 MHz²¹.

The micromachined ultrasound transducers (MUTs) family includes piezoelectric micromachined ultrasound transducers (pMUTs) and capacitive micromachined ultrasound transducers (cMUTs). Both of those two MUTs are based on flexural deflection but on different working principle. A cMUT element is, in essence, a miniaturized capacitor that consists of a thin metalized suspended membrane, e.g., silicon nitride (Si_3N_4), over a cavity with a rigid metalized substrate, e.g., silicon (Si), as shown in Supplementary Fig. 53b. When a voltage is applied between the two electrodes, the membrane will be deflected. This deflection results from the attraction toward the substrate by the electrostatic forces. The mechanical restoring force by the stiffness of the membrane resists the attraction²². Consequently, ultrasound can be generated from the oscillations of the membrane with an AC voltage input. It is reported that cMUTs have been demonstrated to produce high bandwidths (up to 175%) and electromechanical coupling coefficients (~ 0.85) and output acoustic pressure exceeding conventional transducers^{16,17,19}. However, in practice, this high performance can only be achieved when a large bias near the so-called collapse voltage is applied, which increases the risk of failure of the device. This disadvantage can, to some extent, limit performance in biomedical applications. Although new driving methods have been demonstrated, the problem still remains²³.

The pMUTs consist of an ultrathin PZT layer for piezo-actuation, employing the piezoelectric effect to drive the membranes in flexure. They consist of multilayered membranes and one layer of which is an active piezoelectric film. When excited electrically, the piezoelectric layer strains and generates the necessary deflection of the composite membrane. Unlike the

cMUTs, pMUTs do not require a large voltage bias and have fewer geometric and design constraints, facilitating integration with low voltage electronics¹⁵. Furthermore, pMUTs also offer several other advantages over cMUTs. Those advantages can be traced to their higher capacitance and lower electrical impedance. These increase the transducer sensitivity by decreasing the effects of parasitic capacitance while enabling the use of low voltage electronics²⁴.

Although MUTs family offers many unique advantages, e.g., the tunability of many characteristics and miniaturization for high-frequency applications. The disadvantages can be summarized as the requirement of complex design and fabrication process, the manufacturing of high-performance piezoelectric thin films (usually within several μm) for high frequency, and the lack of efficient modeling tools for accurate prediction of the target performances^{23,24}. Additionally, complicated microfabrication steps and equipment are needed to achieve high-performance MUTs¹⁶. The ultrasound performance can be influenced by many factors such as the shape, dimensions, boundary conditions, intrinsic stress, and mechanical stiffness of working element layers on the wafer²⁵.

Considering the ultrasound wall-tracking application of this work, we only need transducer frequency range between 5~10 MHz. This frequency range does not require an ultrathin thickness of the piezoelectric material. Moreover, the arrays do not need ultrafine footprint and pitch because no phased array is needed for this task. Therefore, we decide to fabricate PUTs as the functioning unit, without complex etching, sputter, or photolithography. The dicing used in this study is simpler, more economical, and without involving chemical pollution.

There are a few studies that demonstrate flexible ultrasound transducer arrays based on cMUTs or pMUTs²⁶⁻³¹. However, they have several problems, which greatly limit their applications as discussed below.

Technically, to acquire reliable physiological signal measurement on the highly curvilinear, time-dynamic, and non-developable skin surfaces, stretchability is required to allow seamless integration at the device/skin interface³². Specifically, the device should possess 30% stretchability and similar modulus to the skin⁵⁸. However, the existing devices based on pMUTs or cMUTs are only flexible but not stretchable^{27,30,33,34}. Although various techniques have been provided to fabricate those transducer arrays to solve this problem, the bio-integrated measurements have rarely been reported. The root cause of this problem is two-fold. Firstly, most of the existing devices have poor interconnect design in the transducer array, which significantly deteriorates the mechanical property²⁷. The device has a high risk of rupture during mechanical deformation³⁰. Secondly, the poor encapsulation design makes the device relatively rigid²⁷. Polyimide and PDMS are often adopted as the substrate in those devices, which have not only limited stretchability but also larger modulus than the human skin that can't guarantee conformal contact during the measurement³². The weak contact at the device/skin interface will introduce significant noise due to the inevitable air gaps. Lots of ultrasound gel that can quickly dry out would be needed during the measurement, thus limiting their wearability.

In this work, we used the island-bridge strategy to transform the conventional ultrasound probe into this stretchable, ultrathin, and conformal format. The "island-bridge" structure helps the device to achieve not only flexible but also stretchable configurations (Supplementary Figs. 7 and 8). The soft device can adhere intimately and seamlessly to the human skin with high curvatures (Supplementary Fig. 18), which is impossible for other types of ultrasound devices, including cMUT and pMUT transducer arrays. Also, the number,

size, thickness, and pitch of the elements can be adjusted according to the different requirements and applications without complex design and fabrication as in the case of cMUT or pMUT. The island pitch and element footprint design in our case are fully optimized for vessel localization, which is demonstrated as Supplementary Fig. 11. This function is unique in the sense that it allows clinician-independent measurements. Additionally, we use Eco-flex as the encapsulating material whose modulus is similar to human skin and possesses excellent stretchability. Also, Silbione substrate is coated at the bottom of the device to remove the influence of the air gaps thoroughly, allowing gel-free measurements (Supplementary Fig. 26).

In all, based on the properties above and comparison with the prior arts, our device is among the best prototypes of soft ultrasonic probes demonstrated. Those excellent properties can open up a variety of wearable biomedical applications.

5.2 Structure design of device: performance.

To characterize the performance of a transducer for diagnosis use, two parameters are usually critical: spatial pulse length (SPL) and sensitivity. As Supplementary Fig. 26 illustrated, our device usually can achieve an SNR over 15 dB. So the sensitivity is adequate. The relation between SPL and device structure design is discussed as follows.

The backing layer can be used to damp out the ringing effect by absorbing part of the energy from the vibration of the back surface to improve the performance of a piezoelectric transducer. To be more specific, this component can give smaller SPL thus achieving better resolution⁴. Therefore, the backing layer is critical in imaging applications. However, in our case, we do not track the vessel by ultrasonography. Instead, we track the movement of the vessel using amplitude mode signal by addressing a single transducer element that directly overlies on the artery. The tracking strategy and algorithm are discussed in details in Supplementary note 8. Via this strategy, we can achieve the wall-tracking with a spatial resolution of 0.77 μm and a temporal resolution of 500 μs during vessel pulsation. Moreover, it is worth noting both 0.77 μm and 500 μs resolution is for movement tracking functionality. To guarantee the accurate calibration process as mentioned in Supplementary note 9, the absolute diameter measurement should be accurate as well.

Therefore, we perform a validation between our device and the commercial ultrasonography by measuring the systolic diameter on the same subject and at the same position. The amplitude mode signal from measuring the systolic diameter of brachial artery appears in Supplementary Fig. 14a. We can measure the diameter of the artery by extracting the time of flight between the highest point of the echo peaks from the anterior and posterior walls (after filtration). The measurement result we achieve is 3.23 mm. And the measurement result of commercial ultrasonography indicates the diameter is 3.24 mm, as shown in Supplementary Fig. 14b. We can realize a 99.7% correlation between those two methods, as shown by the inset in Supplementary Fig. 14b. Therefore, our approach doesn't rely on the narrow spatial pulse length because it is not required to perform ultrasound imaging.

However, if the backing layer is needed to achieve efficient suppressing of long spatial pulse length, the thickness of the backing layer is often over 7 ~ 8 times thicker than the piezoelectric transducer³⁵. In our case, it will significantly increase the thickness of our device (reach 2 mm) and largely compromise the device conformability. This trend can be explained by the theory of material mechanics. The flexural rigidity is proportional to the third power of the material thickness. And, it has been demonstrated that when the device thickness is over 1.5 mm, it will be no longer conformal to the human skin^{32,36}. After

balancing the performance and wearability, in this study, we chose to design the device in an ultrathin format by removing the bulky backing layer. Future integration with the backing layer can be readily achievable when there is a strong need.

5.3 Structure design of device: durability.

For the durability of our device, the most critical aspect relies on the encapsulation. Thicker substrate gives higher device resilience. To be more specific, the thin bottom silicone layer serves as the protection of the functioning unit, i.e., the piezoelectric 1-3 composite. The hydrophobic and insulative nature of this silicone material can guarantee excellent piezoelectricity and performance of the transducer. Otherwise, the piezoelectric material would degrade when exposed to moisture/water. Electrical leakage would happen when the substrate is damaged thus limiting its performance. Meanwhile, if the substrate is too thick, the ultrasound will be significantly dampened because of the strong damping/attenuation effect of the silicone, as demonstrated in Supplementary Fig. 15. However, too thin substrate will compromise the robustness of the device. The trade-off is 15 μm thick, which can guarantee both ultrasound energy transmission and mechanical property. Our device can reach ~4 cm penetration, which is suitable for central vascular detection, as demonstrated in Figure 3 (carotid artery and jugular vein are embedded 3 cm under the skin). Also, our device can withstand 60% of strain in x-direction (Figure 2, and Supplementary Figs 7 and 8), and long-term monitoring with high reproducibility (Supplementary Fig. 27). Due to the lightweight and compliance characteristics brought by the soft electronic encapsulation, our device owns the unique advantage in resilience over traditional ultrasound probes. The conventional ultrasound probes are easy to crack if mishandled, which leads to short service cycle and high cost to repair. Our device is highly elastic and resilient, which is robust even under accidental mechanical crushing. Moreover, our conformal probe could be disposable since the conformal probe is assembled using the low-cost materials.

Supplementary note 6: Vessel position alignment and blood vessel mapping.

The alignment of the vessel can be done by the following procedures: Firstly, we activate and receive every transducer individually, 20 in total, and then collect the echo signals. After that, comparison is made to check the correspondence of peak positions with accurate measurement on the same artery region. The transducers on the arterial line with the best position will give the waveform with the best quality. We can justify the waveform quality by comparing the obtained waveform with the best waveform from the subject (which has been validated by commercial tonometer), also known as the similarity between the obtained waveform and accurate waveform. In this way, we can find the transducer that is in the optimized location (Supplementary Fig. 11). Therefore, later we can conduct reliable vessel diameter measurement using the particular transducer with the best pinpointing position.

Supplementary note 7: VIA design and electrical connection.

To optimize the circuitry design and minimize the electrical bonding difficulties, a vertical interconnect access (VIA) structure is designed (Fig. 1a) to route the bottom common ground to a unified region for ACF cable bonding. With this VIA, the ground line can be incorporated into the plane of the top electrode. The VIA is made of silver epoxy. This structure can guarantee the device has good connectivity and stretchability.

Supplementary note 8: Measurement principle and resolution.

The process of capturing excellent BP waveform relies on the temporal and spatial resolutions. The definition and our technical parameters adopted in this work are discussed as follows.

For temporal resolution, we perform the ultrasound wall-tracking by launching ultrasound waves in a high pulse repetitive frequency (PRF), which determines the temporal resolution. In each pulse cycle, the transducer is activated by a high-frequency alternating current (7.5 MHz in this study) to generate the ultrasound waves. PRF determines how many pulse cycles there are in one second. For example, when the PRF is 2000 Hz, the transducer can launch 2000 ultrasound pulses penetrating into the tissue within one second (Supplementary Fig. 48a).

After the ultrasound waves encounter various biological interfaces (e.g., the blood vessel/lumen interface), some parts will be reflected, other parts will transmit through the interfaces. The ratio between the reflection and transmission depends on the acoustic impedance difference between the two layers of tissues at the interface. The reflections can be detected by the same transducer. Given the acoustic velocity in the tissue, the echo signal (i.e., time of flight) contains information about the locations of the biological interfaces.

With a PRF of 2000 Hz, we can receive 2000 signals containing the displacement information of the tissue interfaces in one second (Supplementary Fig. 48b). Given high spatial resolution to distinguish the tiny arterial wall movement, we can acquire around 2000 sampling points in one waveform (assuming the cardiac cycle is close to 1 second). In this process, several typical signals appear in Supplementary Fig. 48c. We can clearly trace the movement of the peaks in the signal. In practical measurements, 2000 data points are sufficient to acquire a detailed BP waveform. In reality, 1000 Hz PRF (1 ms temporal resolution) has been shown to record the waveforms with high resolution³⁷⁻³⁹. In our experiment, 2000 Hz PRF (0.5 ms temporal resolution) is sufficient to realize the wall-tracking functionality, as seen from the waveform in Supplementary Fig. 50.

To further verify the sufficiency of the 2000 Hz PRF, we measured the BP waveform with different PRF from 10 Hz to 5000 Hz (Supplementary Fig. 50a). When the PRF is too low, e.g., 10 Hz and 20 Hz, the waveform will be rugged and miss some detailed morphologies, e.g., the systolic peak and dicrotic notch. As the PRF goes higher, more detailed and smoother waveform will be acquired. When the PRF is higher than 100 Hz, the waveform captures almost every detail.

Supplementary Fig. 50b shows the Pearson correlation coefficient between the signal with 5000 Hz PRF and signals with other PRF values. When the PRF is larger than 100 Hz, the Pearson correlation coefficient is very close to 1 (>0.9999) which means the similarity of two signals is more than 99.99%, and this number also meet the requirement of uncertainty. Thus, when the PRF is larger than 100 Hz, the waveform derived remains almost the same shape. Therefore, the 2000 Hz PRF used in this work is sufficient to capture the detailed morphologies of the waveform.

The spatial pulse length (SPL) characterization in Supplementary Fig. 10 is the standard parameter to reveal how close the adjacent interfaces can be differentiated. The transducer in this study has an SPL of around 400 μm , which is sufficient to distinguish the anterior and posterior walls of the blood vessels typically used in BP measurements. However, SPL

cannot represent the real spatial resolution of a wall-tracking functionality. The spatial resolution in our case is described in details as follows.

The point we selected to represent the position of the arterial wall is the peak of the echo signals, as shown in Supplementary Fig. 49a and 49b. Then we used the peak-tracing method to record the infinitesimal wall movement. As long as the movement of this discrete point can be recognized, the record is effective. The sampling rate pertains to how close the oscilloscope in the experiment can differentiate two points in the temporal space. The tracing of vessel walls relies on the differentiation of two adjacent discrete data points. A higher sampling rate leads to a smaller distance that can be differentiated, resulting in higher spatial resolution.

The sampling rate we adopted in the experiment is 2 GHz, so the sampling period is 0.5 ns. By timing the ultrasound speed 1540 m/s in the tissue, the effective resolution to trace the wall position is 0.77 μm . In other words, we can recognize 2 discrete points at a displacement of 0.77 μm (Supplementary Fig. 49c). This is sufficient for dividing the distension waveform in one cycle into at least 300 divisions for movement recognition. The sampling of the blood vessel diameter waveform is illustrated in Supplementary Fig. 49d-f. The vertical grids in Supplementary Fig. 49e represent the spatial resolution. Each grid has a scale of 0.77 μm . The distension under the heart pulsation can reach to around 10%~15% of the vessel diameter. Taking the smallest artery measured in our experiment, radial artery with a diameter of 3 mm, for example, the diameter distension can reach around 300 ~ 450 μm . Therefore, we can sample 388~584 different points/grids during one cardiac cycle. The horizontal grids represent the temporal resolution, with each grid representing 500 μs . Thus, we can get 2000 data points in one second.

In all, spatial resolution is determined by the sampling capability of the oscilloscope (2 GHz) used in the study. The temporal resolution is determined by the PRF (2000 Hz) used in the transmitting circuit. These two parameters selected in our experiments are both sufficient to capture the interesting details of the BP waveforms.

Supplementary note 9: BP waveform calibration and validation.

9.1 Calibration of the arterial BP

The arterial BP waveform $p(t)$ appears as follows:

$$p(t) = p_d \cdot e^{\alpha \left(\frac{A(t)}{A_d} - 1 \right)} \quad (1)$$

where p_d is diastolic pressure, A_d is the diastolic arterial cross-section and α is the rigidity coefficient. Assuming that artery is rotationally symmetrical, $A(t)$ can be calculated as:

$$A(t) = \frac{\pi d^2(t)}{4} \quad (2)$$

where $d(t)$ is the diameter waveform of the target artery.

We assume the human blood vessel is elastic with negligible viscoelasticity. In other words, the pressure-diameter curve has a moderate hysteresis, below 0.2%⁴⁰. This assumption is suitable for subjects with normal local vascular conditions or with slight local atherosclerosis. In this situation, the diameter of vessel won't lag behind the pressure waveforms⁴¹. And the equation (1) can be used to reconstruct the accurate BP waveforms from the vessel diameter waveforms. The largest hysteresis caused by vessel atherosclerosis is within 5.2%⁴².

α can be calculated by equation:

$$\alpha = \frac{A_d \ln(p_s/p_d)}{A_s - A_d} \quad (3)$$

wherein A_s is the systolic arterial cross-section, p_s is the systolic pressure which can be measured by commercial BP cuff. Using the aforementioned equation and a brief calibration for α and p_d , the accurate pressure waveform $p(t)$ can be achieved. It is worth noting that the vessel diameter measurement is critical from the equation above. The validation method on the diameter measurement accuracy adopted here is to compare the systolic diameter with that captured by the clinical ultrasonic machine at the same vascular location (Supplementary Fig. 14).

9.2 Calibration of the CVP

Central venous pressure (CVP), referring to the BP in the vena cava, is used as an essential clinical tool in ICU for cardiovascular status monitoring. Traditional CVP measurement in the ICU is based on implanting the central venous catheter. However, this method faces thrombo-embolic, infectious, and miscellaneous risks. Recently, techniques for ultrasound-guided volume assessment using the jugular vein diameter measurements have been developed⁴³⁻⁴⁵. Several studies that use ultrasound-measured jugular vein parameters to estimate the CVP have been reported⁴⁶⁻⁴⁸. The relationship between the CVP and the cross-sectional area (CSA) is⁴⁹:

$$CVP = 4.21 + 2.15 \times CSA \quad (4)$$

We assume the cross-section is rotationally symmetrical. Then the formula can be written as:

$$CVP = 4.21 + 0.54 \times \pi d^2 \quad (5)$$

where d is the vessel diameter extracted from our ultrasound measurement. Therefore, we derived the normalized pressure waveform as:

$$Normalized\ Pressure(t) = \frac{4.21+0.54 \times \pi d(t)^2}{4.21+0.54 \times \pi d_{max}^2} \quad (6)$$

There is a minor disadvantage with the CVP measurement method, which lies in the assumption of the circular vein cross-section. In most cases, the cross-sections of the vein are elliptical. Although this method has this minor disadvantage that can be improved by refining the relationship equation, the monitoring of central vein pulsatile is of high clinical significance. Its waveform can indicate the right heart functionality, as discussed in Supplementary note 13.

9.3 Calibration coefficient

Every waveform reported in the manuscript has been calibrated with a commercial pressure cuff. We need to calibrate our device only once as long as there is no significant physiological change or vascular reconstruction of the subject. This is because although the pulse pressure varies from beat to beat, the diastolic pressure maintains relatively stable under a constant physiological status.

According to equations (1) and (2), the relationship between the measured signal, arterial diameter, and the actual value of a determined physical quantity, BP, can be expressed as follows:

$$\ln p(t) = (\ln p_d) \cdot \alpha \cdot \left[\frac{d^2(t)}{d^2_D} - 1 \right] \quad (7)$$

where d_D is the minimum diameter in one cardiac cycle, corresponding to the diastolic BP. Here, the true value $\ln p(t)$ is proportional to the signal $\frac{d^2(t)}{d^2_D} - 1$. The calibration coefficient f can be defined as the ratio between these two:

$$f = \frac{\ln p(t)}{\frac{d^2(t)}{d^2_D} - 1} = \alpha \cdot \ln p_d \quad (8)$$

The calibration coefficient f depends on the diastolic pressure p_d and the rigidity coefficient α . These two parameters vary on different subjects and are calibrated every time in different physiological states (e.g., before or after exercise). The rigidity coefficient can be calibrated as following:

$$\alpha = \frac{A_d \ln(p_s/p_d)}{A_s - A_d} \quad (3)$$

where p_s is the systolic pressure, and A_s is the systolic arterial cross-section. Through the arterial tree, α and p_d do not change significantly⁵⁰. Thus, calibration of the brachial artery can be used to obtain BP waveforms at different sites such as the wrist, neck, and the foot on the same subject. In other situations, as long as the α and p_d do not change significantly, the device does not need frequent re-calibration.

9.4 CBP measurement validation

Commercial tonometer could provide a noninvasive assessment of both PBP and CBP waveforms. When combined with ECG electrodes, ECG correlation based PWV measurement is achievable. A *SphygmoCor EM3*[®] device shown in Supplementary Fig. 39, which is approved by FDA, can provide CBP waveforms and PWV measurements. With mature tonometer strain sensors and advanced algorithms, the commercial tonometer is the most widely accepted gold standard for noninvasive CBP waveform monitoring.

To characterize the accuracy of CBP measurements using our ultrasound device, we measured carotid BP waveforms using both our conformal ultrasound sensor and the *SphygmoCor EM3*[®]. A healthy subject is in a static situation, and the measurements using both methods are conducted in close succession to avoid large physiological status changes of the subject. The morphology of the measured waveforms is with high fidelity (Supplementary Fig. 29a). The cross-correlation of the waveform in Supplementary Fig. 29b is 0.94. And the measured differences of systolic pressure and dicotic notch are both within an acceptable range (Supplementary Fig. 29c). According to the widely accepted AAMI SP10 Protocol⁵¹, the standard BP monitoring device's error tolerance is as high as 5 mmHg. Our measurement results of 0.05 mmHg for systolic pressure and 0.28 mmHg for dicotic notch are well below this tolerance threshold.

Supplementary note 10: Strain on the skin.

The skin can be approximated as a bilayer, which consists of the epidermis and dermis. This bilayer exhibits a linear elastic response to tensile strains <15%, which transitions to non-linear behavior at higher strain levels. Failure occurs when skin reaches 30% strain level⁵². Our device is encapsulated by silicone and has mechanical properties well matched to the epidermis, giving conformal and intimate contact to the texture on the skin surface. Thus, as long as the skin itself has no rupture, our device with 30% elastic strain will be sufficient for accommodating any motion of the skin.

Supplementary note 11: Measurement uncertainty, accuracy, and precision.

The measurement uncertainty, accuracy, and precision of our device are evaluated and compared with those of the non-invasive gold standard instrument (*SphygmoCor EM3*[®]), an FDA approved tonometer for BP waveform measurements⁵³. The following evaluation demonstrates our devices' excellent capability to measure with lower uncertainty, higher accuracy, and higher precision compared with the tonometer.

11.1 Measurement uncertainty evaluation

The relation between vessel cross-section area waveform $A(t)$ and BP waveform $p(t)$ appears as follows:

$$p(t) = p_d \cdot e^{\alpha \left(\frac{A(t)}{A_d} - 1 \right)} \quad (1)$$

$$\alpha = \frac{A_d \cdot (\ln p_s - \ln p_d)}{A_s - A_d} \quad (3)$$

where the BP waveform $p(t)$ is a function of systolic pressure p_s , diastolic pressure p_d , vessel cross-section area waveform $A(t)$, systolic cross-section area A_s , and diastolic cross-section area A_d . A_s and A_d are defined as the maximum and minimum values of $A(t)$ in one cardiac cycle, respectively. $A(t)$ is calculated from the diameter waveform $d(t)$ based on the assumption that the blood vessel is rotationally symmetrical. Their relation is shown as follows:

$$A(t) = \frac{\pi d^2(t)}{4} \quad (2)$$

Overall, the relation is shown as follows:

$$p(t) = p_d \cdot e^{\frac{A_d \cdot (\ln p_s - \ln p_d)}{A_s - A_d} \times \left(\frac{\pi d^2(t)}{4A_d} - 1 \right)} \quad (9)$$

Thus, to evaluate the measurement uncertainty of $p(t)$, individual uncertainty of each input variables should be evaluated. The combined measurement uncertainty of $p(t)$ is calculated based on the assumption that there are no correlations between each one of the input variables, since all of them are measured independently.

11.1.1 Measurement uncertainties of p_s and p_d

The systolic pressure p_s and diastolic pressure p_d are measured with a commercial BP cuff which provides a relative uncertainty $U_{prel} = 1\%$ ⁵⁴.

11.1.2 Measurement uncertainty of $d(t)$

$d(t)$ is the measured vessel diameter waveform. Our ultra-thin and skin compatible ultrasonic device can provide a reliable measurement of the vessel diameter without squeezing the blood vessel as in the case of tonometer. We conducted repeated measurements to derive the standard deviation of the results that is defined as the A type uncertainty, which is more appropriate for repeated measurements than the B type uncertainty⁵⁵. Vessel diameters corresponding to the diastolic BP (d_D), systolic BP (d_S), and

BP at the dicrotic notch (d_N) on a radial artery of the same subject are all measured for 15 times. The measurement results are summarized in the Table 1.

Table 1. Diameter Measurement of the Radial Artery*

NO.	d_D /mm	d_S /mm	d_N /mm
1	2.436	2.563	2.547
2	2.436	2.562	2.547
3	2.437	2.563	2.546
4	2.435	2.563	2.546
5	2.435	2.562	2.545
6	2.436	2.563	2.547
7	2.437	2.562	2.547
8	2.437	2.563	2.546
9	2.435	2.563	2.546
10	2.435	2.562	2.546
11	2.436	2.563	2.547
12	2.437	2.563	2.547
13	2.436	2.563	2.546
14	2.435	2.563	2.546
15	2.436	2.563	2.546
AVERAGE	2.436	2.563	2.546

* d_D , d_S , and d_N correspond to the radial artery diameter for diastolic BP, systolic BP, and BP at the dicrotic notch, respectively. All data are obtained from the same subject within the duration of 10 minutes so the fluctuation in physiological conditions of the subject is negligible.

The standard deviation of the mean is defined as the following⁵⁵

$$U_d = \left(\frac{1}{n \cdot (n-1)} \sum_{k=1}^n (d_k - \bar{d})^2 \right)^{\frac{1}{2}} \quad (10)$$

Therefore, we can obtain:

$$U_{d_D} = 0.0002 \text{ mm}; \text{ the relative uncertainty } U_{rel d_D} = \frac{U_{d_D}}{\bar{d}_D} = 0.0082\%$$

$$U_{d_S} = 0.0001 \text{ mm}; \text{ the relative uncertainty } U_{rel d_S} = \frac{U_{d_S}}{\bar{d}_S} = 0.0039\%$$

$$U_{d_N} = 0.0002 \text{ mm}; \text{ the relative uncertainty } U_{rel d_N} = \frac{U_{d_N}}{\bar{d}_N} = 0.0079\%$$

The maximum relative uncertainty of these three measurements is considered to be the relative uncertainty of the overall vessel diameter measurement:

$$U_{rel d} = \frac{U_d}{\bar{d}(t)} = \max\{U_{d_D}, U_{d_S}, U_{d_N}\} = 0.0082\%$$

11.1.3 Measurement uncertainties of A_s and A_d

A_s and A_d represent the maximum (systolic) and minimum (diastolic) vessel cross-section area, respectively. Based on the relation between the vessel cross-section area and vessel diameter, A_s and A_d can be calculated as:

$$\frac{U_{A_s}}{A_s} = \frac{U_{A_d}}{A_d} = \frac{d A(t)}{d d(t)} \cdot \frac{U_d}{d(t)} = \frac{2U_d}{d(t)} = 0.016\%$$

The uncertainties of A_s and A_d are the same since they are derived using the same method.

11.1.4 Combined measurement uncertainty of $p(t)$

With predefined input variables' uncertainties and the calculating function, the measurement uncertainty of $p(t)$ can thus be calculated as⁵⁶:

$$p_t(p_s, p_d, d(t), A_s, A_d) = p_d \cdot e^{\frac{A_d \cdot (\ln p_s - \ln p_d)}{A_s - A_d} \times \left(\frac{\pi \times d^2(t)}{4A_d} - 1 \right)} \quad (9)$$

$$U_{p_t}^2 = \left(\frac{\partial p_t}{\partial p_s} \right)^2 \cdot U_{p_s}^2 + \left(\frac{\partial p_t}{\partial p_d} \right)^2 \cdot U_{p_d}^2 + \left(\frac{\partial p_t}{\partial d} \right)^2 \cdot U_d^2 + \left(\frac{\partial p_t}{\partial A_s} \right)^2 \cdot U_{A_s}^2 + \left(\frac{\partial p_t}{\partial A_d} \right)^2 \cdot U_{A_d}^2 \quad (11)$$

Finally, we use MATLAB[®] to calculate the combined uncertainty $U_{p_t} = 0.65$ mmHg when the measured $p(t) = 90$ mmHg. The relative uncertainty $U_{rel p_t}$ appears as follows:

$$U_{rel p_t} = \frac{U_{p_t}}{p_t} = 1.0\%$$

According to the combined relative uncertainty, we believe that the actual BP value is within the uncertainty line (blue dash line in Supplementary Fig. 22). In practical measurements, the difference between real BP value and corresponding measurement results should be less than 1.5 mmHg.

The uncertainty curve in Supplementary Fig. 21 shows the uncertainty as a function of the measured BP results. The measurement uncertainty of our wearable ultrasonic bandage is smaller than the commercial tonometer BP device: *SphygmoCor EM3*[®], which is an FDA approved BP monitoring device based on tonometry, providing a relative uncertainty of 2%⁵⁷.

11.2 Measurement accuracy and precision evaluation

According to the widely accepted BP monitoring evaluation method AAMI SP10⁵¹, accuracy is determined by the mean difference between the tested device and the standard measurement instrument (mercury sphygmomanometer). Precision is determined by the standard deviation of the measured results of the tested device. We conducted tests with our ultrasound device on three healthy subjects. Diastolic arterial pressure (DAP), systolic arterial pressure (SAP), and mean arterial pressure (MAP) are measured for 20 times under the same physiological circumstances.

The average (AVG) and standard deviation (SD) of BP values from the different subjects are summarized in the Table 2.

The standard deviations (SDs), i.e., the measurement precisions, are within 2 mmHg. According to the widely accepted AAMI SP10 Protocol⁵¹, the device with a measurement

standard deviation lower than 8 mmHg is recommended for the clinical use. Apparently, our ultrasound device's precision qualifies for the clinical use.

Table 2. Average and standard deviation of the BP measurement

	DAP/mmHg		SAP/mmHg		MAP/mmHg	
	AVG	SD	AVG	SD	AVG	SD
Subject 1	69.10	0.86	131.85	1.25	90.01	0.63
Subject 2	75.98	0.89	125.04	1.59	92.33	0.85
Subject 3	72.99	0.85	127.15	1.52	91.04	0.66

The mercury sphygmomanometer is the most reliable BP measurement method, which is normally considered as the reference of accuracy evaluation. Standard BP values of the three subjects are measured by the mercury sphygmomanometer to compare with the results from our device (shown in the Table 3).

According to the AAMI SP10 Protocol⁵¹, a clinically acceptable difference of the mean should be less than 5 mmHg. The measured BP values using our device are 100% within the tolerable accuracy range of 5 mmHg in all three subjects, which means our ultrasound device is adequately qualified from the accuracy aspect. In addition, according to the widely accepted 1993 modified BHS protocol⁵⁸, the device satisfies the requirements for grade 'A' accuracy, which is designed for the highest level of clinical use. The results are also summarized in the Table 3.

Table 3. BP measurement comparison between the conformal ultrasonic sensor and the mercury sphygmomanometer

		This work	Sphygmomanometer	Accuracy
Subject 1	DAP	69.10	72	-2.9
	SAP	131.85	132	-0.15
	MAP	90.01	89	1.01
Subject 2	DAP	75.98	75	0.98
	SAP	125.04	124	1.04
	MAP	92.33	95	-2.67
Subject 3	DAP	72.99	77	-4.01
	SAP	127.15	129	-1.85
	MAP	91.04	93	-1.96

Supplementary note 12: Challenges of current approaches for BP waveform monitoring.

Existing approaches for long-term BP waveform measurements have three significant limitations: the inaccuracy and operator dependency, the lack of a precise long-term monitoring modality, and the incapability of serving in a severe environment.

1) Inaccuracy and operator dependency

Carotid artery pressure waveform recorded by the applanation tonometry is often used as an alternate for the aortic pressure because of the close proximity of these arterial sites. However, carotid waveforms of high quality can be difficult to obtain in all individuals, especially in obese patients. This technique is highly operator-dependent, making it unreliable for self-monitoring and routine high-throughput screening of CBP in a non-specialist setting^{36,37}. Cannulation is the most accurate method for measuring CBP, but it is too invasive to allow frequent measurements, which are needed for all-cause cardiovascular mortality prediction. Non-invasive solutions, such as photoplethysmography, cannot penetrate deep enough into the tissue to consistently measure the CBP of the carotid artery. The operator-dependency of tonometry is demonstrated in Supplementary Fig. 24. Although this is the current non-invasive gold-standard technique, it is highly operator-dependent, creating significant challenges for accurate and reliable measurements on blood vessels that are deep underneath the skin. The operator-dependency is reflected by the fact that either tiny offset from the central arterial axis or moderate holding forces of the tonometry probe will introduce tremendous recording error of the BP waveforms (Supplementary Fig. 24). To solve those challenges, our wearable approach transforms the measuring probes into ultrathin, light-weight, and stretchable “skin-like” membranes that are capable of conformally laminating on the skin surface. Additionally, our wearable approach avoids operator-dependency. This is because the 2-D array design of the device with small pitch between the transducers enables the vessel localization. As a consequence, the user can obtain signals with excellent quality without the need for accurate aligning to the target vasculature as in the case of tonometer. The related demonstration appears in Supplementary note 6 and Supplementary Fig. 11.

2) Lack of a precise long-term monitoring modality

BP waveform is one of the most dynamic vital signs corresponding directly to heart activities⁴¹. However, the traditional method of taking a small number of readings with the auscultatory technique gives only two discrete values. Therefore, all of the other information except the systolic pressure and diastolic pressure, is totally missing. Additionally, this traditional method often provides a poor estimate of risks in an individual patient for reasons such as the poor technique of the observer, also known as the “white-coat” effect⁴², resulting from the inherent variability of BP waveform⁴³. Although, ambulatory monitoring based on the sphygmomanometer cuff has been developed to improve the estimate of the true BP. Its application is still restricted to a minor group of patients due to the limited sampling rate (once every 15 to 30 minutes), bulky size (often 10 by 8 by 3 cm³), and heavyweight (~ 2 kg)⁴⁴. Although the instrument can be taken with the subjects themselves, the method still causes inconvenience to their daily life. Thus, most ambulatory monitoring only records BP for a relatively limited time. To solve those challenges, we designed this technique that can provide CBP measurement and waveform monitoring precisely to every heartbeat in a lightweight and mechanically invisible manner. Ecologically, this offers the availability of a comfortable, non-invasive BP monitoring device that can shift the public perception of the concept of the BP (i.e., from “discrete” to “continuous”). And, it raises patient awareness. Additionally, it can be translated into more effective preventive care and a significant

reduction in associated mortality and healthcare costs. Finally, our conformal probe is low-cost and could be disposable. The conformal probe is assembled using the low-cost materials that include the 1-3 composite, Cu electrode, and silicone. Considering those material and machining costs, the overall expense of one conformal probe is much lower than the commercially available ultrasound probe.

3) Incapability of serving in severe environments

Continuous BP monitoring of people serving in a harsh environment, e.g., the battlefield, is a remaining challenge. For example, cerebrovascular blood supply is vital for the fighter pilot, which is closely related to the CBP. In combats especially during climbing, because of the significantly increased gravity, blood is pulled to lower areas of the body resulting in abnormal CBP and deprived blood supply to the brain and thus pilots' passing out. Modern aircraft could reach 9G acceleration or higher, which is extremely difficult for pilots to tolerate. Although technologies like the anti-G suit are well developed for high acceleration protection, well-trained pilots will still experience visual impairment or even G-LOC (G-induced loss of consciousness) if the high G-force sustains for more than a few seconds⁴⁵. Many fatalities are reported in which the aircraft and crew are lost due to G-LOC⁵⁹. Thus, developing a method providing continuous monitoring of the pilots' CBP and cerebrovascular blood supply is of great significance in preventing G-LOC from happening.

Aforementioned existing approaches for CBP monitoring are not suitable for this particular need. Invasive catheters, which are typically used in intensive care units (ICUs), will introduce bleeding, making it impossible for practical application in actual combat circumstances. The noninvasive tonometer is not possible either. A tonometer probe needs to be held on the target artery for measurements and its reliability closely related to the precision of position. These features make these methods impossible to be applied in a drastic aerial combat circumstance. On the contrary, our wearable ultrasound approach demonstrates remarkable advantages in this case. Ultrasound can penetrate deep tissues and perform the CBP monitoring task. Most importantly, due to its lightweight and mechanical compliance, the bandage can be mounted on the skin bringing minimum mechanical constraints to pilots and avoiding relative displacement between the device and the target artery. This feature allows collecting reliable CBP waveforms, which can be used as a robust G-LOC indicator for pilots and will therefore significantly improve the aviation safety and combat capabilities of the pilots.

In all, by providing easy access to the critical CBP waveform automatically, our device will appear as a powerful technique for care-providers to precisely assess the situation of patients, for researchers to do detailed statistic studies on CBP, and for the public to do better health self-management.

Supplementary note 13: Clinical significance of BP waveform.

BP waveform is a highly dynamic, ever-changing meaningful data that can give a lot of implications for human cardiovascular status. This variability is closely related to the fluctuating cardiovascular states. The BP waveform contains three different components that can serve as the direct indicator of corresponding cardiovascular status. This critical information has a high significance that necessitates wearable, continuous, and long-term monitoring.

13.1 Arterial BP waveform

The arterial pressure waveform is related to the left heart activity. During each heartbeat, BP varies between systolic and diastolic pressure levels. The BP in the circulation is in principle due to the pumping action of the heart. Three components of the arterial BP waveform are discussed as follows.

1) Systolic phase

Continuous monitoring the systolic phase allows the observation of sudden stenosis at the aortic valve. Specifically, the systolic phase is the first phase of the cardiac cycle, characterized by a rapid increase in pressure to a peak value, followed by a rapid decline. The systolic peak indicates blood is ejected forward to the peripheral arteries. This phase begins with the opening of the aortic valve and corresponds to the left ventricular (LV) ejection. The slope of this segment has a close relationship with the rate of change in LV pressure and the competence of the aortic valve³⁰. Consequently, when the ventricle pumps blood through the stenosed aortic valve, the systolic upstroke becomes less steep. Therefore, by analyzing the systolic phase, one can perform the diagnosis on whether the valve is blocked³¹. Besides the diagnosis of valvar blockage, the slope of the waveform upstroke can also evaluate the myocardial contractility⁶⁰. An increased upstroke gradient suggests a more significant pressure generated per unit time by myocardial muscle. More interestingly, a bisferiens appearance (double peaks) on the systolic peak can indicate the aortic regurgitation of the subject.

2) Dicrotic notch

The dicrotic notch is a reflected wave propagating backward from the peripheral arteries to the central artery. In a normal healthy person, the reflection wave will return in the diastolic phase, after the closure of the aorta valves. This reflected wave benefits the perfusion from coronary arteries to the heart. Therefore, the reflected wave velocity becomes very important: the stiffer the arteries are, the faster it returns. This reflection velocity is derived from PWV. In addition, continuous monitoring of dicrotic notch can indicate the aortic regurgitation and stenosis³². The notch is labeled in Supplementary Fig. 31, which represents the closure of the aortic valve. By analyzing the activity of aortic valve, one can acquire critical information that is essential for diagnosing the valvular disease³³. To be more specific, if the notch is blurred, it is highly indicative of aortic stenosis and aortic regurgitation⁶¹. Usually, the stenosis and regurgitation happen abruptly during daily activities, which justifies the necessity of wearable continuous monitoring.

3) Diastolic phase

The importance of wearable continuous monitoring of the diastolic decline is that it can provide insights for the compliance of large arteries. To be more specific, the diastolic phase

represents the blood run-off into the peripheral circulation. The diastolic run-off is the drop-in pressure that occurs after the aortic valve has closed. There is no flow from the LV, but pressure does not drop suddenly. Instead, it decreases gradually along an exponential curve³⁴. The reason for this behavior is arterial "cushioning," or the reservoir effect of pumping blood into an elastic tube, resulting in the declined shape of the waveform. This elastic recoil of large arteries contributes as much as 40% to the stroke volume. Therefore, the shape of this reservoir pressure has a relationship with the characteristics of the reservoir. The nice supple aorta of a young person is going to perform differently from the calcified barnacle-encrusted aneurysm aorta of an elderly smoker³⁵.

More detailed information is shown in Supplementary Fig. 31.

Besides the analysis of above three components, the analysis of the morphology of the distension waveform can also diagnose the accelerated aging and hypertension. To be more specific, pulse waveforms vary from different ages due to the PWV change. For a normal young person, where the arteries are generally compliant, the slow traveling reflected wave returns from the peripheral arteries during the diastole. With aging, PWV increases and the reflected wave travels faster and gives rise to a "shouldering" at the primary wave. This effect prolongs the systolic cycle and increases the workload and oxygen requirement of the heart muscles. The poor notch compromises the flow of the coronaries. In the elderly, further arterial stiffening causes the reflected waves to return much faster, and coincide very close to the systolic peak, resulting in an augmented wave. The heart now needs to contract even harder to overcome the reflected wave for a longer period. At the same time, the coronary artery perfusion is further compromised. Thus, assessment of PWV provides critical information to possible accelerated aging and vascular sclerosis^{62,63}.

13.2 Venous pressure waveform

The venous waveform has equal significance to the arterial BP waveform for continuous monitoring by wearable devices. This is because the hemodynamics in the artery has a close relationship with the left ventricle, atrium, and valves. However, the vein is closely related to the right ventricle, atrium, and valves. By analyzing both left and right sides of the cardiovascular status, one can acquire and achieve a comprehensive diagnosis of the entire heart.

Unlike the arterial BP waveform, the venous pressure waveform is difficult to obtain in a non-invasive way since its much lower amplitude than the arterial BP. Trained cardiologists discern pulses in jugular vein pressure (JVP) as signs indicating the state of the right atrium. JVP pulsation has a biphasic waveform⁶⁴. The A wave corresponds to the right atrial contraction. The peak of the A wave demarcates at the end of atrial systole. The C wave corresponds to right ventricular contraction causing the tricuspid valve to bulge towards the right atrium. The X descent follows the C wave and occurs as a result of the right ventricle pulling the tricuspid valve downward during ventricular systole. As stroke volume is ejected, the ventricle takes up less space in the pericardium, allowing relaxed atrium to enlarge. The X descent can be used as a measure of the right ventricle contractility. The V wave corresponds to venous filling when the tricuspid valve is closed, and venous pressure increases from venous return - this occurs during and following the carotid pulse. The Y descent corresponds to the rapid emptying of the atrium into the ventricle following the opening of the tricuspid valve.

Abnormal JVP waveforms relate to certain cardiovascular diseases. For example, prominent A wave means there is resistance to RA emptying or increased resistance to ventricular

filling. These symptoms may be a result of tricuspid stenosis, right heart failure, or pulmonary hypertension.

Also, the continuous monitoring of the jugular vein dilation can significantly facilitate the diagnosis of the central vascular pressure. When the jugular vein is visible, it is known as jugular vein distention (JVD). The JVD patient is common with a bulging neck vein formed by the distension of external jugular vein. Internal and external jugular veins run through the right and left sides of the neck. They bring blood from the head to the superior vena cava, which is the largest vein in the upper body. The vena cava runs to the heart, where blood arrives before passing through the lungs to pick up oxygen. Therefore, JVD is a sign of the increase of the CVP. And, the CVP can indicate how much blood is flowing back into the heart and how efficient the heart can move that blood into the lungs and the rest of the body.

Due to this close relationship between the JVD and the heart, the JVD is a symptom of several different cardiovascular problems. The JVD occurs when the CVP increases above a normal or healthy level. This can be caused by several conditions.

1) Right-sided heart failure

Heart failure means the heart has grown too weak to efficiently pump enough blood to meet the demands of the body. Right-sided heart failure usually develops after the individual has left-sided heart failure. The left ventricle pumps blood out along the aorta to elsewhere of the body. The right ventricle pumps blood to the lungs. When the left ventricle's pumping power weakens, fluid can back up into the lungs. This eventually weakens the right ventricle. When the heart's right side can't properly empty, blood can back up into the veins, causing them to bulge⁸³.

2) Pulmonary hypertension

Pulmonary hypertension occurs as the pressure in the lungs increases. And, this hypertension sometimes is a result of changes to the lining of the artery walls. This symptom can also lead to right-sided cardiac failure and JVD⁸⁴.

3) Tricuspid valve stenosis

Due to various physiological changes, the valve that separates the right atrium and the right ventricle can become stiff. As a result, it may be incapable of opening up enough to let all the blood in the atrium flow into the ventricle. Therefore, blood can back up in the atrium, leading to a backup of blood in the veins, including the jugular vein, causing them to distend⁸⁵.

4) Superior vena cava obstruction

Superior vena cava obstruction is a kind of rare condition, which usually derives from a tumor in the chest that restricts blood flow in this large vein⁸⁶.

5) Constrictive pericarditis

The pericardium is a thin, fluid-filled sac that embraces the heart. An infection of the pericardium, as known as constrictive pericarditis, can restrict the volume of the heart. As a result, the chambers can't fill with blood in a proper way, so blood can back up into the veins, e.g., the jugular veins⁸⁷.

In all, those components of morphology in the BP waveform can bring a lot of information that is clinically meaningful. And it would be best if those data can be long-term monitored and analyzed properly. In this way, individuals can sense their cardiovascular status and prevent diseases from happening at an early stage.

Supplementary note 14: Simultaneous measurement of pulse pressure.

Since diastolic and pulse pressures vary on a beat-to-beat basis, data of pulse pressure should be measured simultaneously, which requires the multi-channel measurement. A circuit was designed for this purpose shown in Supplementary Fig. 51.

With this circuit, the pulse pressure at different sites can be measured simultaneously. A minor disadvantage of the current measurement setup is that the PRF of the data acquisition decreases to 50 Hz because the channel selection delay of each channel is 5 ms, and therefore, the waveform quality slightly degrades. The waveform quality can be improved by using high-speed channel selection chips to give shorter selection delay in future work.

The measurement results from the carotid to the brachial, radial, and foot arteries are listed and statistically analyzed as shown in Supplementary Fig. 35, which demonstrates the pulse pressure amplification from the central to the peripheral arteries. With the distance from the heart increasing, the corresponding pulse pressure amplification is obvious. The BP waveform data from our device highly correspond to the data from the commercial device.

Supplementary note 15: Medical value to measure the progressive change of BP waveforms.

Due to the close relationship between the progressive change of the waveform and physiological and pathological status, the amplification effect observed in clinical settings will contain abundant information related to age, gender, height, heart rate, as well as systematic diseases affecting the vasculature⁶⁵⁻⁶⁸. Furthermore, various clinical anti-hypertension treatments are reported to exert different influences on the central and peripheral arteries. By simultaneously observing the distension behavior of those arteries at different physical locations, the clinician can obtain valuable information on the efficacy of the cardiovascular disease therapy⁶⁹, e.g., BP lowering drugs. In all, that information, if being carefully collected and analyzed, can give various insights for individual cardiovascular systemic diagnosis and prognosis⁷⁰.

However, in the current clinical environment, those valuable data and signals can only be obtained by professionals in a considerably infrequent manner. And also, the current medical equipment for those data acquisition is highly operator dependent, limiting the accurate data acquisition. Comparing to those existing equipment, our conformal device can perform reliable and user-friendly measurements by directly observing the pulsatile behavior of human vasculature around the whole body. More importantly, in future work, we will incorporate all of the post-end circuits, including the transmitting/receiving units, data processing, and wireless communication modules, into the conformal probe by utilizing the island-bridge strategy⁷¹. This will allow continuous recording those vital signals in a continuous, long-term, and noninvasive manner.

Supplementary note 16: Pulse arrival time, pulse transit time and pulse wave velocity.

Physiologically, the PWV of the blood vessel can be expressed as:

$$PWV = \frac{Eh}{2r\rho} \quad (12)$$

where r is the internal radius of the blood vessel, h is the wall thickness, ρ is the blood density, and E is the artery modulus. In those parameters, the artery radius plays a dominating role, much more than the other three. The central artery has a larger diameter, and thus has the lower arterial stiffness, resulting in smaller pulse pressure. Likewise, arteries in the extremities have higher stiffness and thus possess more significant pulse pressure than the central arteries.

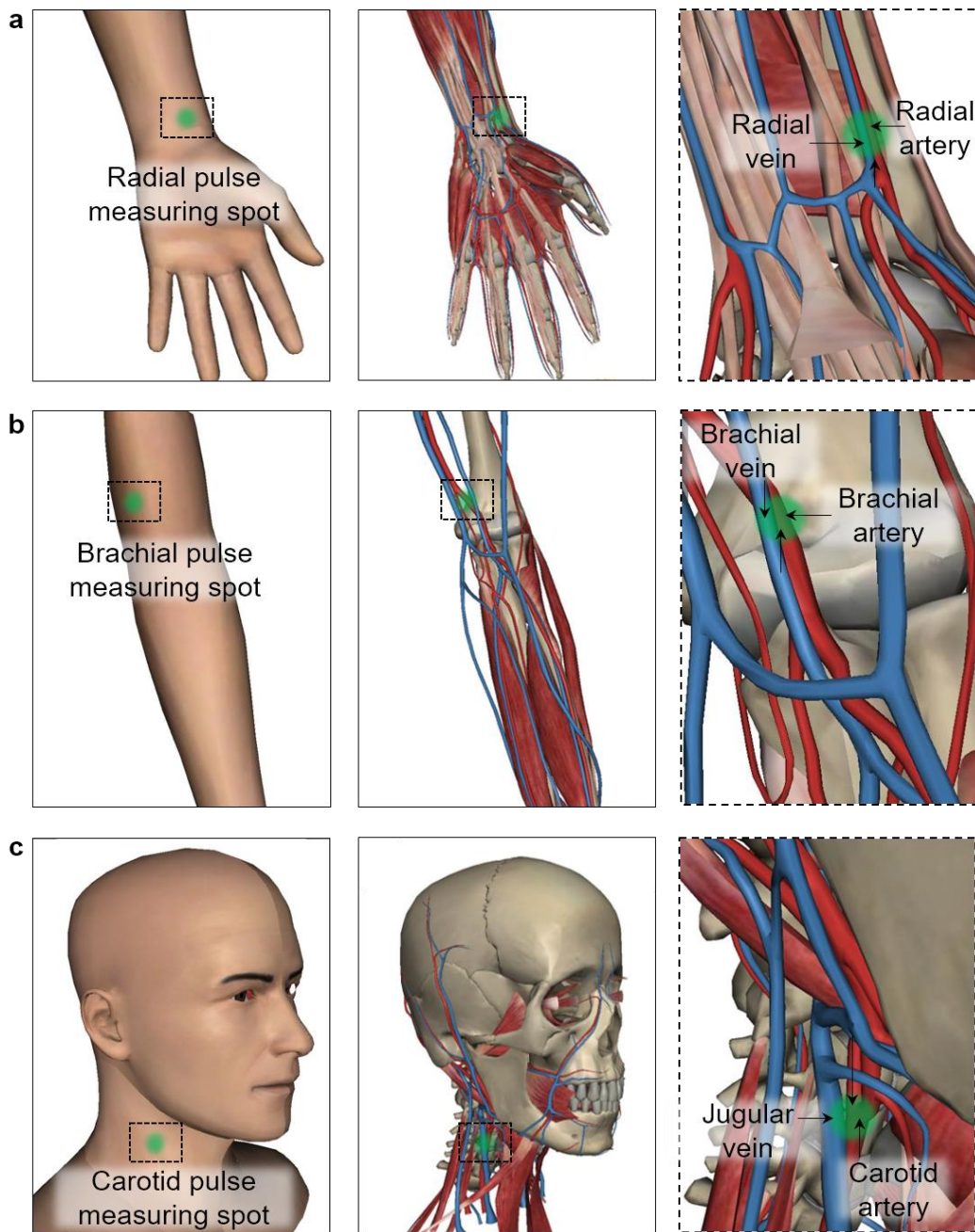
Another significance of PWV is its capability for absolute BP calculation with a simple calibration by a conventional BP cuff. The variation of the PWV can be utilized to correlate the absolute BP change, which is highly dependent on the arterial stiffness⁷².

PWV can be calculated using the known distance divided by the PTT, which is defined as the time it takes for the BP waveform to propagate through a length of the arterial tree. Literally, the PTT should be measured as the foot-to-foot time delay between the proximal and distal waveforms. In practice, the measurement of PAT, defined as the time delay between the R-wave of an ECG waveform and the distal arterial waveform foot, also serves as a surrogate for the PTT⁷³. PAT could also be used instead of PTT on different people⁷⁴. The method for calculating PAT and PTT is illustrated in Supplementary Fig. 52.

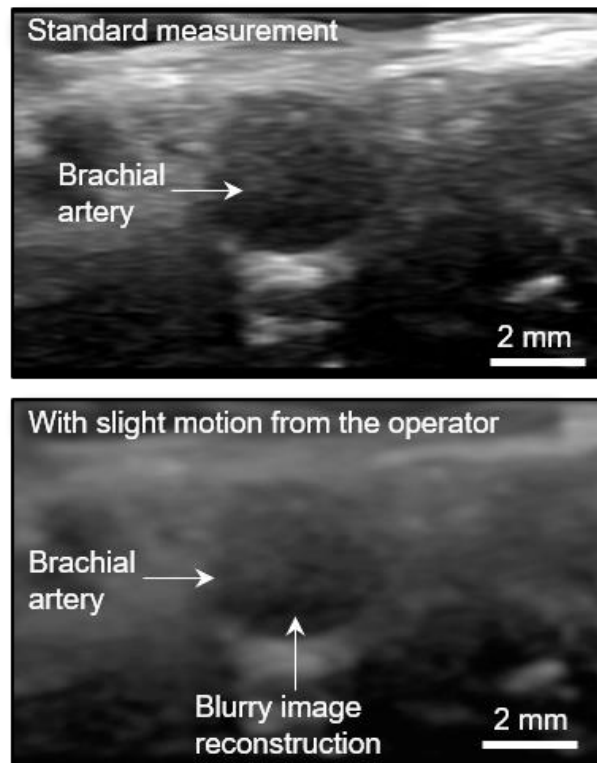
Supplementary Figures

Method Situation	Photoplethysmography	Tonometry	Ultrasound
Peripheral artery measurement			
Obese subject (Influence by thick fatty layer)			
Central artery measurement (Deeply buried and without supportive bony structures)			

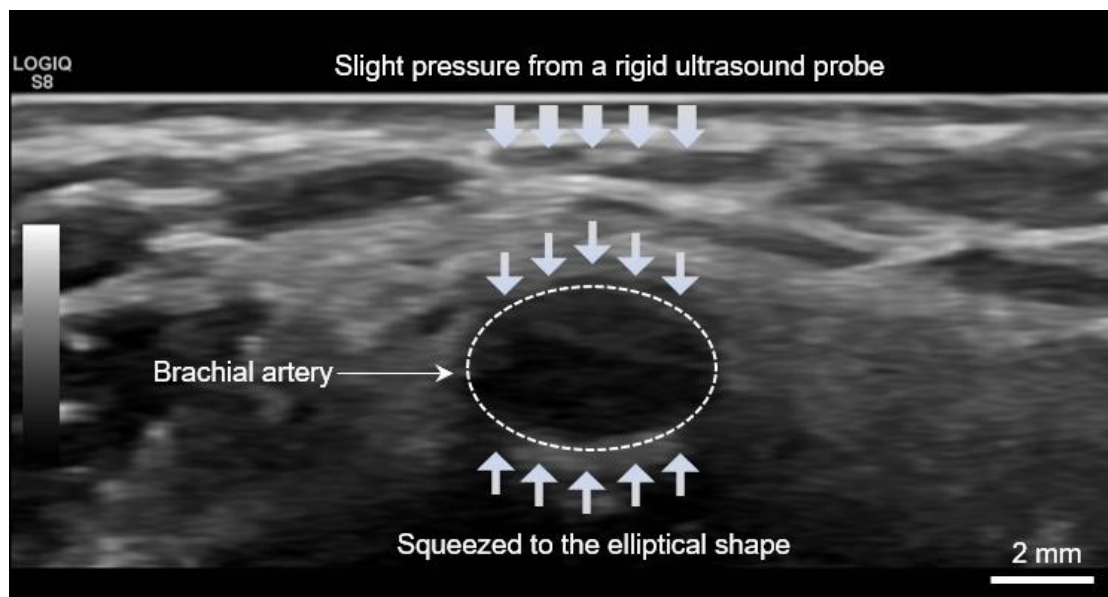
Supplementary Fig. 1. Comparison of BP measurements using different approaches in different situations. The comparison is focused on three major non-invasive BP waveform monitoring methods: PPG, tonometry, and ultrasound wall-tracking. The three situations are the normal condition, testing on obese people (with a thick fat layer, which is a large damper for all measurement strategies), and the central artery measurement (deeply buried, without proximal bony structures as support).



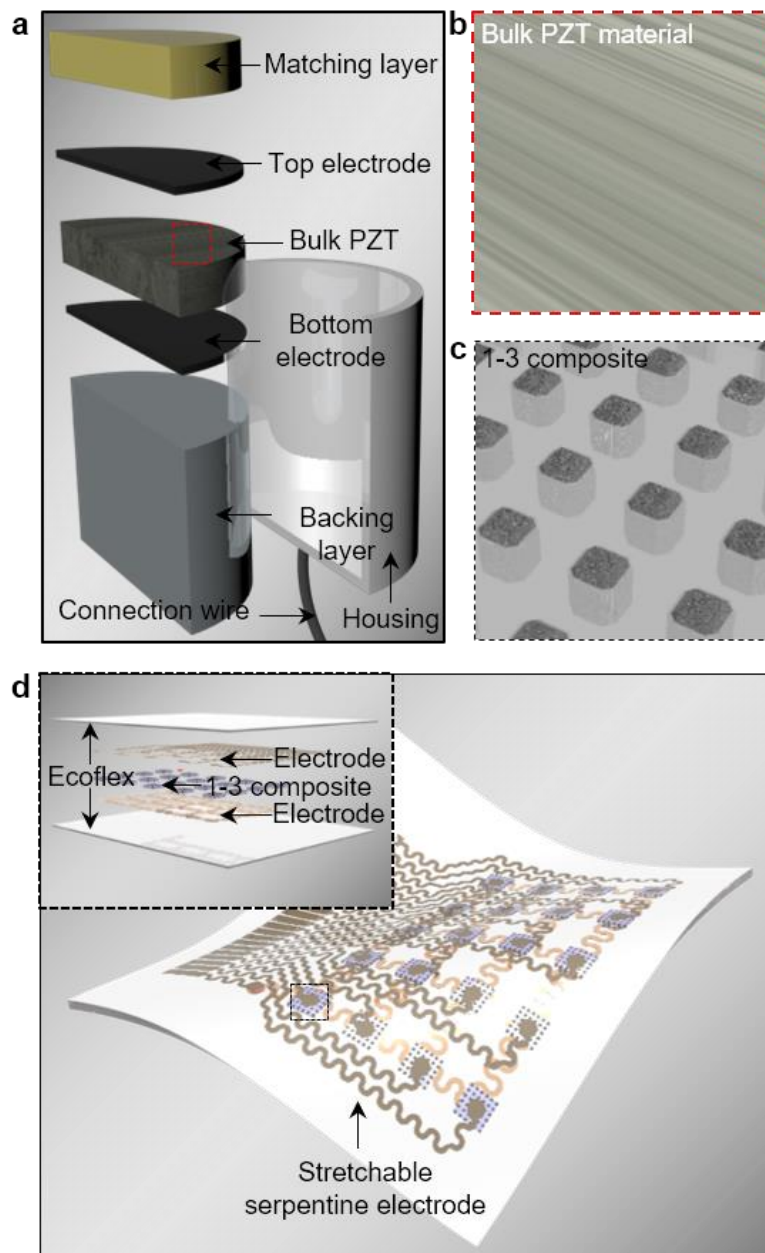
Supplementary Fig. 2. The anatomic structures of BP waveform testing spots. (a) Testing on the human wrist (radial pulsation), where the adjacent radial artery and vein are labeled. **(b)** Testing on the human arm (brachial position), where the adjacent brachial artery and vein are marked. **(c)** Testing on the human neck (carotid position), where the adjacent carotid artery and jugular vein are labeled. At the radial testing spot, the radial artery and radial vein are close to each other with high proximity. When we move to the brachial testing spot, the brachial artery and vein are overlapping with each other. This trend is the same when we perform the test on the carotid artery. The internal jugular vein overlays on the carotid artery. Those anatomic configurations will significantly limit the application of PPG and tonometer. The PPG will sense both the arterial and venous pulses at the same time due to the non-directional characteristics of light.



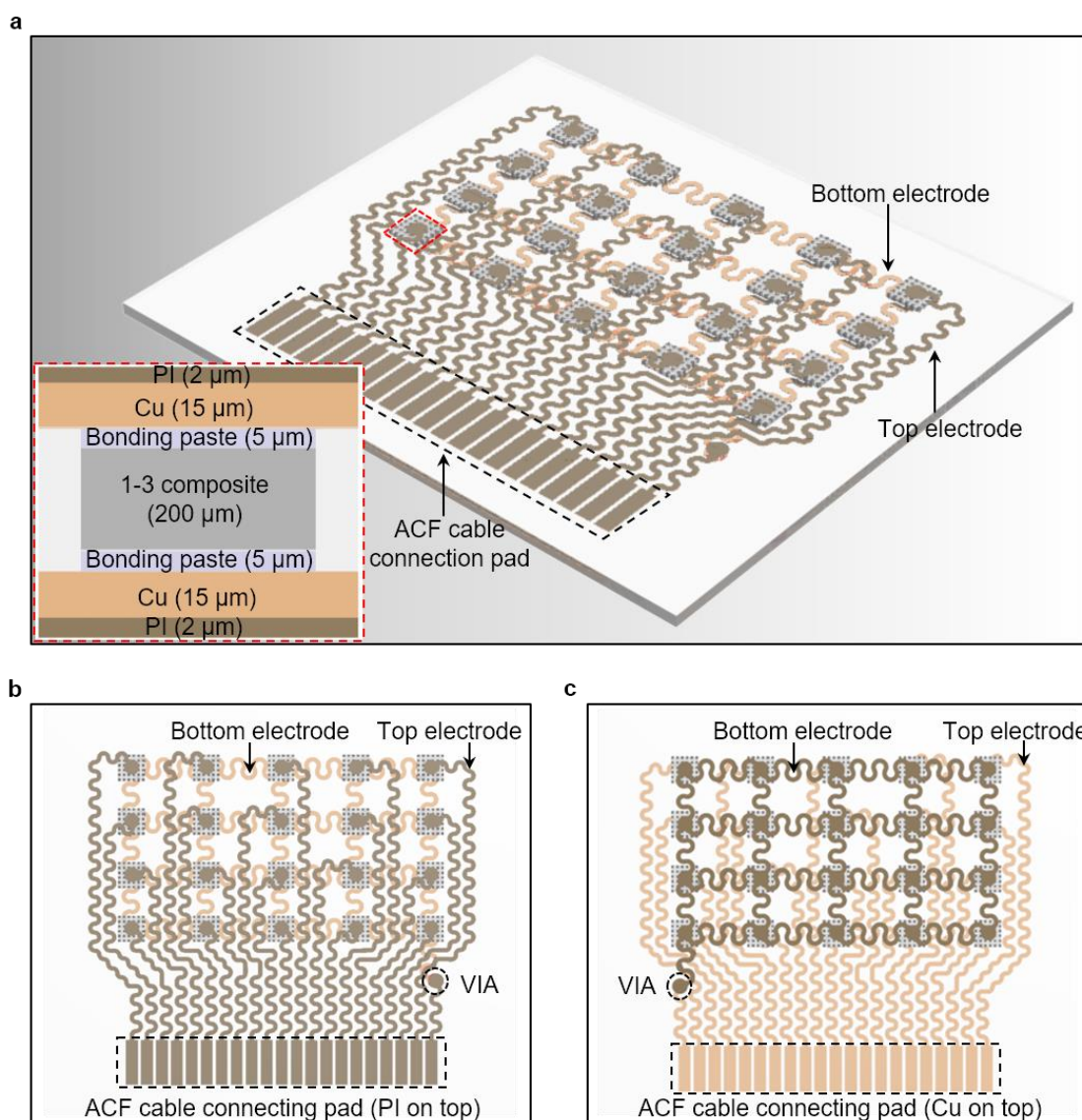
Supplementary Fig. 3. The effect of tiny operator movement on the image reconstruction quality using an ultrasound imaging probe. The top image shows a standard measurement. The bottom image demonstrates a blurred image reconstruction caused by inevitable motion artifacts from the operator.



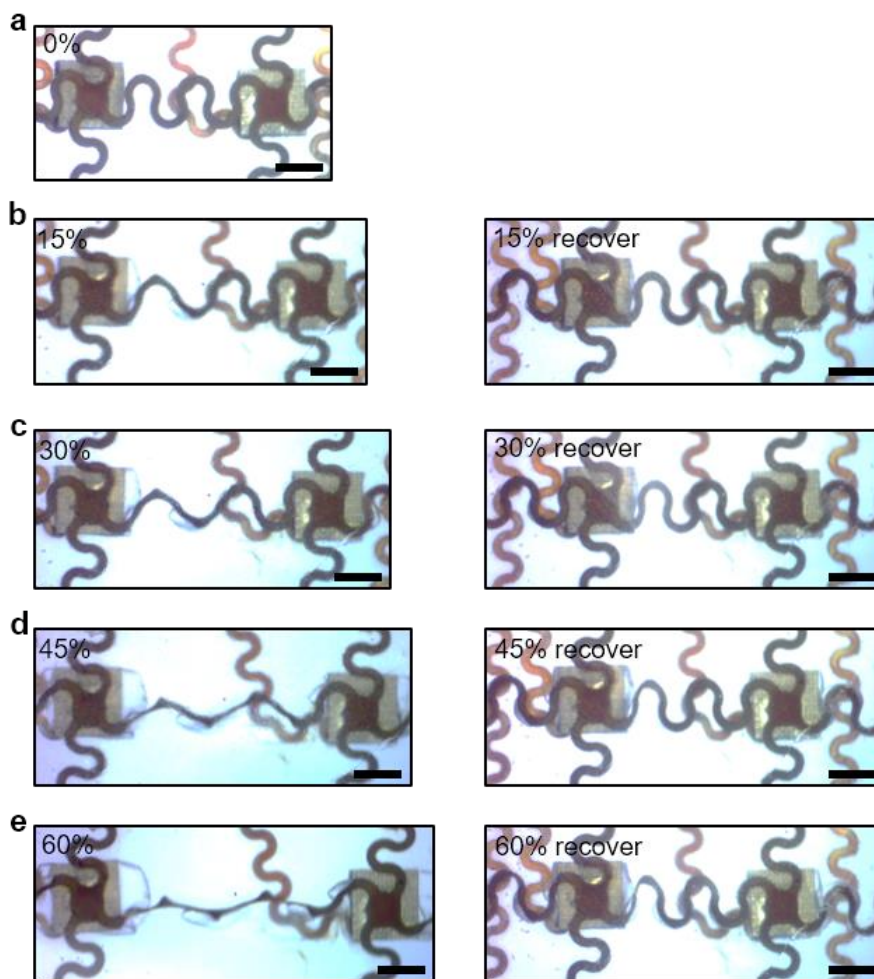
Supplementary Fig. 4. Vessel compression from holding the rigid ultrasound probe. This inevitable compression issue is brought by the mechanical or mass loading from the rigid ultrasound probe during the routine scanning process.



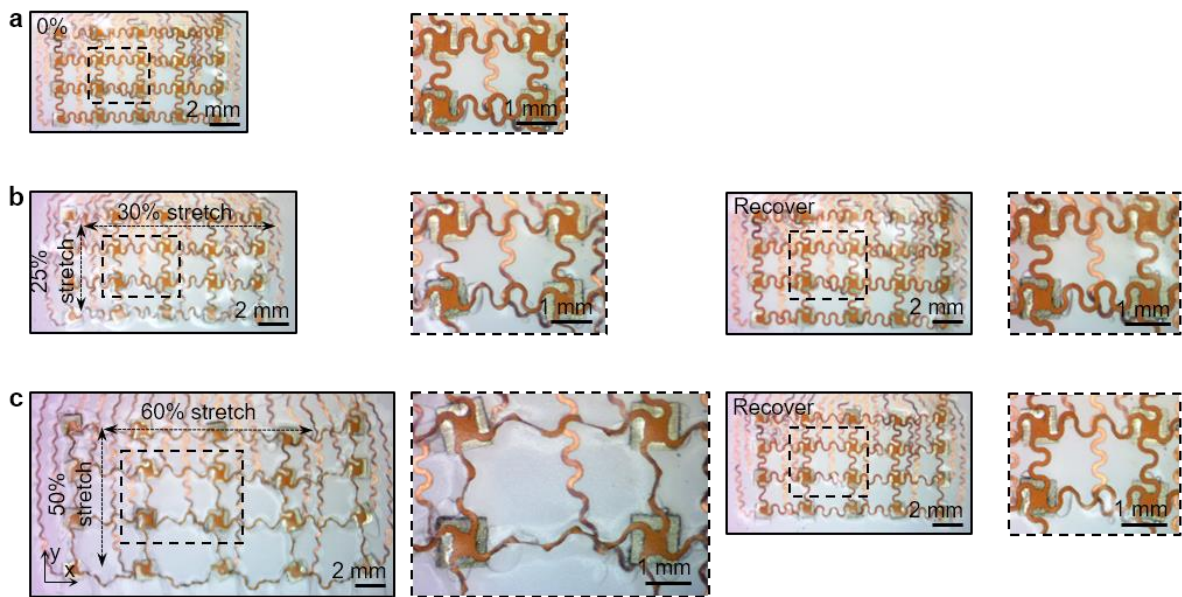
Supplementary Fig. 5. Comparison of the probe structure between the rigid and conformal ultrasonic devices. (a) The structural design of a traditional ultrasonic transducer, which contains a matching layer, top and bottom electrodes, bulk PZT materials, backing layer, housing, and connection wires. (b) and (c) are the comparison between the isotropic bulk PZT material and the anisotropic 1-3 composite. (d) An ultrathin and stretchable ultrasonic device, and its exploded view. The comparison between (a) and (d) shows our simplification and re-engineering strategies, which can be concluded as reducing the device thickness and substituting rigid materials with soft materials where necessary. The 1-3 composite can provide better acoustic matching to the tissue than the isotropic PZT, thus eliminating the necessity of the matching layer. Silicone elastomer encapsulation acts as a good dielectric and protective layer for the housing. The bottom Ecoflex layer serves as an acoustic damping layer, thus removing need for the backing layer.



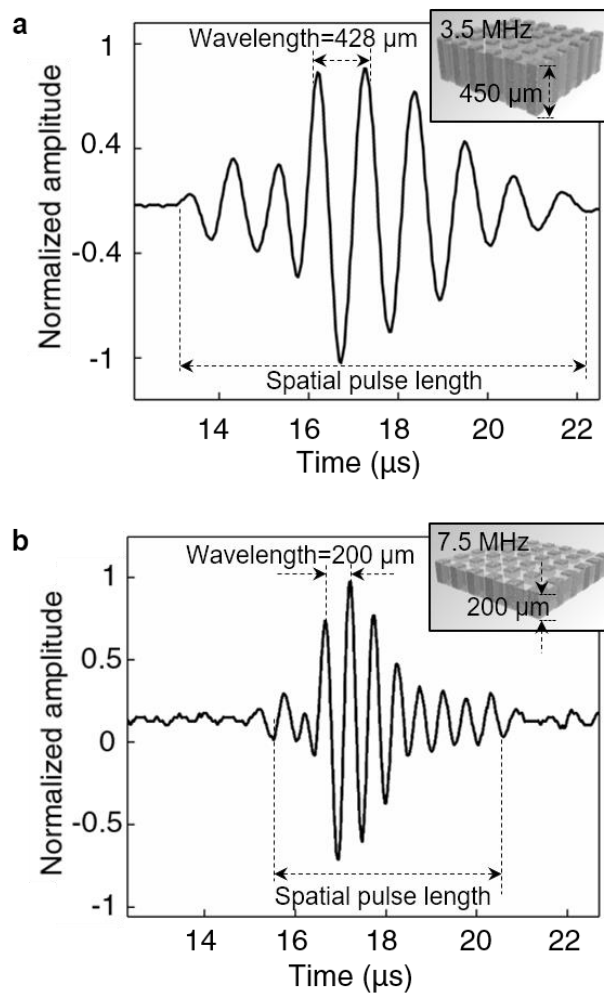
Supplementary Fig. 6. Device schematics and design layout. (a) The device under a flat state in a perspective view. The inset image is the cross-sectional structure. (b) The top view of the device. (c) The bottom view of the device.



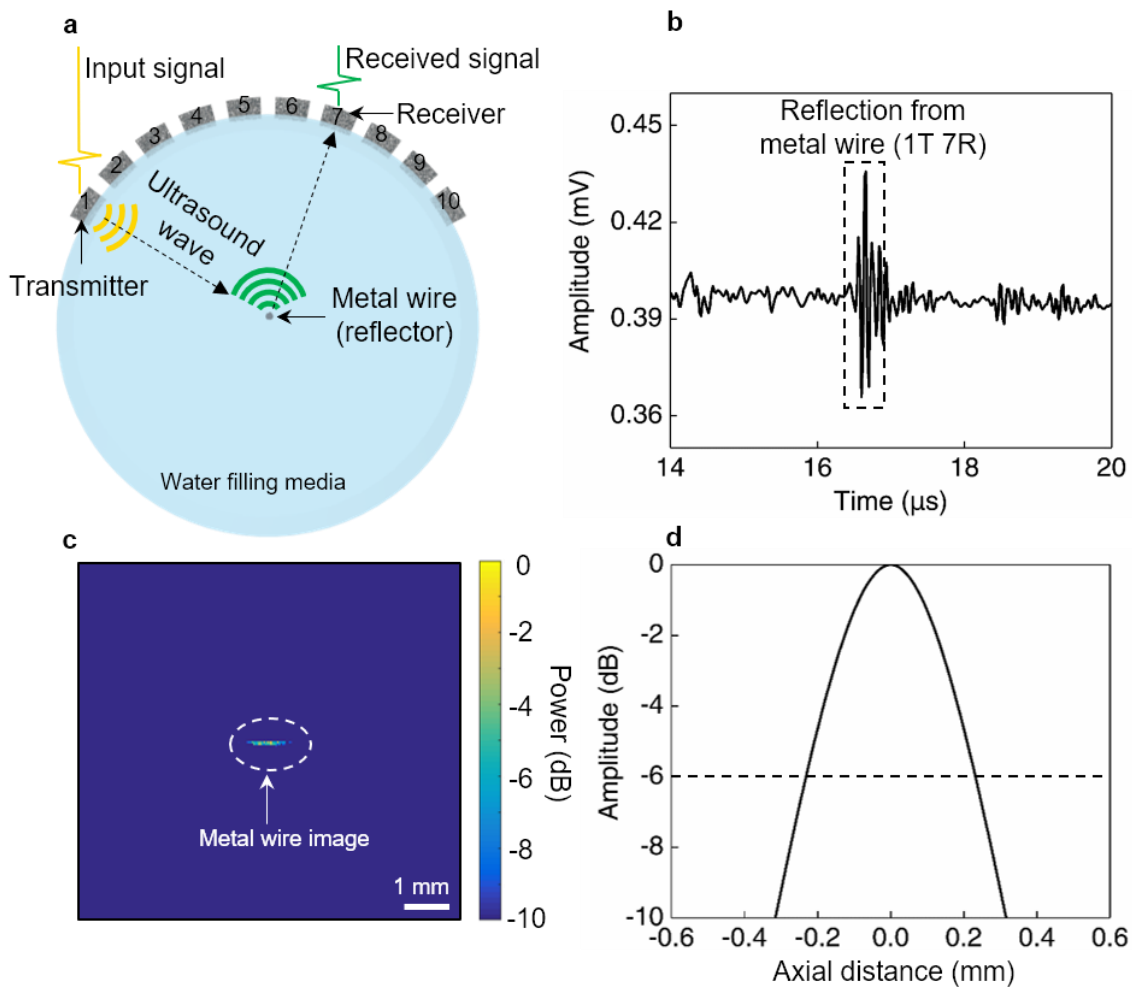
Supplementary Fig. 7. Photographs of the uniaxial tensile test. (a) The 0% original state. **(b)** The 15% tensile state and its recovery. **(c)** The 30% tensile state and its recovery. **(d)** The 45% tensile state and its recovery. **(e)** The 60% tensile state and its recovery.



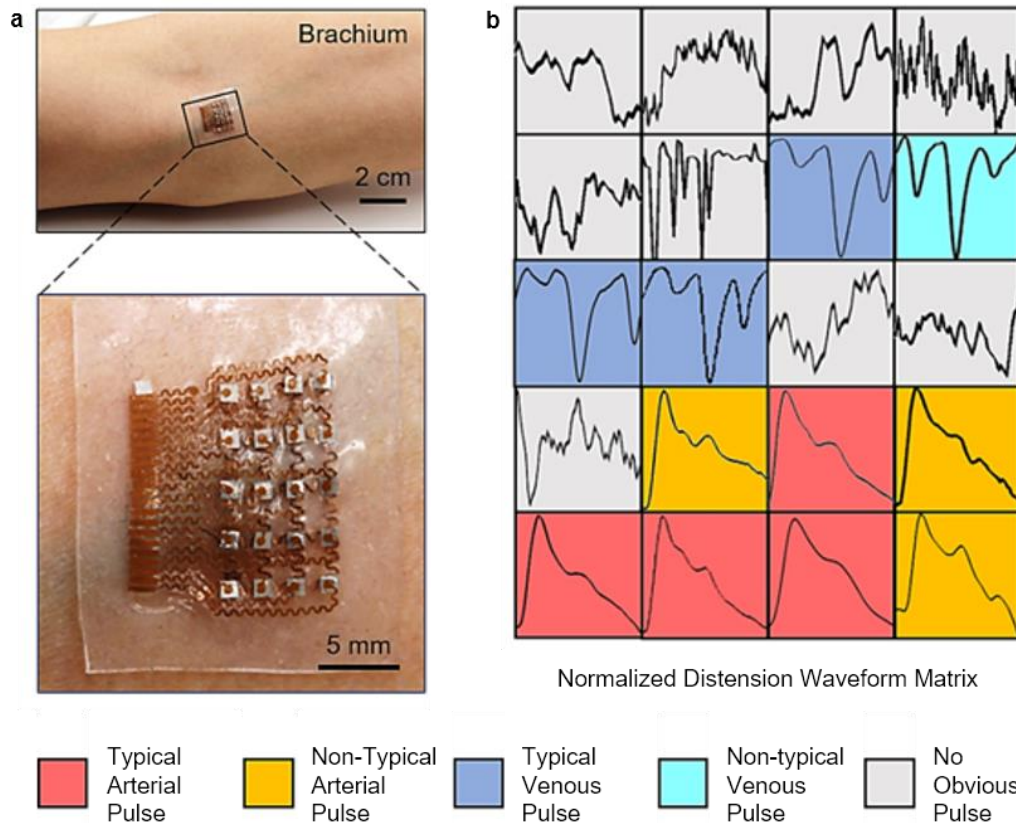
Supplementary Fig. 8. Photographs of the bi-axial tensile test. (a) The 0% original state. **(b)** The state of 30% stretching in x-direction and 25% in y-direction and its recovery. **(c)** The state of 60% stretching in x-direction and 50% in y-direction and its recovery.



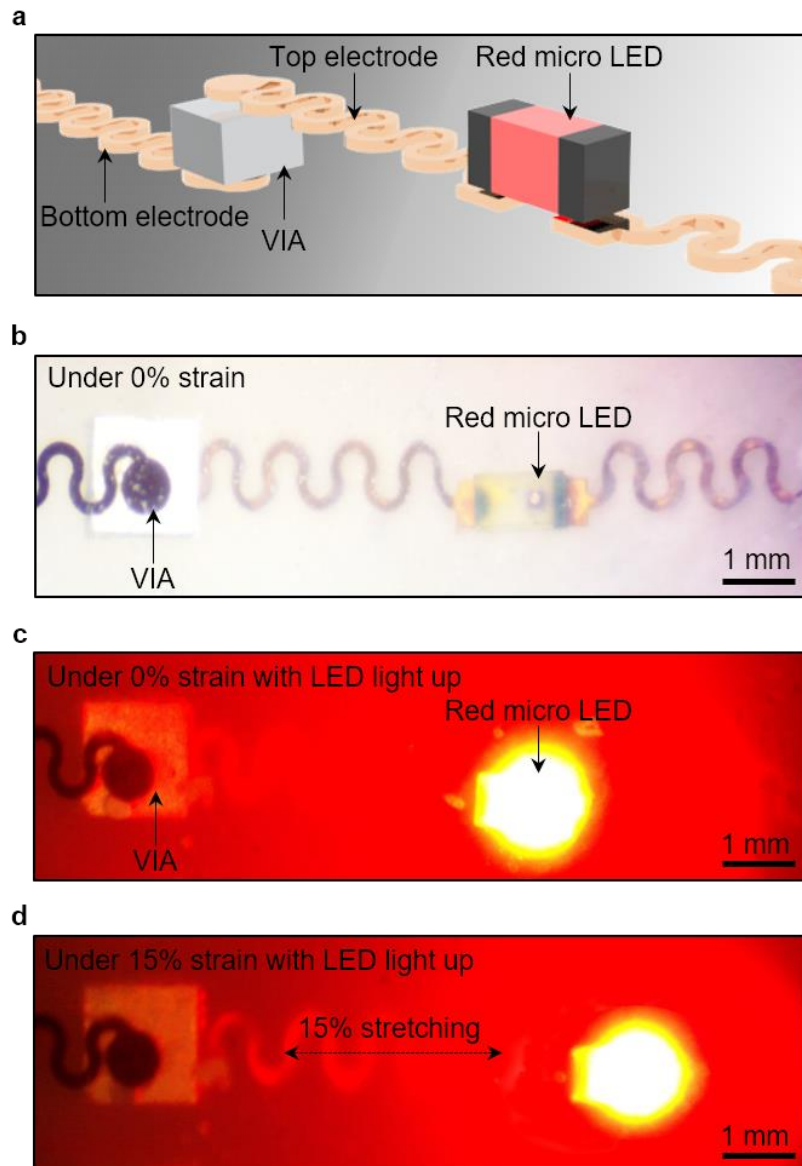
Supplementary Fig. 9. Spatial pulse length of reflected signals. Comparison between 1-3 composites with working frequencies of (a) 3.5 MHz and (b) 7.5 MHz, showing the high frequency has better-defined peaks than the low frequency due to the smaller wavelength of the ultrasound wave.



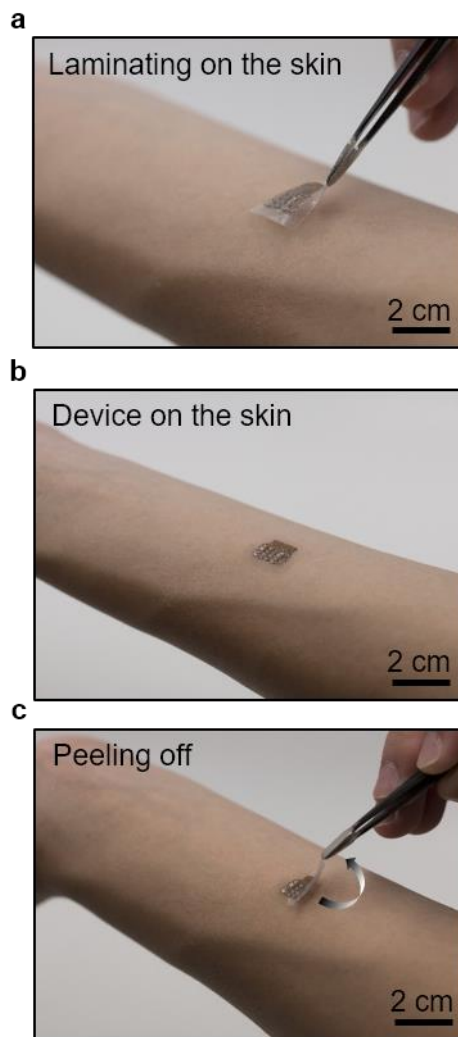
Supplementary Fig. 10. Axial resolution characterization of the stretchable ultrasonic device. (a) The testing setup and representative 1T7R acoustic wave emitting and receiving. (b) The signal of 1T7R. (c) Image reconstruction of the metal wire. The image is shown using the dB scale with 0dB set to be the maximum and -10 dB the minimum grey scale of the image. (d) Axial resolution curve calculated from the reconstructed image, showing the axial resolution can reach down to ~ 0.4 mm.



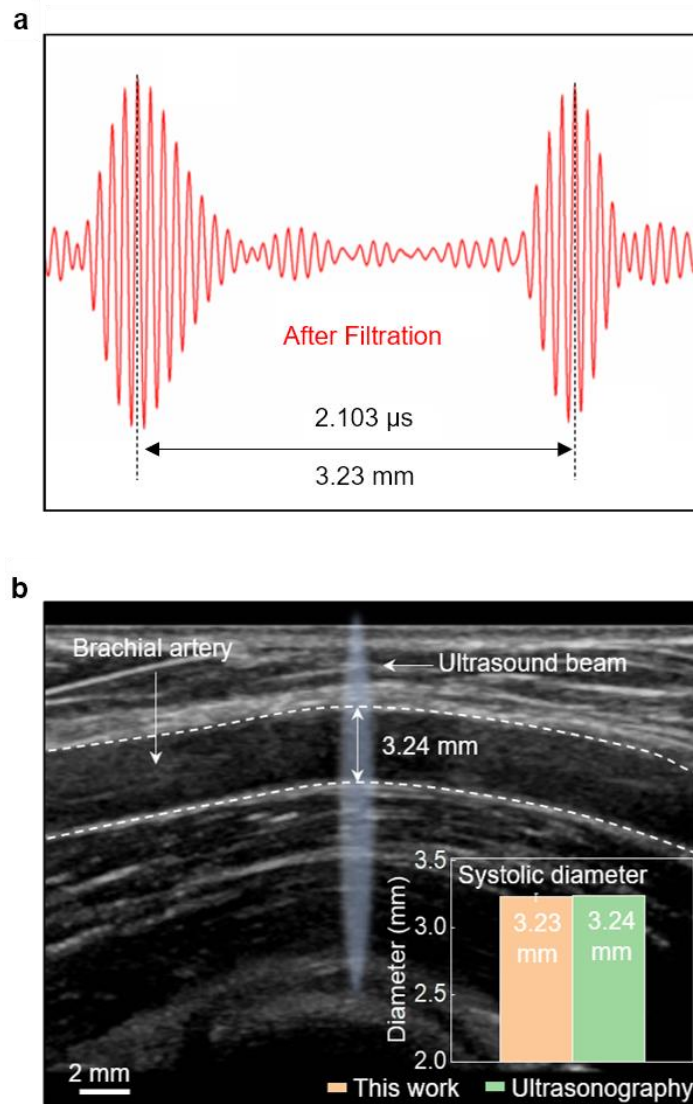
Supplementary Fig. 11. Transducer array and vessel line mapping. (a) The experimental set-up of vessel positioning and recognition. Connections cables for power and data transmission are omitted for clarity purposes. (b) The matrix shows the vessel distention waveforms from all transducer elements individually. The transducer at the optimal position (directly overlying on the vessel) can detect the largest vessel diameter distension. Therefore, the optimal position will be determined by the pixel with the largest pulsatility.



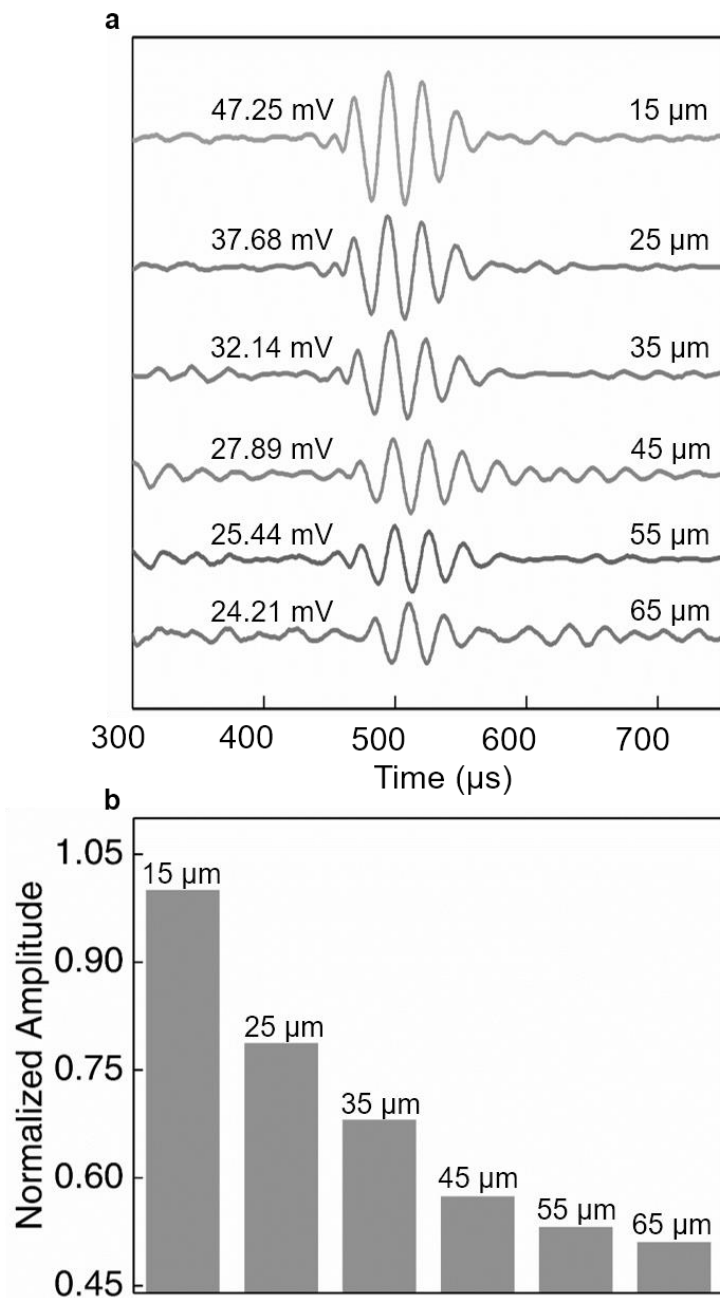
Supplementary Fig. 12. Double-layered electrodes with a vertical interconnect access (VIA) under tensile strain. (a) Circuit structure illustration. Images of the circuit (b) when the LED is off, (c) when the LED is turned on, and (d) when the LED is under 15% tensile strain, showing the mechanical integrity of the system.



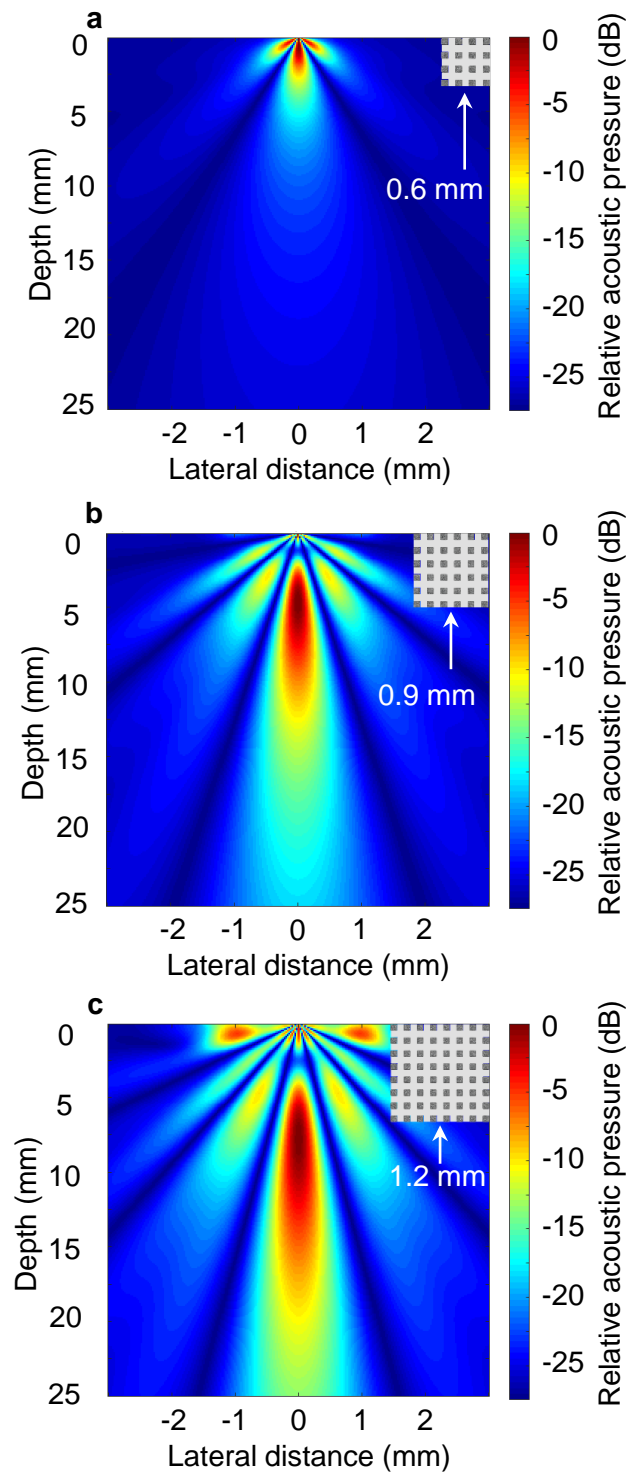
Supplementary Fig. 13. Photographs of the process of using the conformal device. (a) Laminating the device on the skin; (b) The device is on the skin. (c) The device is peeled off from the skin.



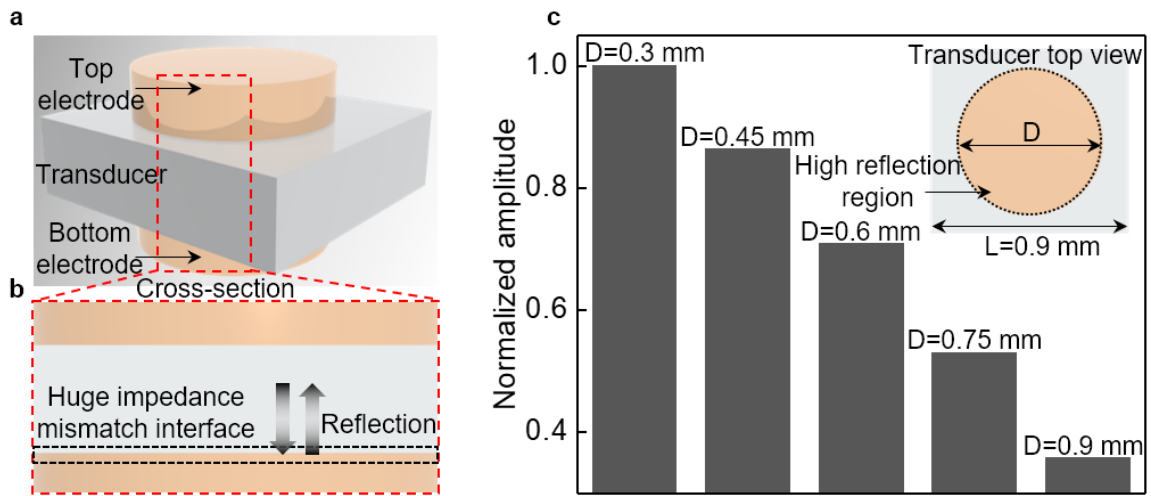
Supplementary Fig. 14. Diameter measurement validation using the commercial ultrasonographic probe. (a) Single transducer measurement on the systolic diameter of the brachial artery (A mode signal). **(b)** Brachial artery systolic diameter measurement by the commercial ultrasonography. The inset figure shows the diameter measurement data by the two methods. The correspondence reaches 99.7%.



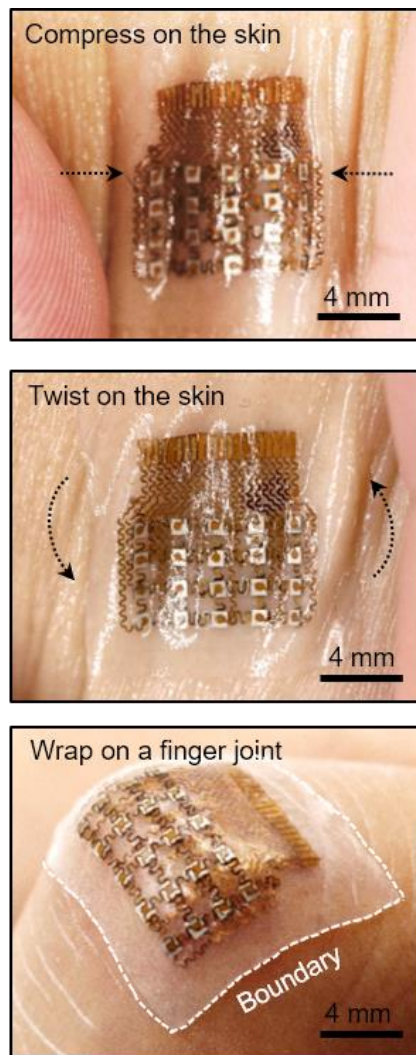
Supplementary Fig. 15. The damping effect of the Ecoflex. (a) Device acoustic emission performance under different thicknesses of the Ecoflex encapsulation at the bottom. **(b)** Normalized peak amplitudes of the transmitted peaks in **a**.



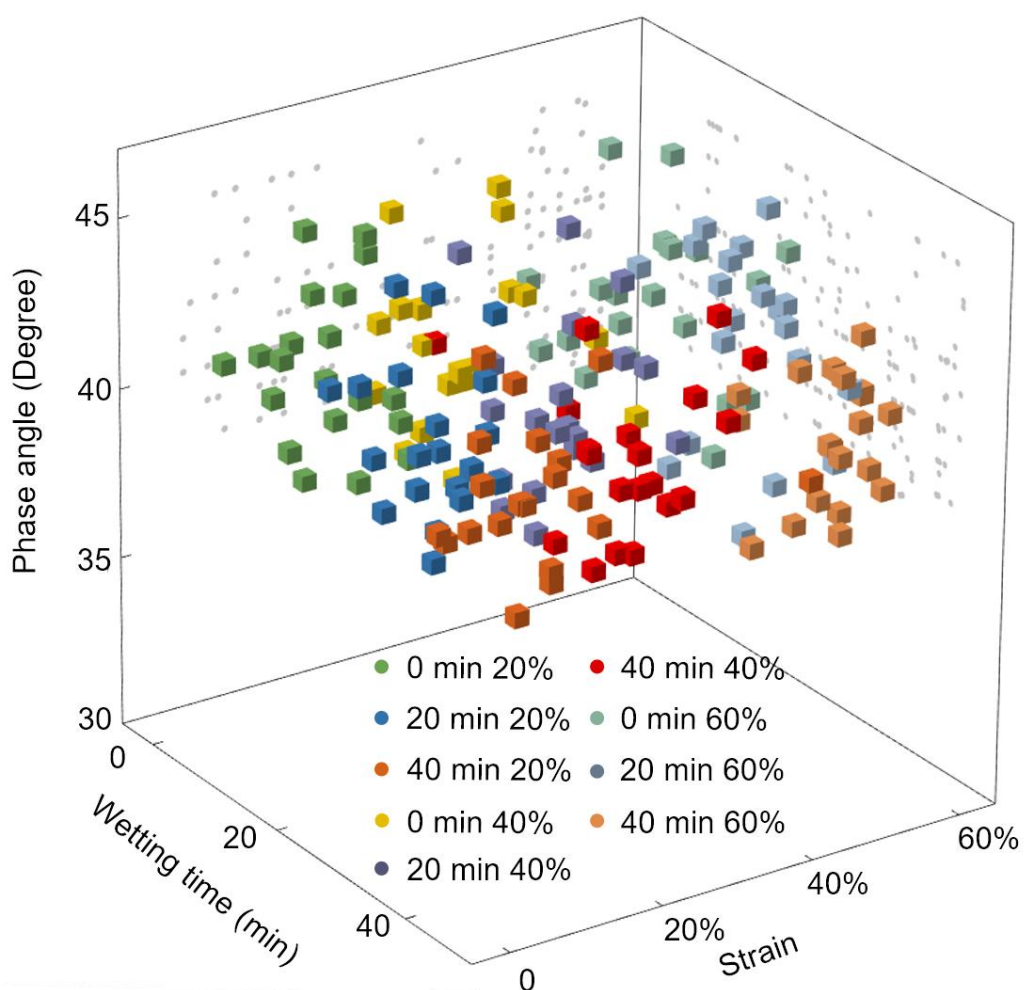
Supplementary Fig. 16. Acoustic field simulation for 1-3 piezoelectric composites with different sizes: (a) $0.6\text{ mm} \times 0.6\text{ mm}^2$, (b) $0.9\text{ mm} \times 0.9\text{ mm}^2$, and (c) $1.2\text{ mm} \times 1.2\text{ mm}^2$, respectively. All images are shown using the dB scale with 0 dB set to be the maximum and -25 dB the minimum.



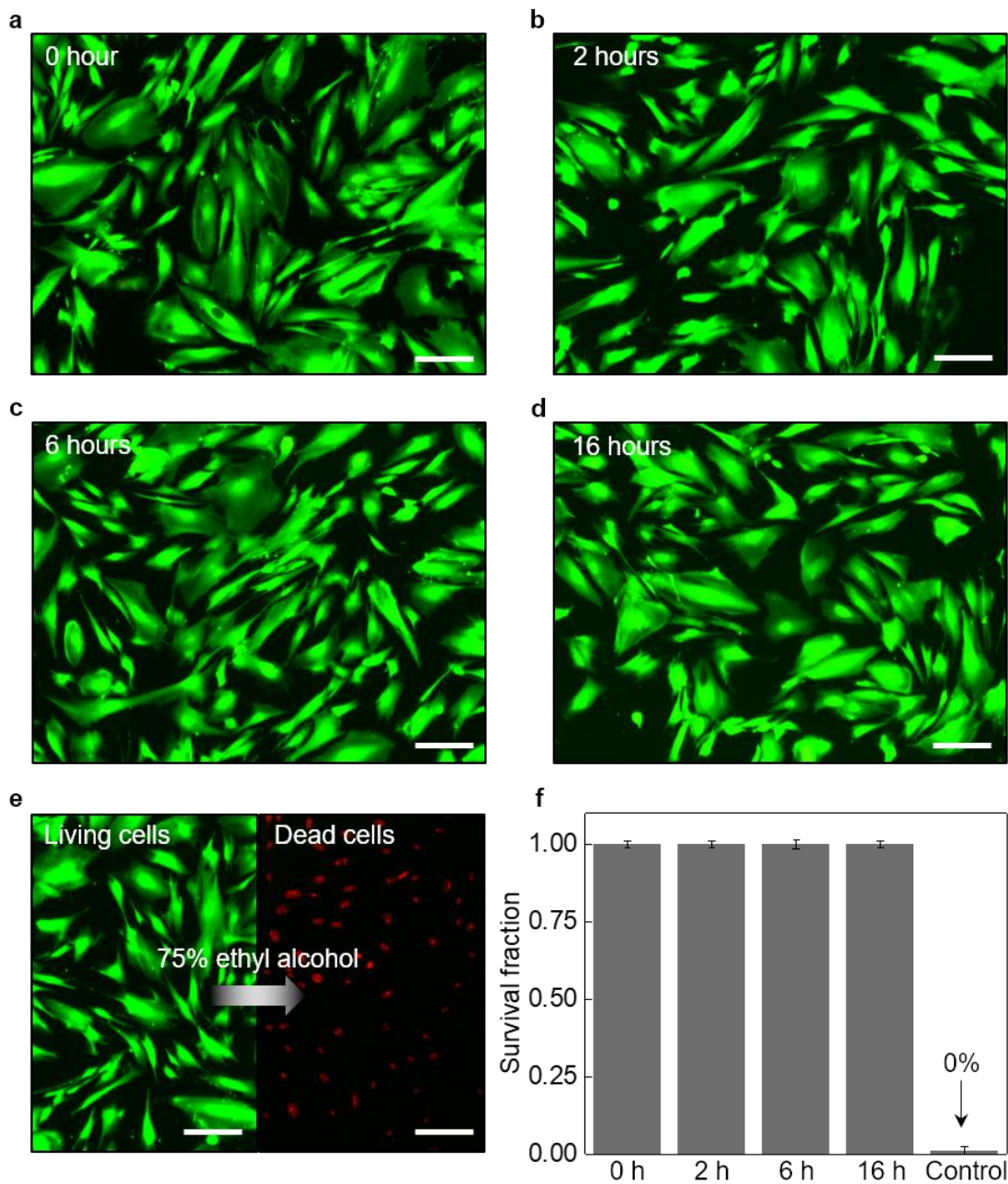
Supplementary Fig. 17. Acoustic emission performance comparison of devices with different diameters of the circular bottom electrode. The results show different portions of ultrasonic energy reflected by the bottom electrode with different sizes. (a) The layered structure of the device. (b) The cross-sectional view of the device, showing the interfacial reflection caused by impedance mismatch between the Cu electrode and the 1-3 composite. (c) The experimental results of acoustic emission performance of the device with different bottom electrode diameters. The signal amplitudes are normalized.



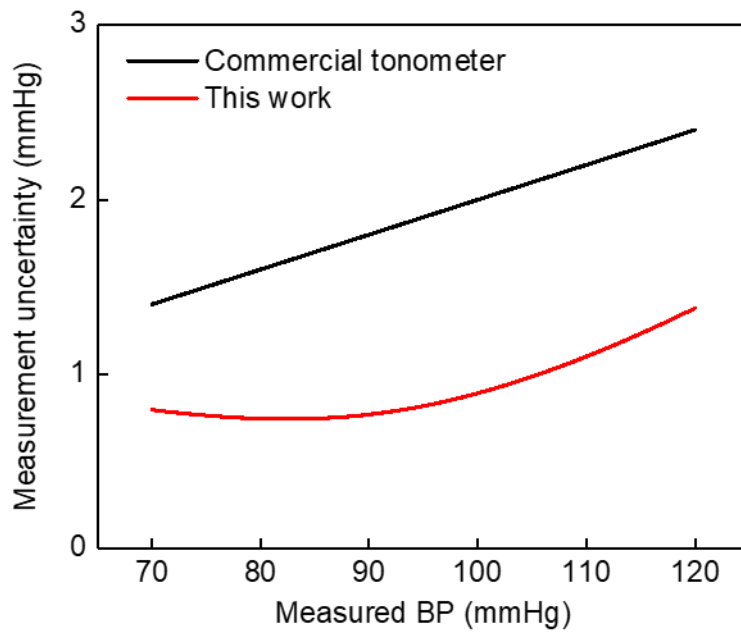
Supplementary Fig. 18. Photographs of the device integrated on the skin, demonstrating its outstanding mechanical compliance. The device has similar mechanical properties to the skin and can thus adapt to the natural motion of the skin.



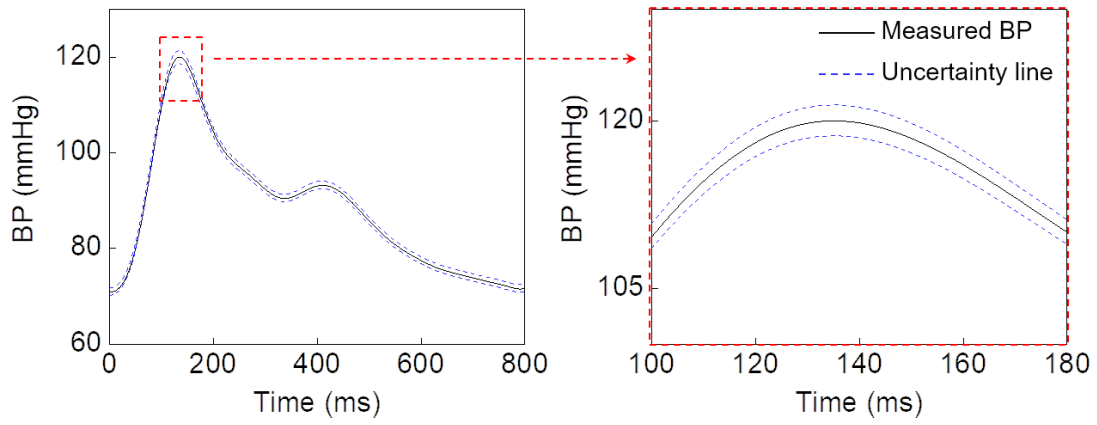
Supplementary Fig. 19. Electrical performance of the device under various levels of tensile strain and moisture conditions at room temperature. The strain levels are 0%, 20%, 40%, and 60%. The device is dipped in water for 0, 20, and 40 min under those four tensile strain levels. After that, the phase angles of 20 transducers are measured under each condition. The results show the stable electric performance of the device under these conditions.



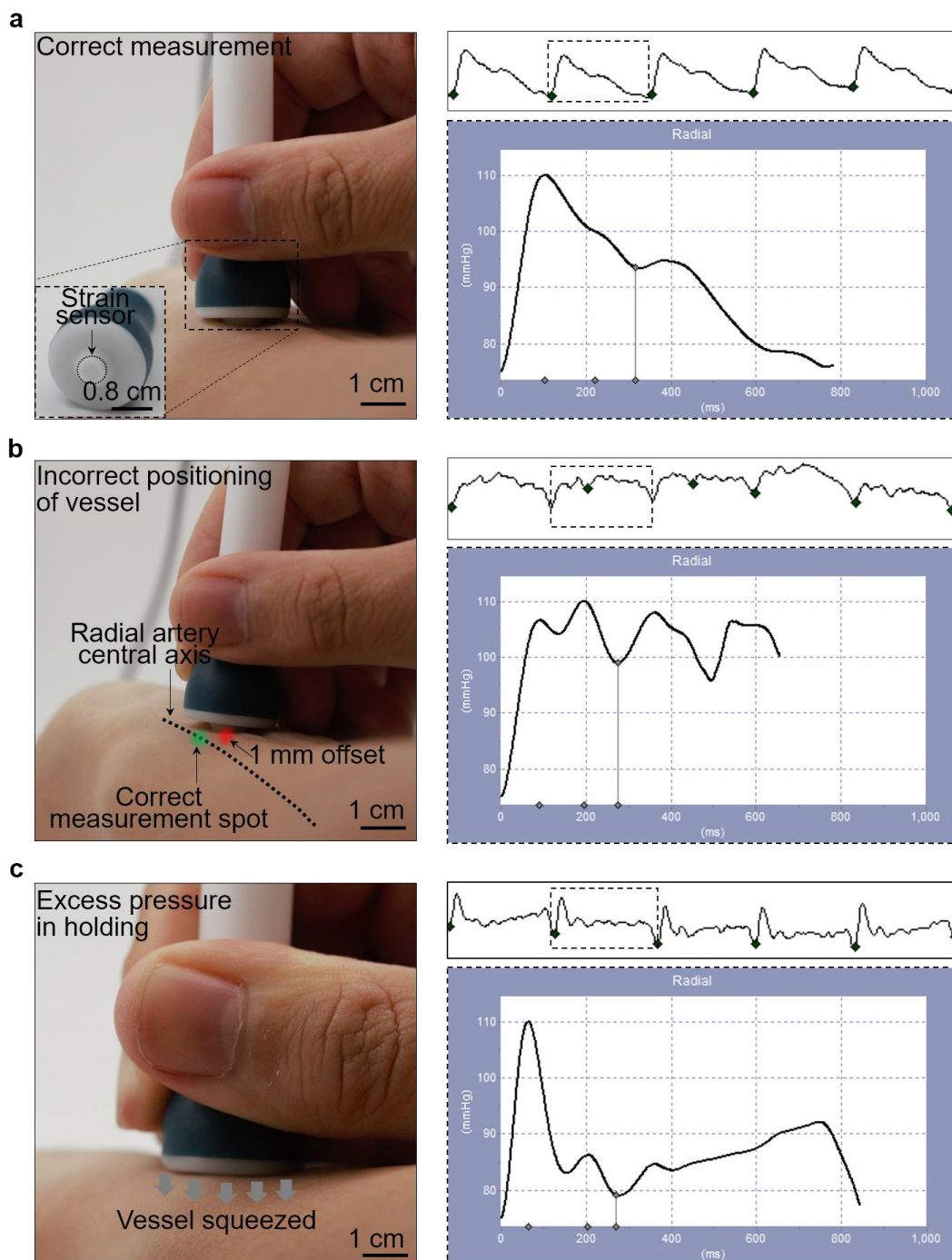
Supplementary Fig. 20. Cell viability assay. Fluorescent images of HFF-1 cells cultured under exposure of the stretchable ultrasound device. Images of (a) healthy HFF-1 cells, and (b)-(d) HFF-1 cells under a continuous ultrasound exposure for 2 hours, 6 hours, and 16 hours, respectively, showing good cell viability and survival under the acoustic pressure of the device. (e) Positive control experiment demonstrated the robustness of the testing and observing method. (f) The statistics of the survival fraction of HFF-1 cells. The results are averaged from five different observations. Scale bars are all 20 μm .



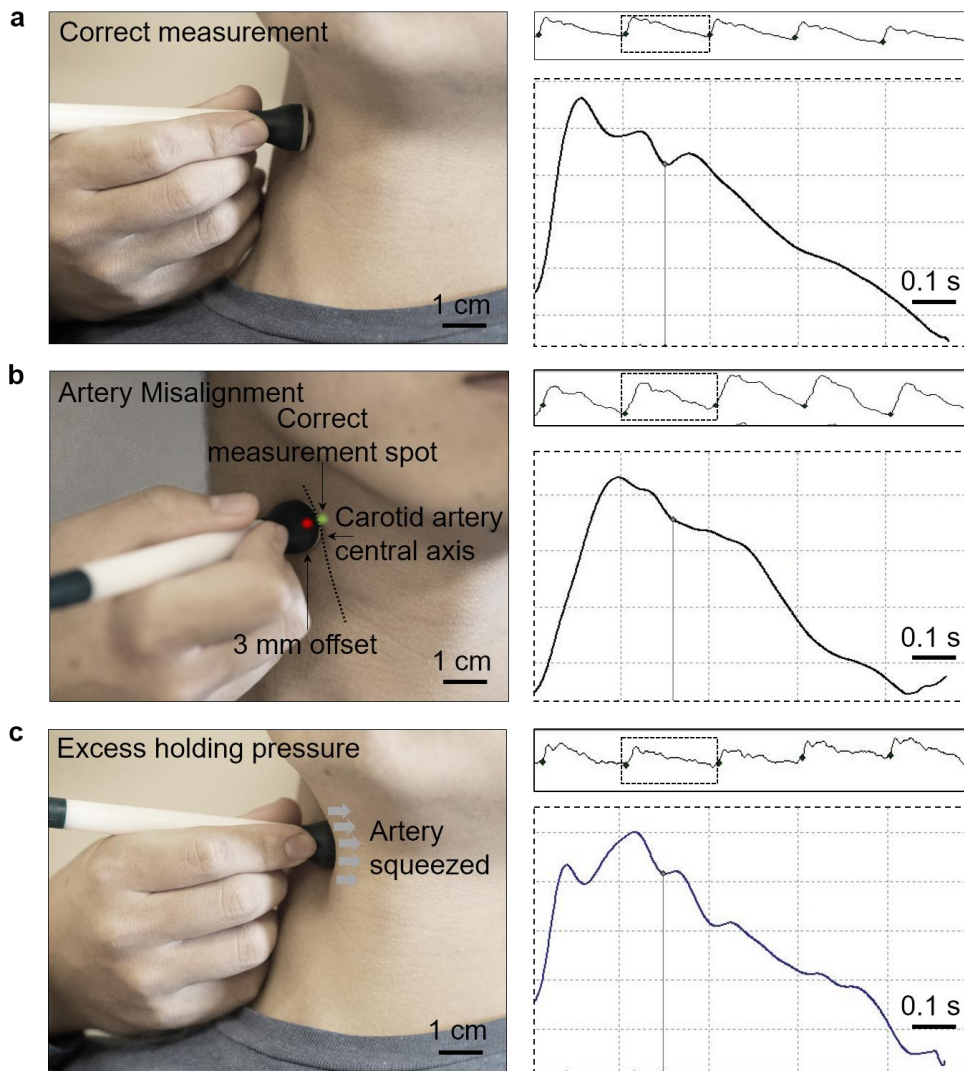
Supplementary Fig. 21. Comparison of the measurement uncertainty between the commercial tonometer (SphygmoCor EM3[®]) and our ultrasonic device. The results show that our device has a lower measurement uncertainty than the commercial gold standard in common ranges of BP.



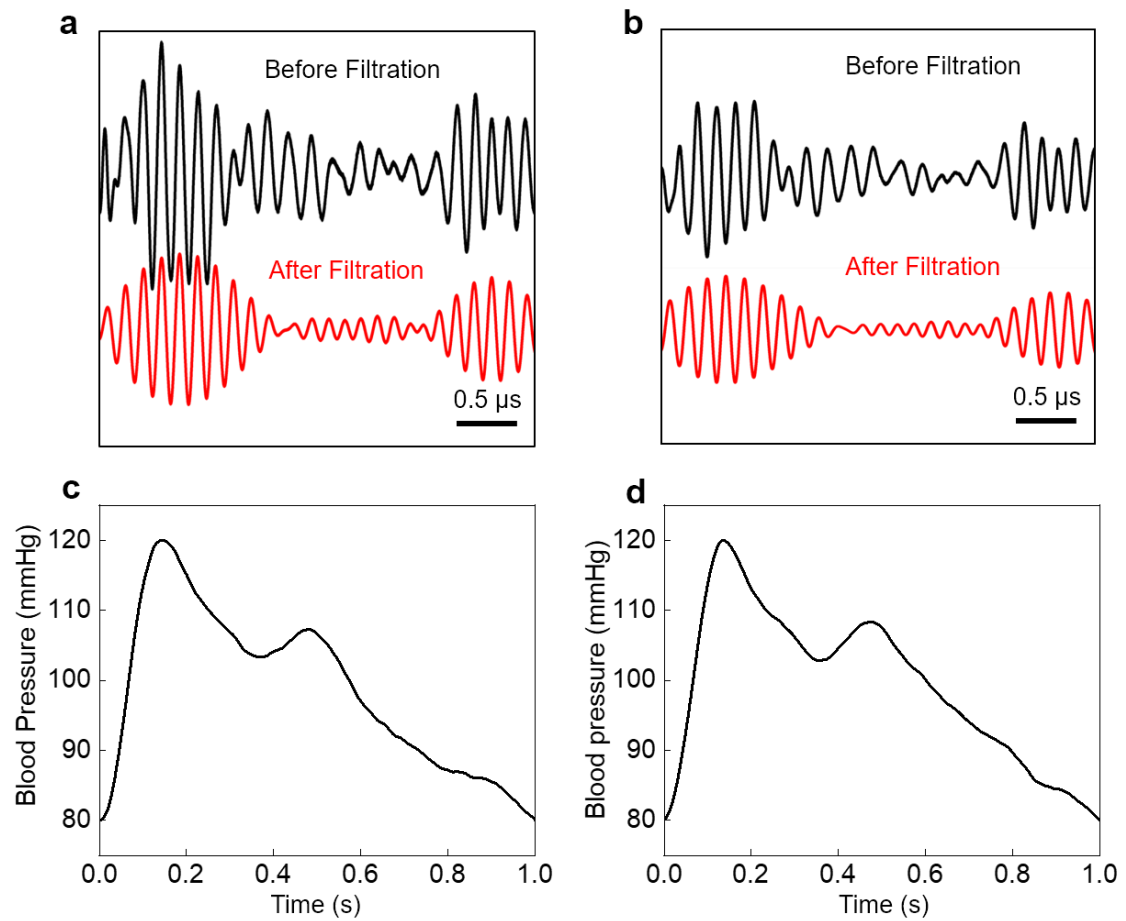
Supplementary Fig. 22. The measured BP waveform using our device and its uncertainty range. The blue dashed line shows the uncertainty range. The small uncertainty range ensures the reliability of our measurement results.



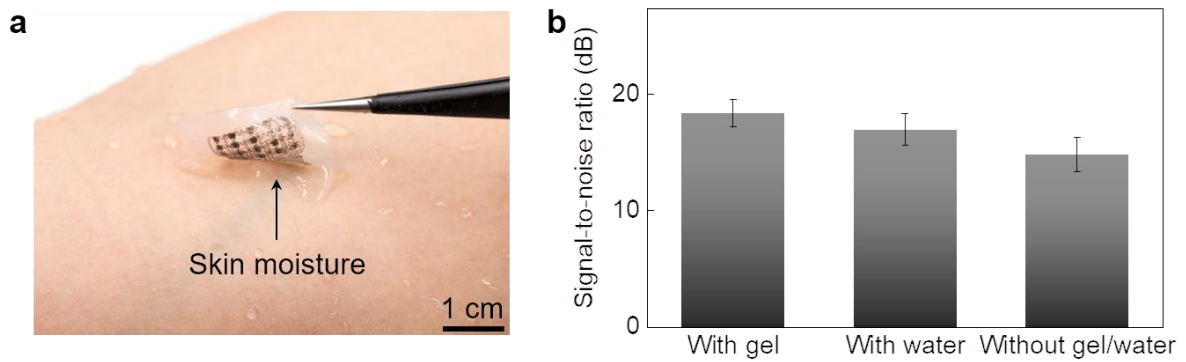
Supplementary Fig. 23. Operator dependency of the commercial applanation tonometry system (SphygmoCor EM3®) measuring the radial artery (peripheral). (a) Correct measurement condition and the corresponding waveform. **(b)** Incorrect vessel positioning and the erroneous recording. **(c)** Moderately excessive holding pressure induces squeezing the vessel that leads to waveform morphology distortion.



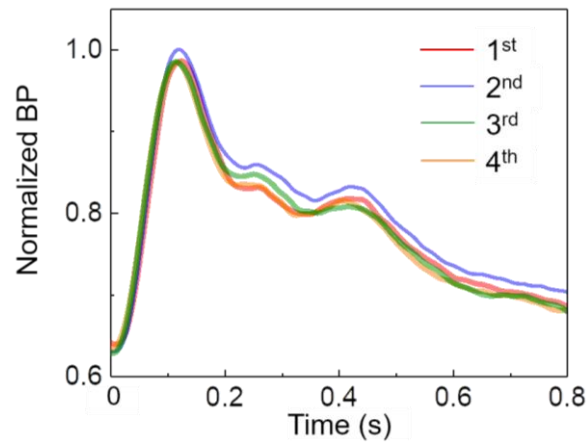
Supplementary Fig. 24. Operator dependency of the gold standard applanation tonometry system (SphygmoCor EM3®) measuring the carotid artery (central). (a) Correct measurement condition and the corresponding waveform. **(b)** Vessel misalignment and the erroneous recording. **(c)** Moderately excessive holding pressure induces squeezing the vessel that leads to significant waveform distortion.



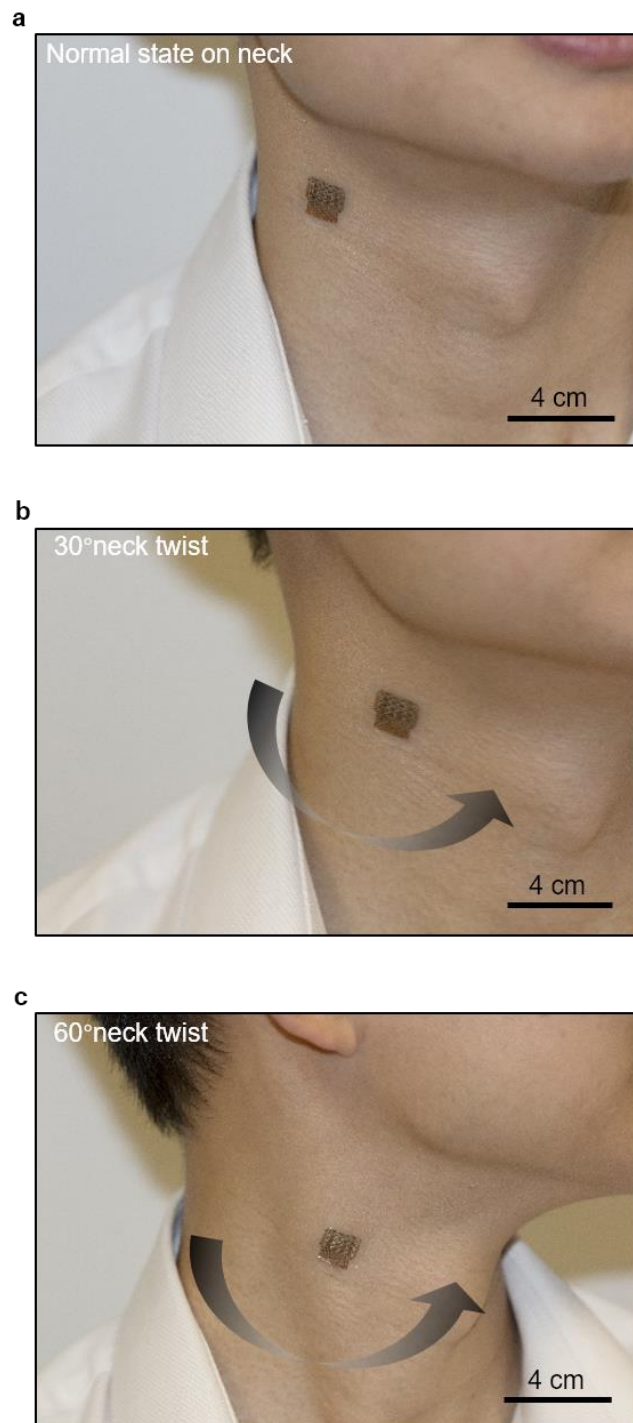
Supplementary Fig. 25. Comparison of the device acoustic emission performance with and without the ultrasonic gel. Echoes received (a) with and (b) without the ultrasonic gel. Measured waveforms from the radial artery after decoding (c) with and (d) without the ultrasonic gel. The results show comparable signal quality.



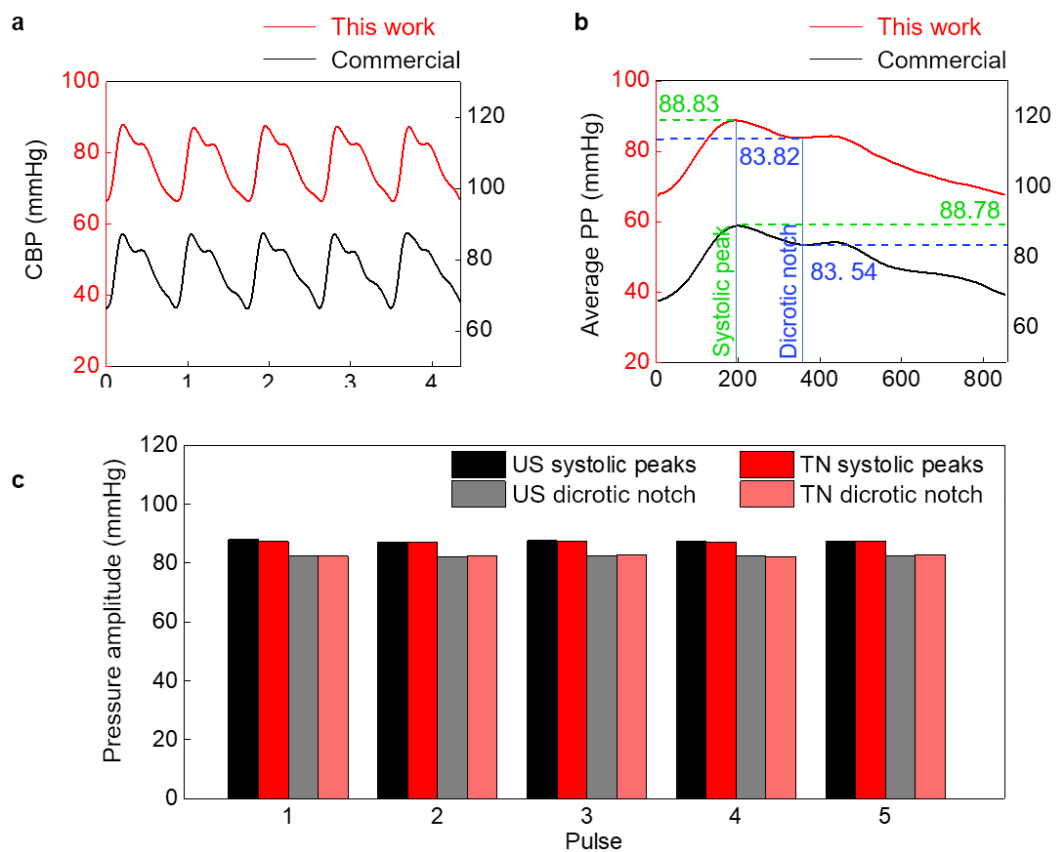
Supplementary Fig. 26. Signal qualities of the conformal ultrasound device with different coupling agents. (a) The testing condition image. (b) Signal quality comparison when ultrasonic gel, water, and no gel or water are applied as the acoustic coupling agent. The results show that neither skin moisture nor absence of gel or water will degrade the signal quality of the device.



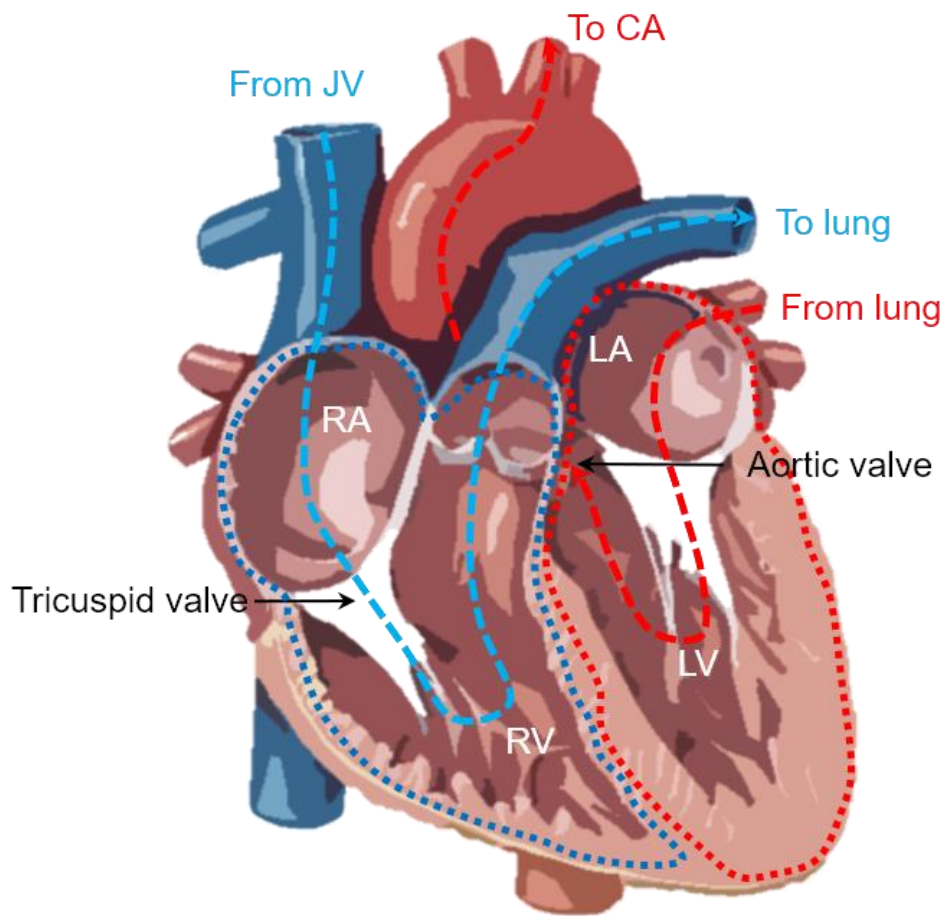
Supplementary Fig. 27. Reusability test of the device. The measurements are carried out on the same subject under the same condition during 1st (the first week), 2nd (the second week), 3rd (the third week), and 4th (the fourth week). The four measurements are normalized to the same diastolic and systolic pressure values for clarity purposes.



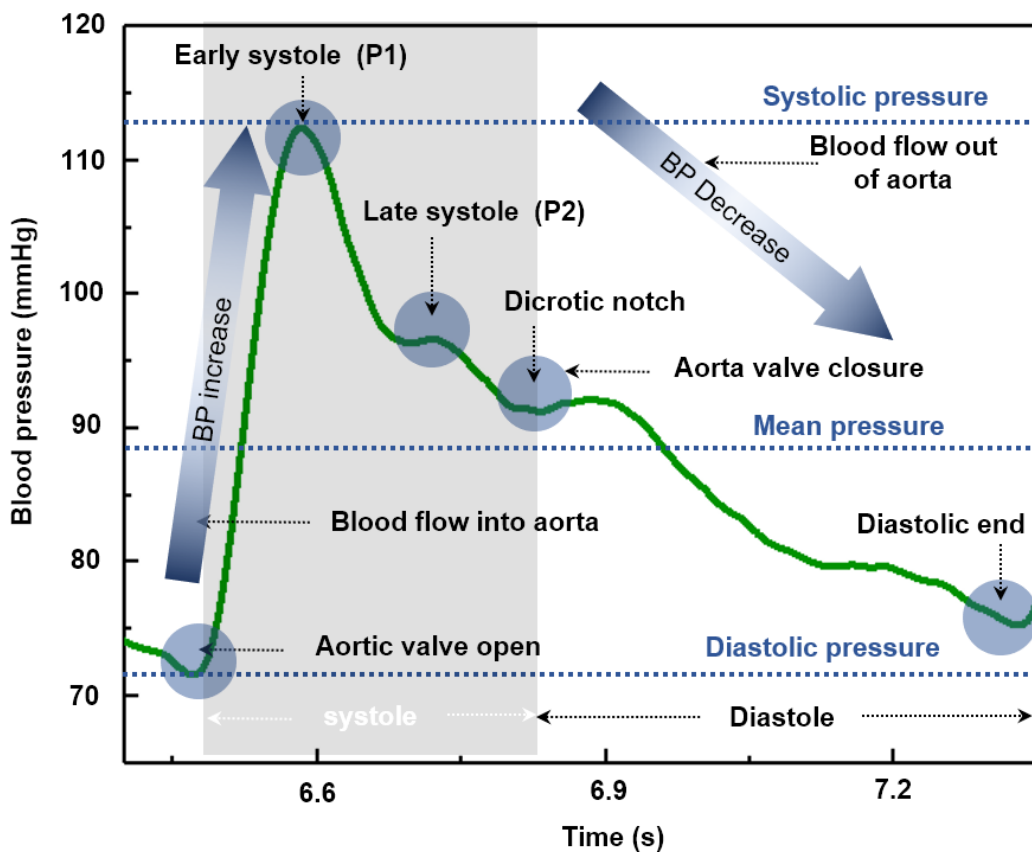
Supplementary Fig. 28. Conformability and self-adhesion of the device on the neck under different postures: (a) Normal state; (b) with 30° neck twist; (c) with 60° neck twist.



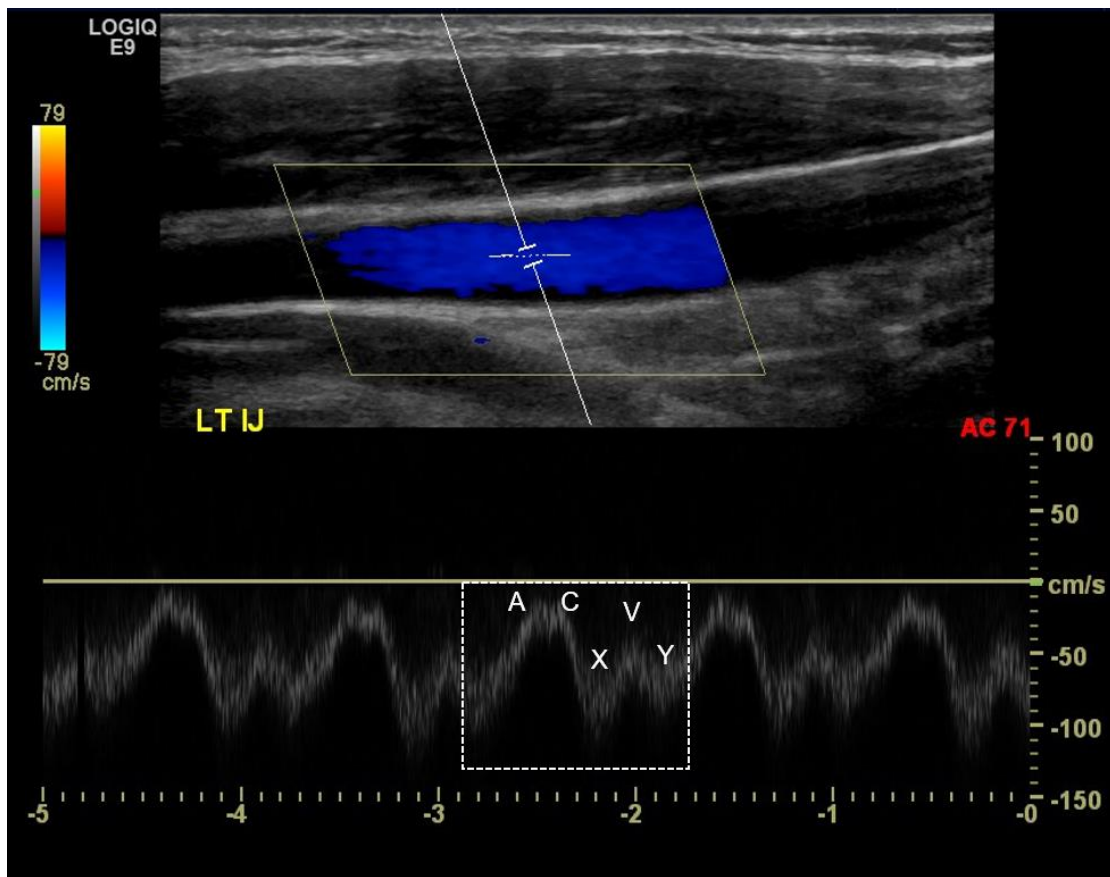
Supplementary Fig. 29. CBP measurement results and their validation. (a) Continuous CBP waveforms measured by our device and the commercial tonometer. (b) Averaged wave pulse pressure (PP) values extracted from 10 continuous pulse waveforms. The systolic pressure (SP) and dicrotic notch (DN) is compared. The difference of the SPs is 0.05 mmHg, and the difference of the DNs is 0.28 mmHg. (c) The comparison of systolic peaks and dicrotic notches between the ultrasound (US) method and tonometry (TN) method. The CBP waveform provided by the commercial tonometer is calibrated by brachial pressure and arterial stiffness measured by ECG correlation.



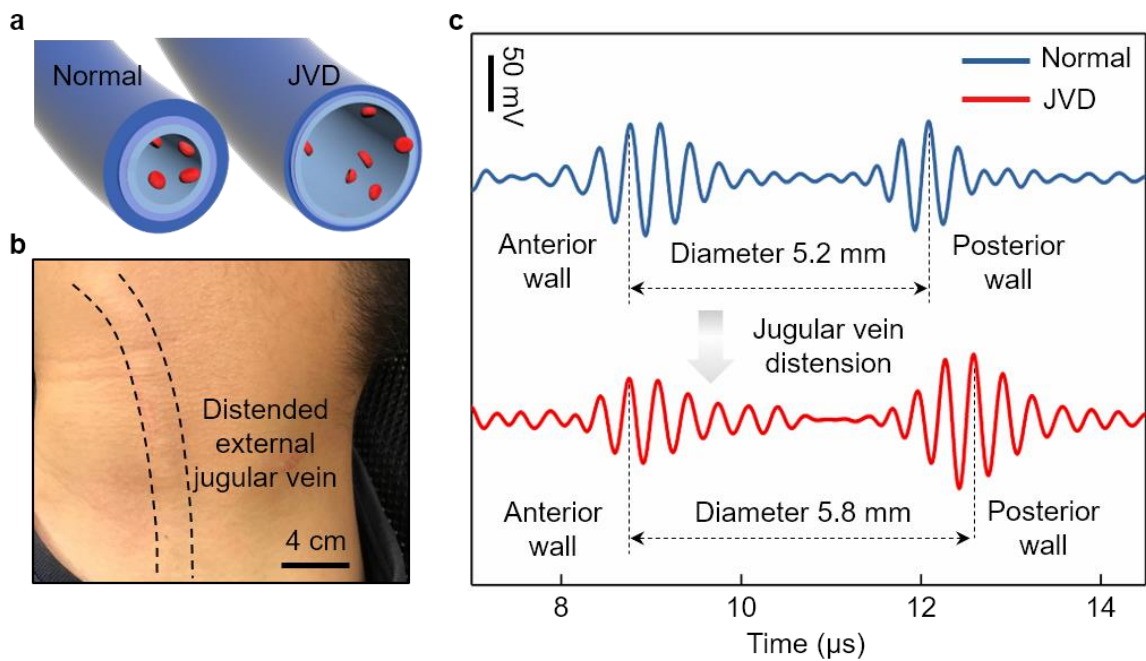
Supplementary Fig. 30. The anatomical structure of the human heart and associated blood flow sequence. (JV = jugular vein, CA = carotid artery, RA = right atrium, LA = left atrium, RV = right ventricle, and LV = left ventricle).



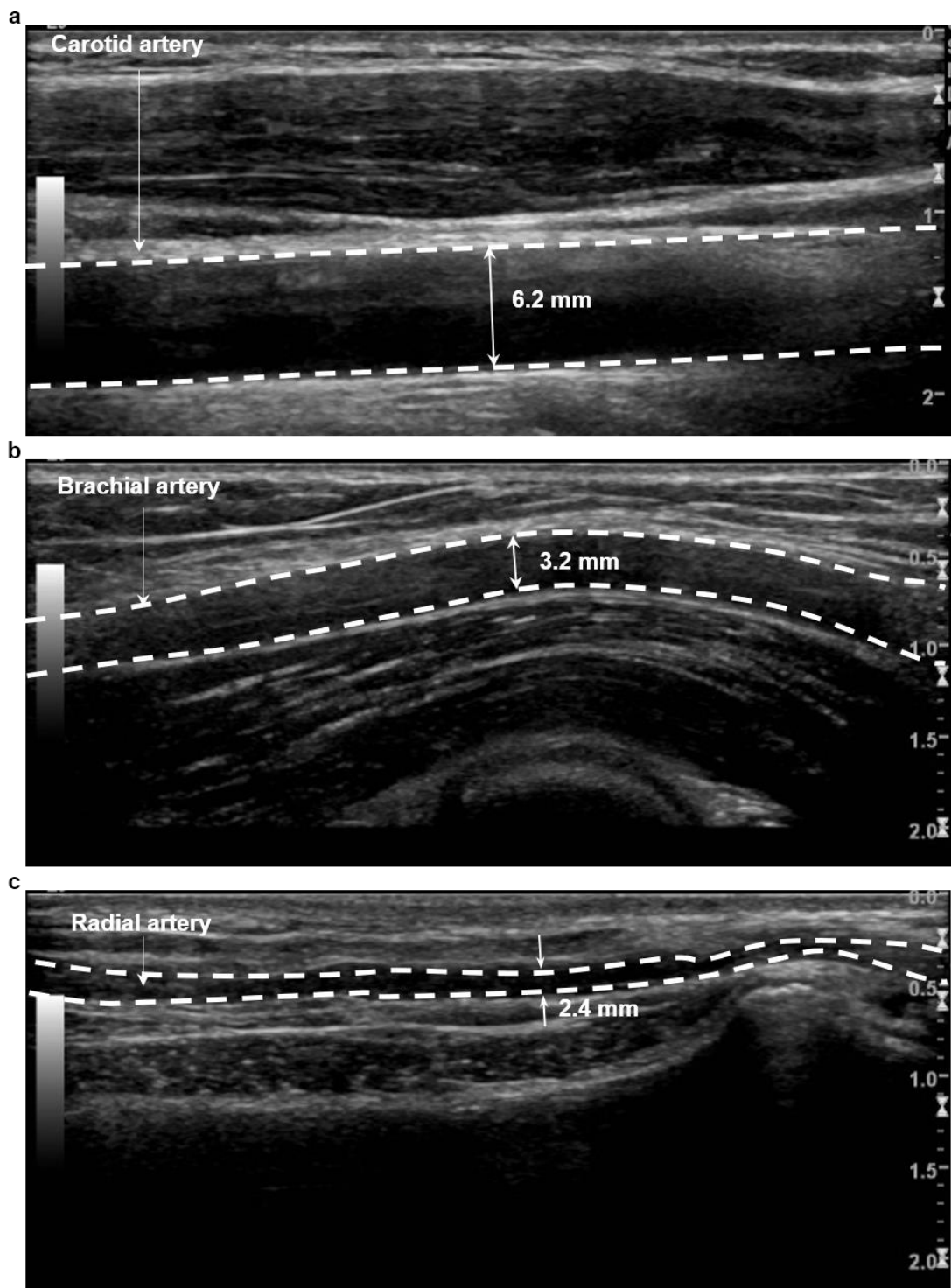
Supplementary Fig. 31. BP waveform illustration. Three major components are labeled as the systolic phase, dicrotic notch, and diastolic phase. Other waveform morphologies with corresponding physiological meaning are also labeled.



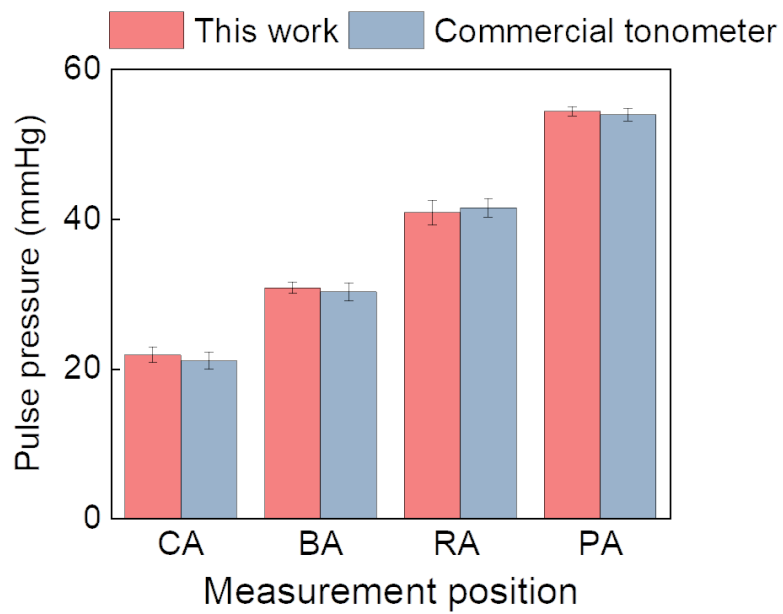
Supplementary Fig. 32. A Doppler ultrasound image of an internal jugular vein and its associated Doppler waveform. Corresponding A, C, X peaks and V, Y descents are labeled in one cycle of the jugular venous waveform.



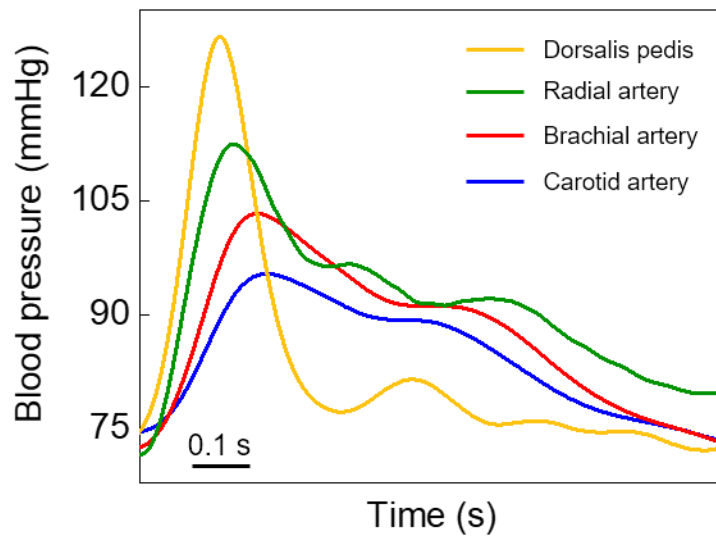
Supplementary Fig. 33. JVD monitoring by the conformal ultrasound device. (a) The schematics for external JVD caused by dramatic increases in the thoracic pressure. (b) A photograph of the human neck with a JVD created by deep exhalation. (c) Vessel wall measurements before and after JVD, showing evident diameter distension after deep exhalation.



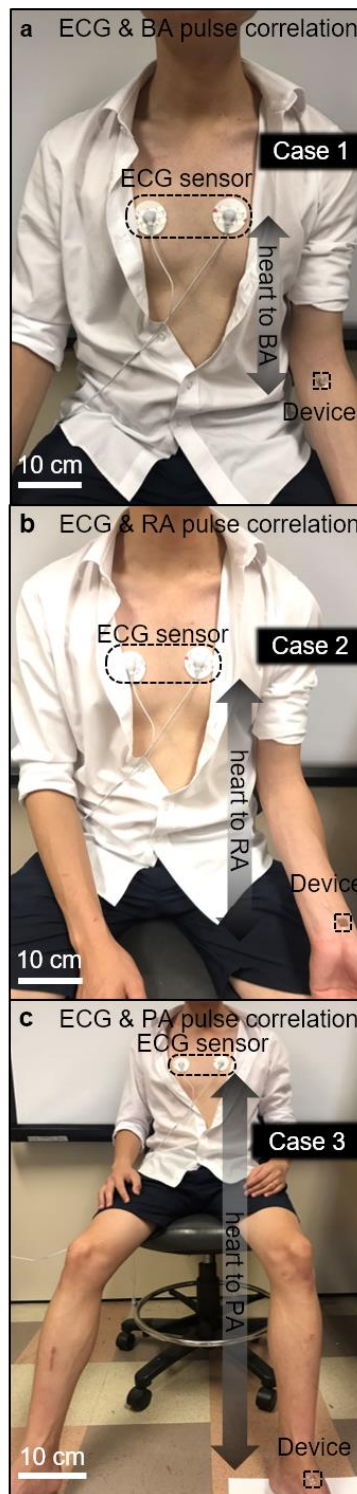
Supplementary Fig. 34. Grayscale images of blood vessels from central to peripheral measured by Doppler ultrasound. The results show the gradual shrinkage of the vessel diameter. (a) The carotid artery with the diameter of 6.2 mm, (b) the brachial artery with the diameter of 3.2 mm, and (c) the radial artery with the diameter of 2.4 mm. Those shrinkage of the vessel will introduce progressive increase of the vascular resistance (related equation appears in Supplementary note 9).



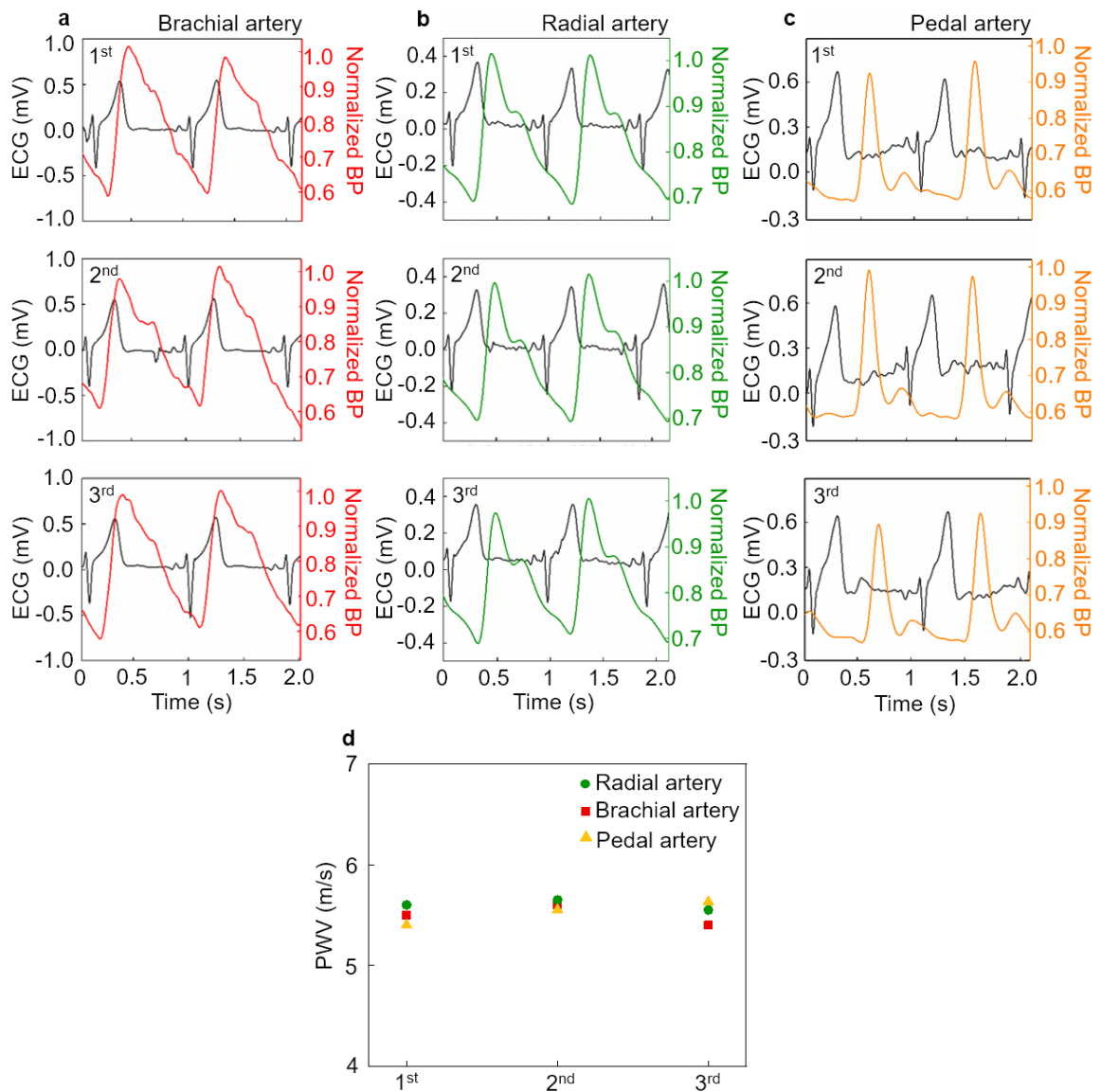
Supplementary Fig. 35. Measurement validation using a commercial equipment of pulse pressure amplification from the central artery (CA) to the peripheral arteries (BA, RA, and PA). The validation results show a high correspondence of our conformal device to the commercial equipment.



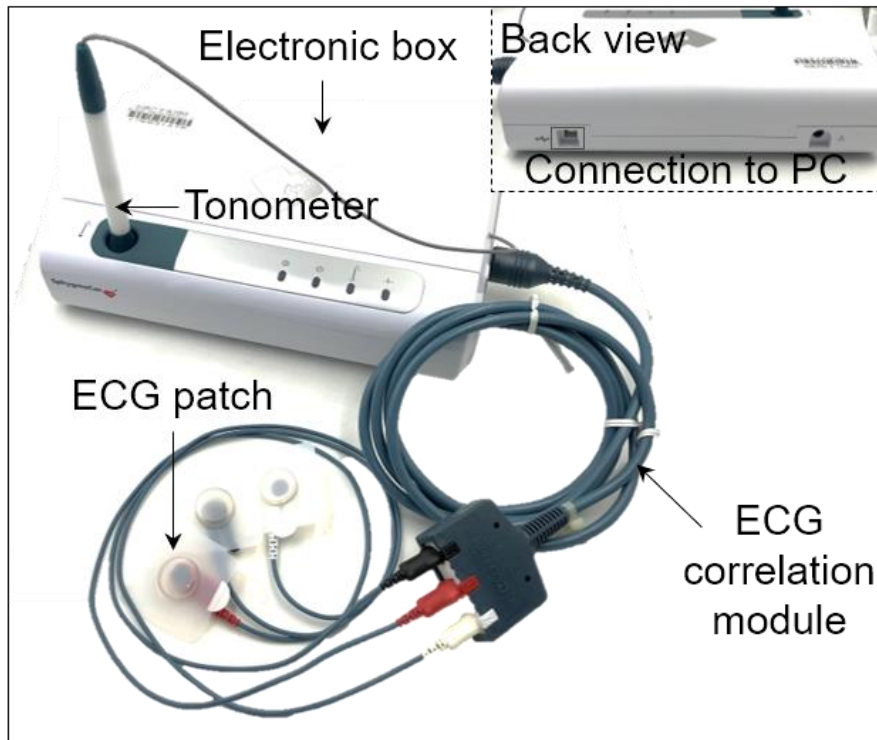
Supplementary Fig. 36. Comparison of the upstroke gradient from the central to peripheral arteries. The data show the systolic upstroke gets steeper as the artery goes away from the heart, due to the progressive arterial stiffness and reflection.



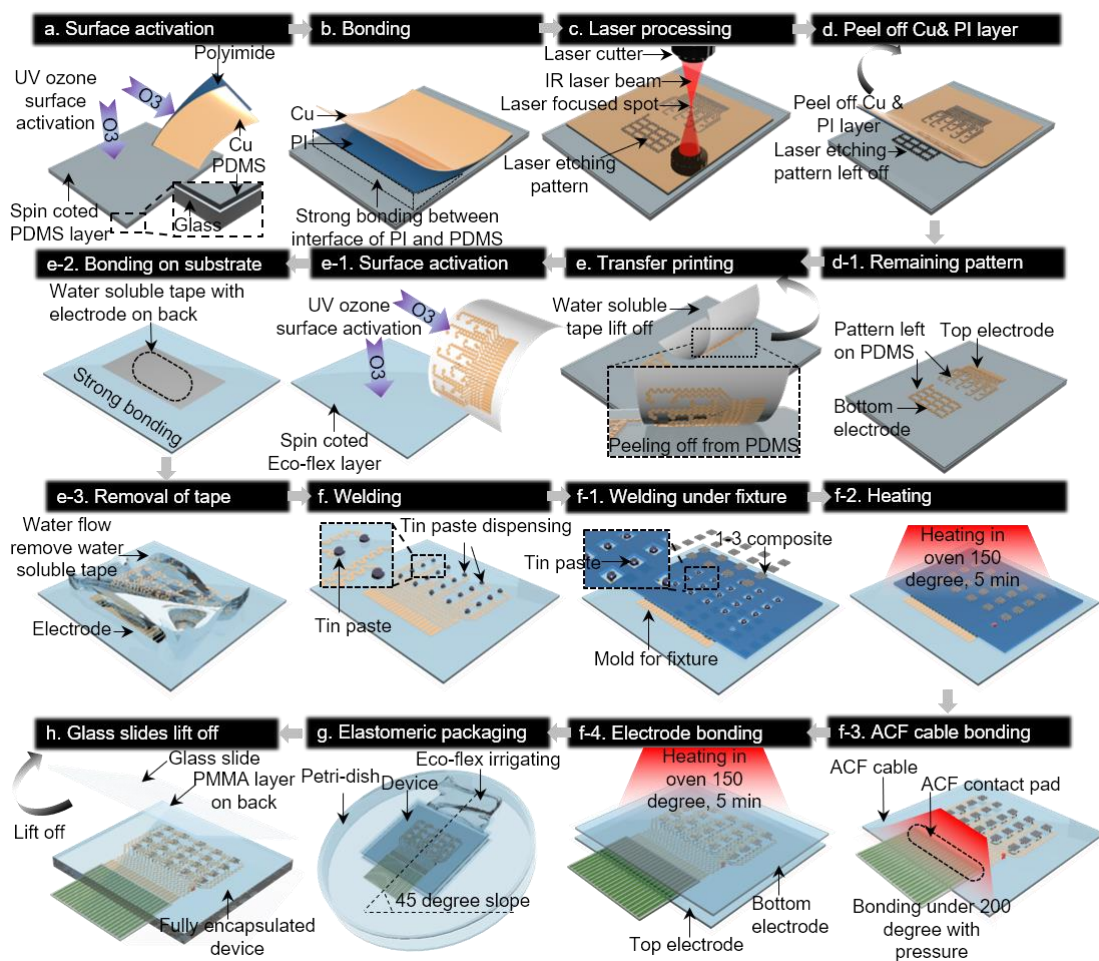
Supplementary Fig. 37. Testing conditions for ECG correlation. Correlations to (a) brachial artery, (b) radial artery, and (c) pedal artery. In each case, PAT will be measured to calculate the associated PWV.



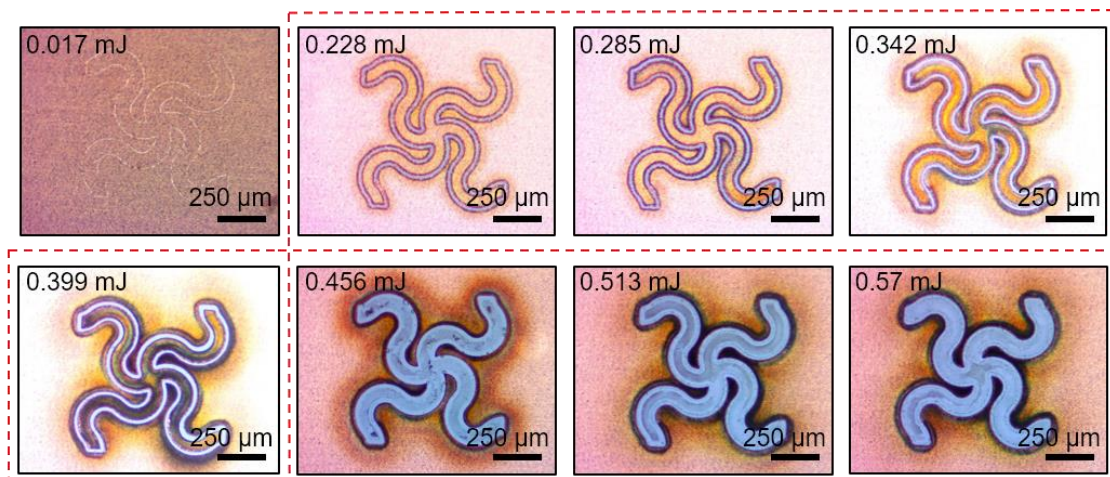
Supplementary Fig. 38. Testing robustness of the ECG correlation. Three measurements on the same subject with the same and stable physiological status on (a) brachial, (b) radial, and (c) pedal arteries, respectively, showing consistent results of the PWV. The pressure waveforms are normalized. (d) Statistics of the PWV in these measurements.



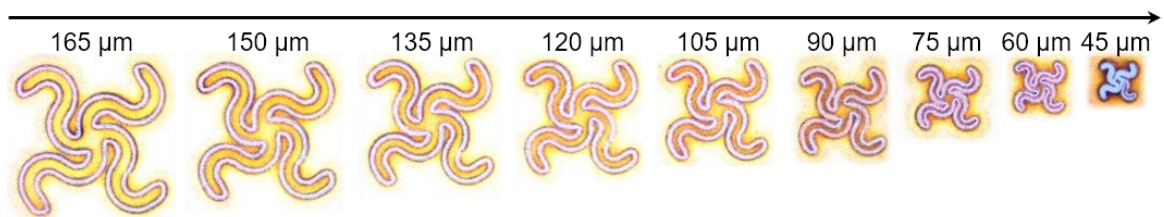
Supplementary Fig. 39. The commercial CBP monitoring tonometer: SphygmoCor EM3[®] (AtCor Medical, Sydney, Australia) with ECG patches for PWV measurements. Each key component is labeled.



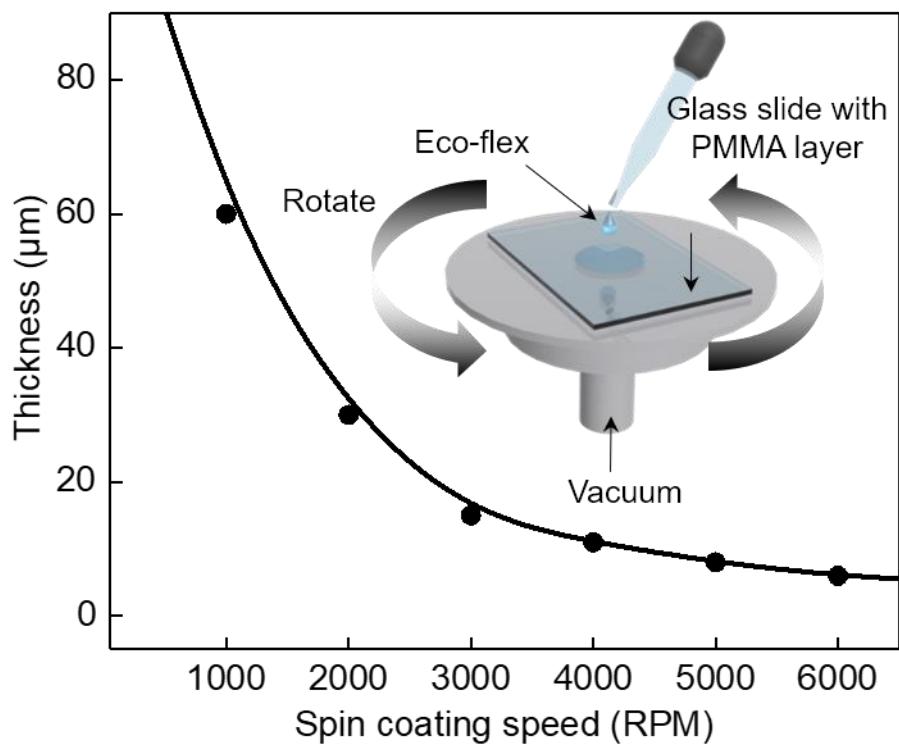
Supplementary Fig. 40. Stretchable ultrasound device fabrication flow chart. (a) Surface activation to enhance the interfacial bonding between the Cu/PI and the PDMS layers. (b) The PI side has strong bonding with the PDMS after UV ozone activation. (c) Circuit fabrication based on laser ablation. (d) Cu/PI layer lift-off. (e) Transfer printing using the water-soluble tape. (f) Welding the transducers to the ACF cable. (g) Elastomeric encapsulation using Ecoflex. (h) Glass slides removal.



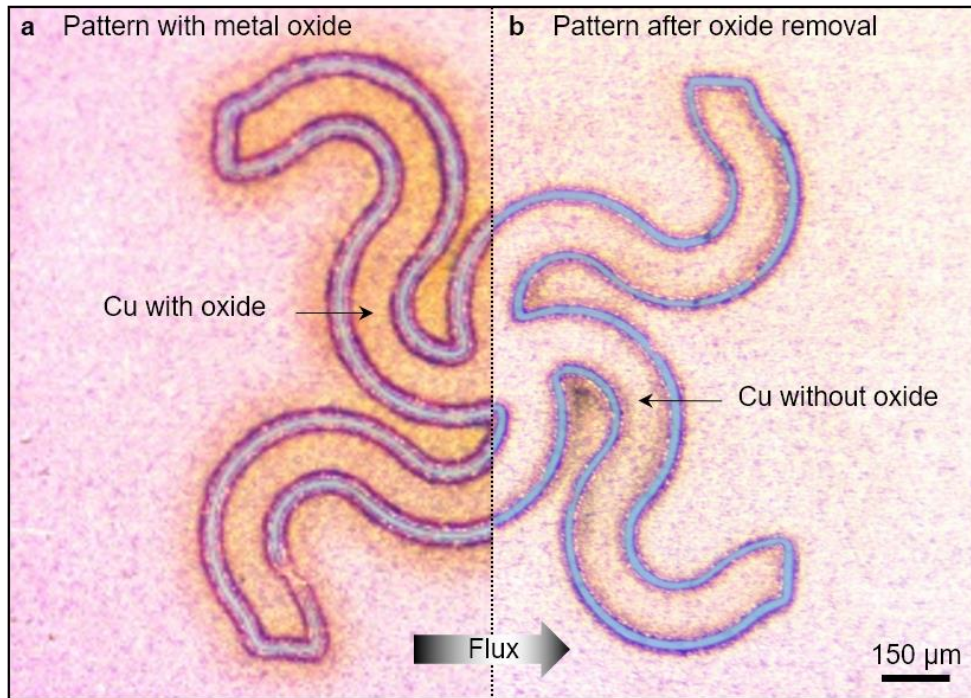
Supplementary Fig. 41. Photographs of Cu patterns processed under different levels of laser power. When the laser power is low (e.g., below 0.228 mJ), Cu won't be etched through. When the laser power is high (e.g., above 0.339 mJ), the thin Cu interconnects are ablated away. Therefore, an ideal range of laser power is 0.228 mJ~0.339 mJ. The other parameters including pulse repetitive frequency: 900 KHz, speed: 300 mm/s, and pulse width: 241 ns.



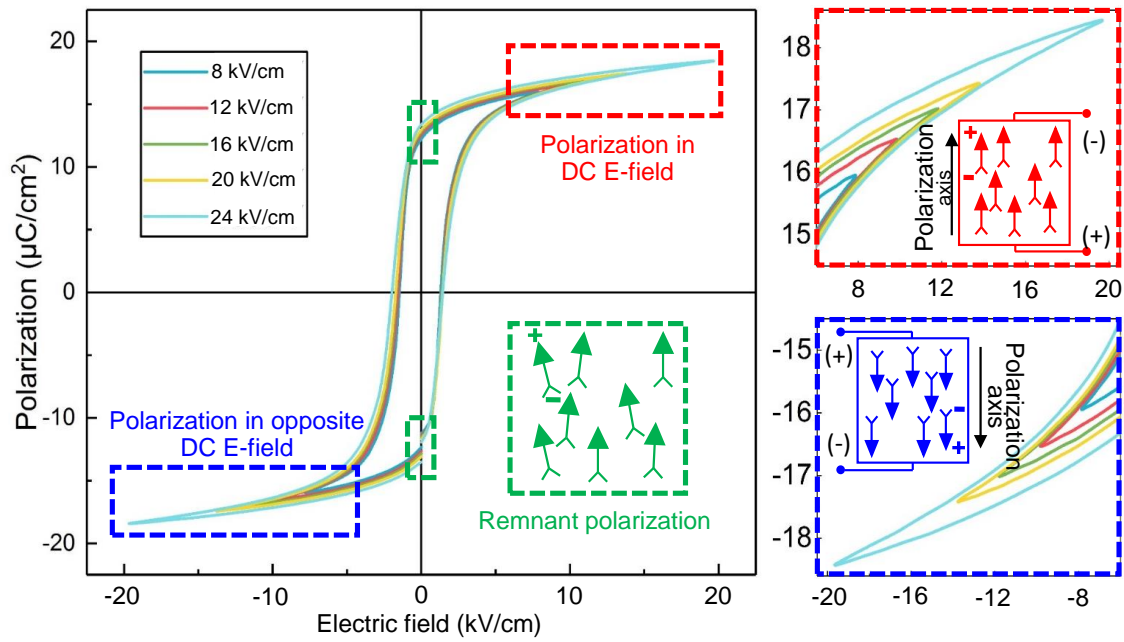
Supplementary Fig. 42. Photographs of the Cu serpentine patterns with different widths. The resolution of the laser ablation machine for 20 μm thick Cu foil is determined to be 45 μm.



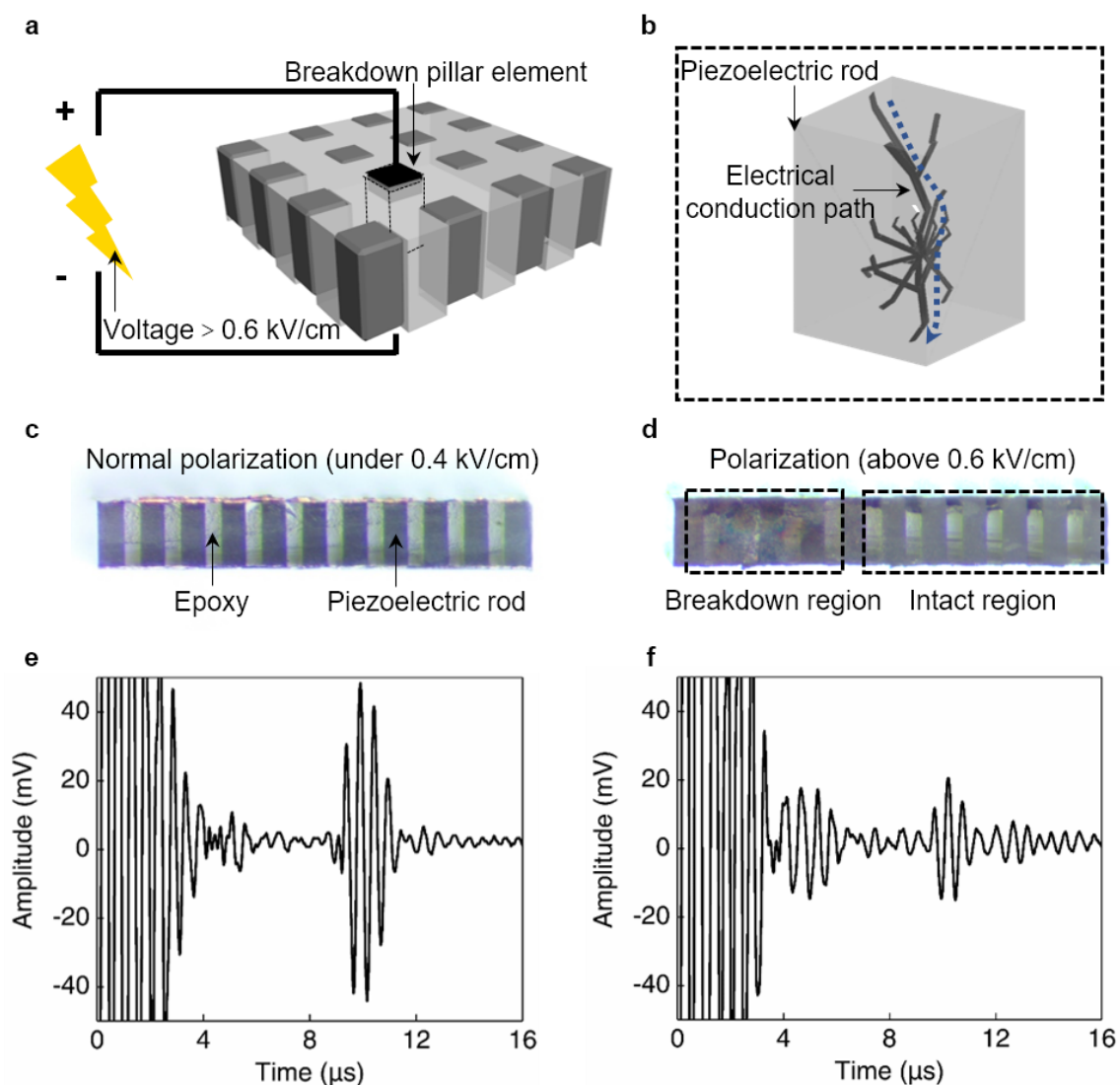
Supplementary Fig. 43. Relationship between Ecoflex thickness and spin speed on a glass slide. The experiment is carried out at room temperature, and all Ecoflex spin coating processes are performed with roughly the same viscosity.



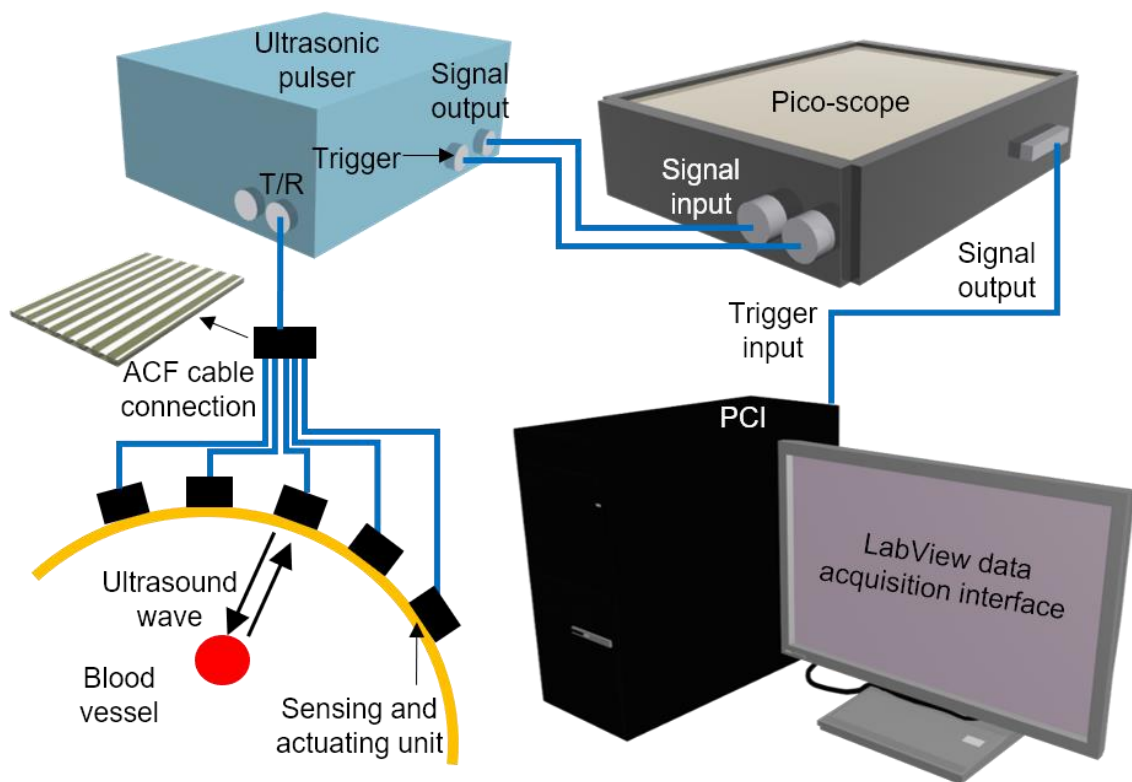
Supplementary Fig. 44. Photographs of the Cu pattern (a) before and (b) after surface oxide removal using flux. The oxide will create a barrier for forming interfacial alloy of Cu and solder paste, leading to weak bonding.



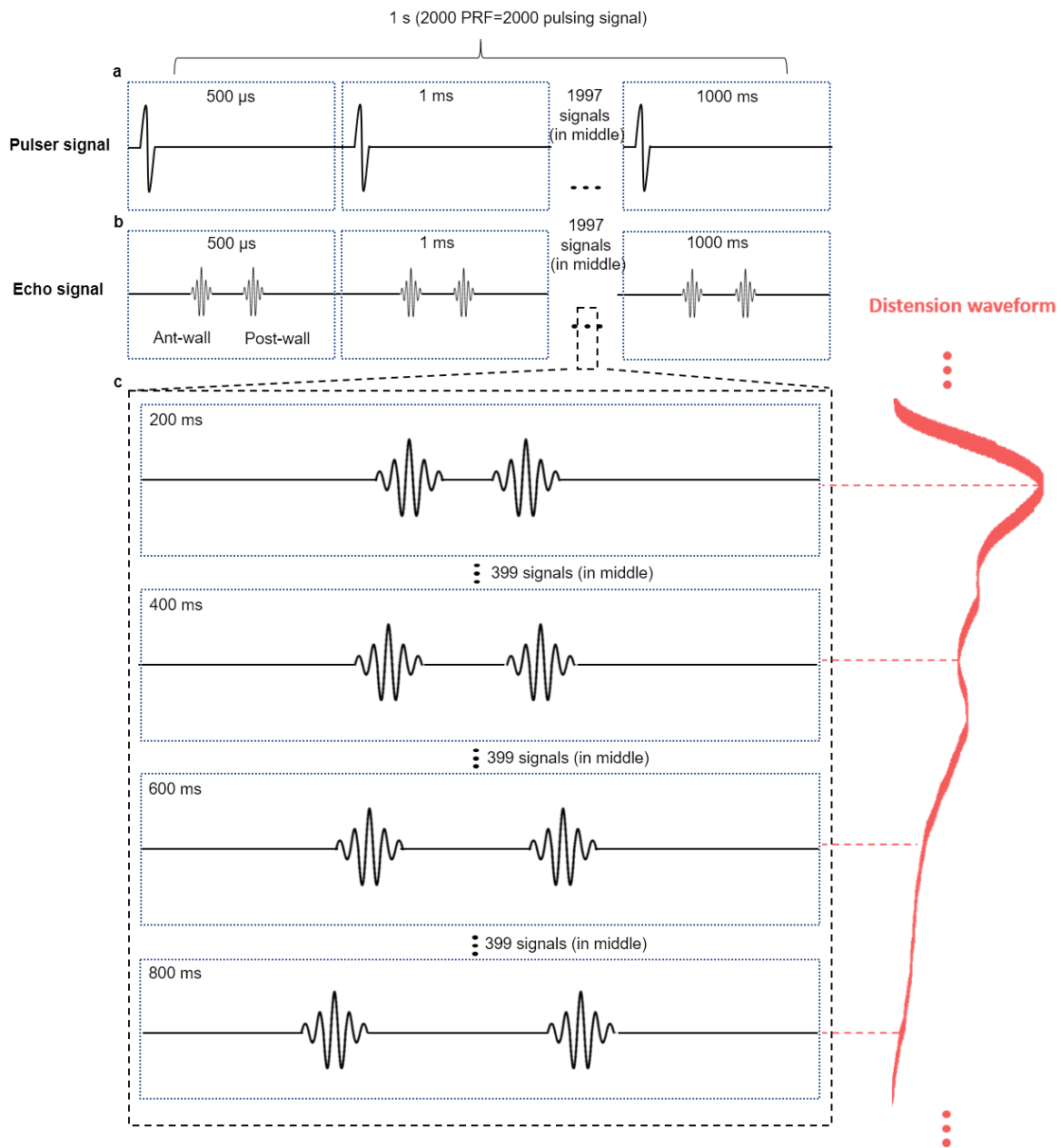
Supplementary Fig. 45. The polarization hysteresis loop, illustrating the switchable dipole alignment of the piezoelectric materials under an electrical field. The dipoles are better aligned with a stronger electrical field. However, the piezoelectric material would break down if the electrical field goes over a threshold.



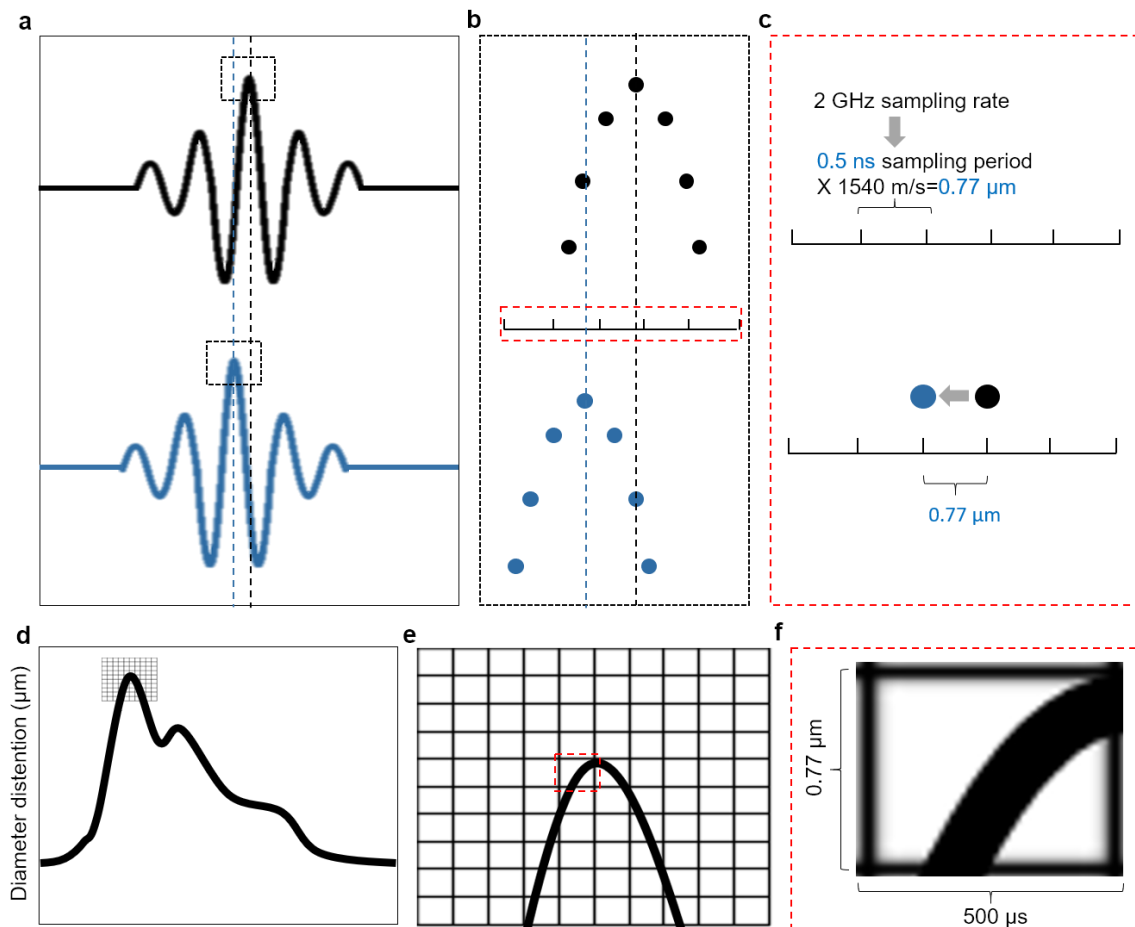
Supplementary Fig. 46. Acoustic emission performance comparison between normal polarization and breakdown. (a) Illustration of the polarization setup. (b) Schematics to show the existence of an electrical conduction path caused by breakdown. (c) The cross section view of an intact 1-3 composite under 800 V polarization. (d) The cross-sectional view of a broken-down 1-3 composite under 1200 V. Reflected signals from devices made of (e) an adequately polarized 1-3 composite and (f) a broken-down 1-3 composite, showing a smaller amplitude caused by the broken-down region.



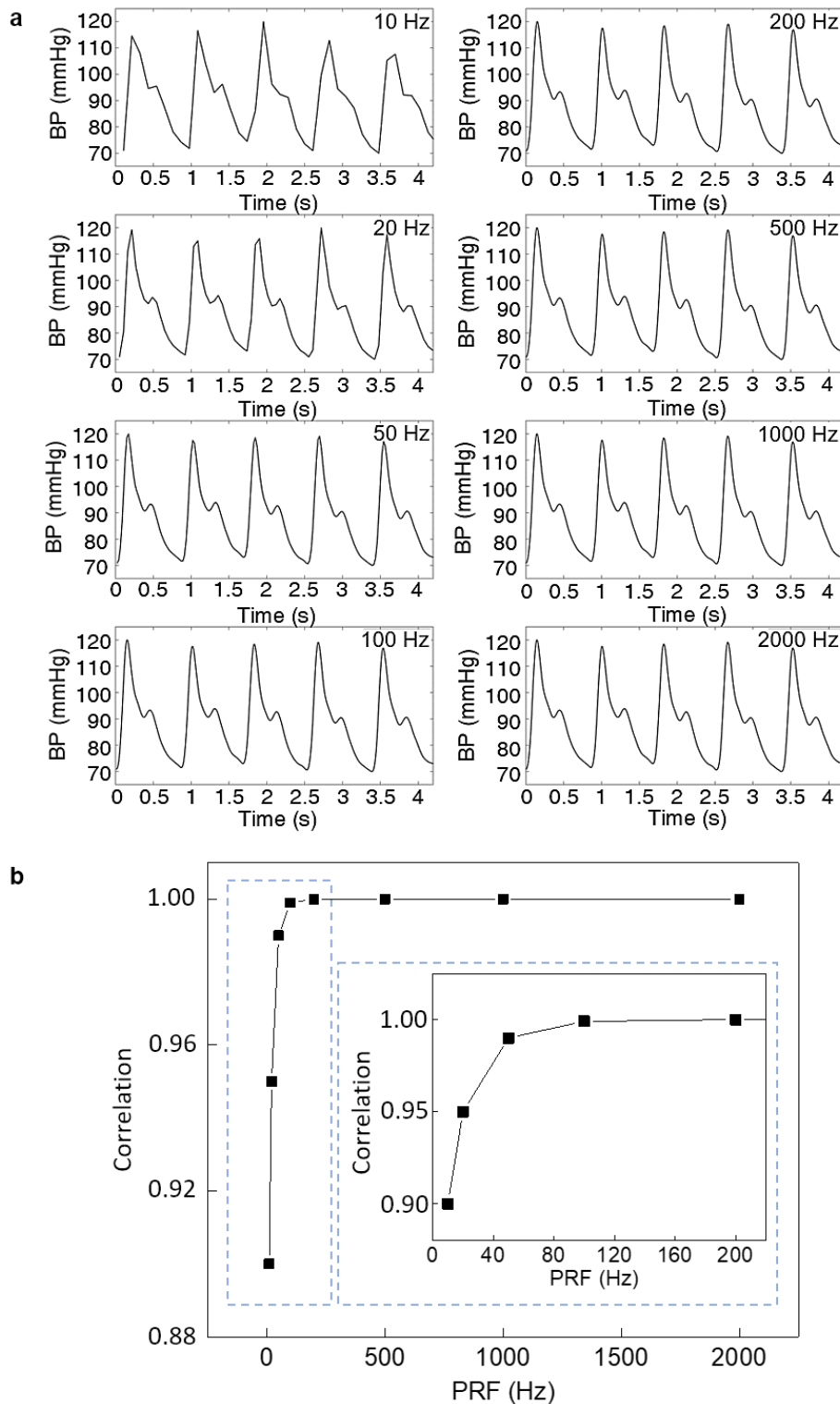
Supplementary Fig. 47. The experimental setup for BP measurement. All of the backend data processing electronics can potentially be miniaturized and integrated with the front-end sensor on the human skin.



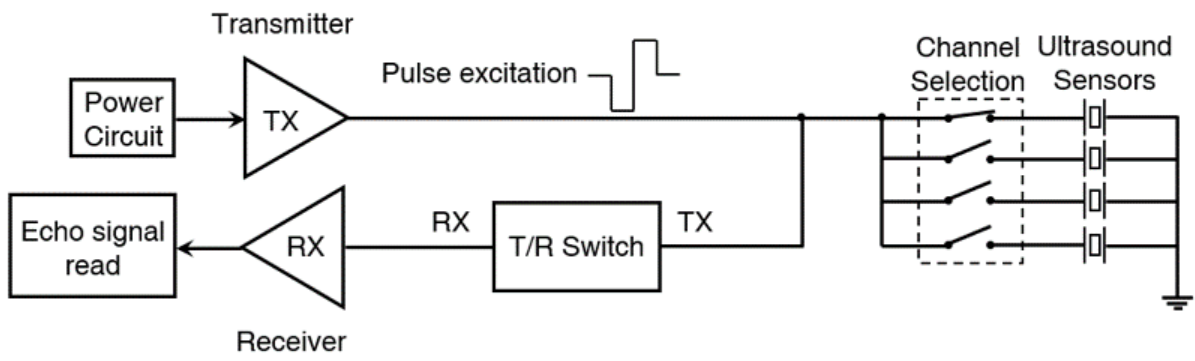
Supplementary Fig. 48. Schematic illustration of the activating and receiving signals during the wall-tracking process. (a) High-frequency activating signals. The PRF adopted is 2000 Hz, which means there are 2000 identical activating signals generated in one second. (b) Echo signals received at the receiver. Each signal has two peaks indicating the locations of the anterior-wall and posterior-wall of the blood vessel. The receiver will receive 2000 echo signals. (c) Four snapshots of signals (at 200 ms, 400 ms, 600 ms, and 800 ms) corresponding to four locations in the BP waveform on the right. The peaks of the signal will shift due to the distension of the blood vessel.



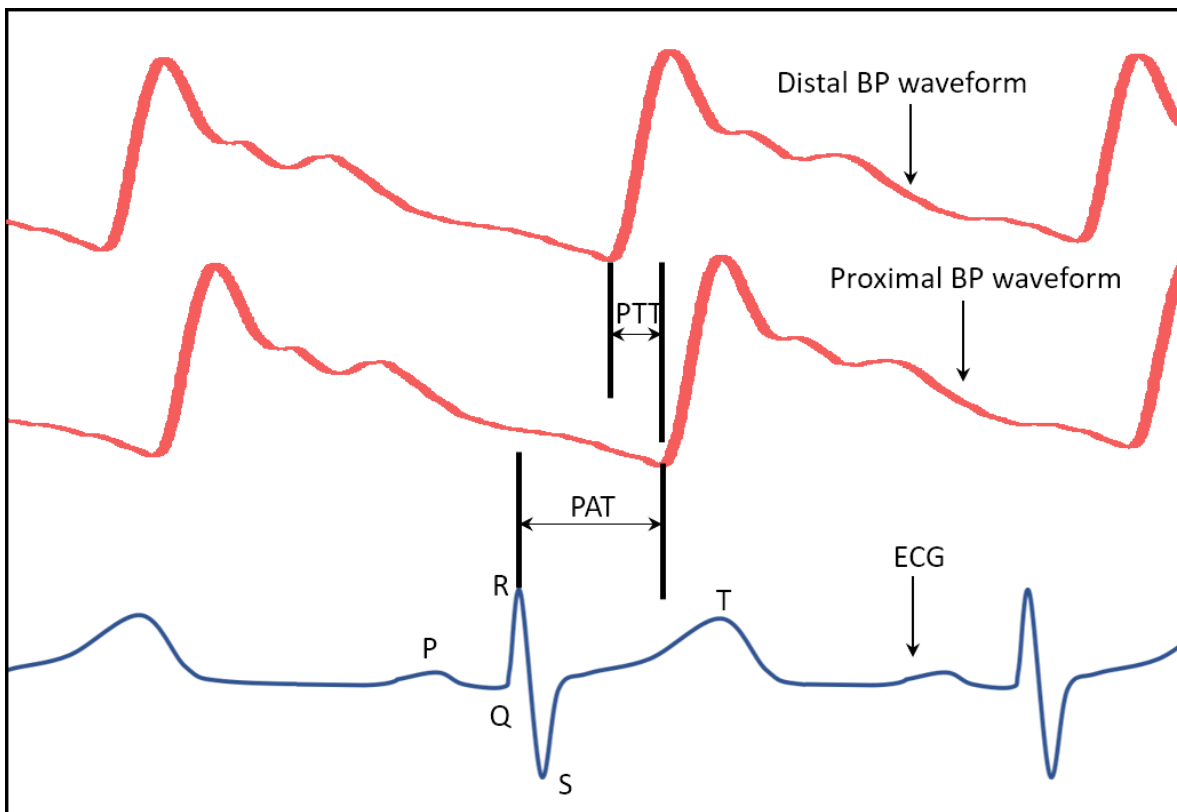
Supplementary Fig. 49. Schematic illustration of the vessel wall-tracking system designed in this work. (a) Schematics of the shifting echo signals in the time domain. (b) The zoomed-in view of the echo signal, showing the analysis is based on the shifting of the data points. (c) Sampling rate calculation to determine the actual spatial resolution. (d), (e), and (f) illustrate the sampling process in both spatial and temporal perspectives. (d) The BP waveform sampling process. (e) The zoomed-in view of (d) for sampling the systolic peak. The horizontal grid represents the temporal resolution. The vertical grid represents the axial resolution. (f) The zoomed-in view of (e), showing the actual spatial and temporal resolutions are 0.77 μm and 500 μs, respectively.



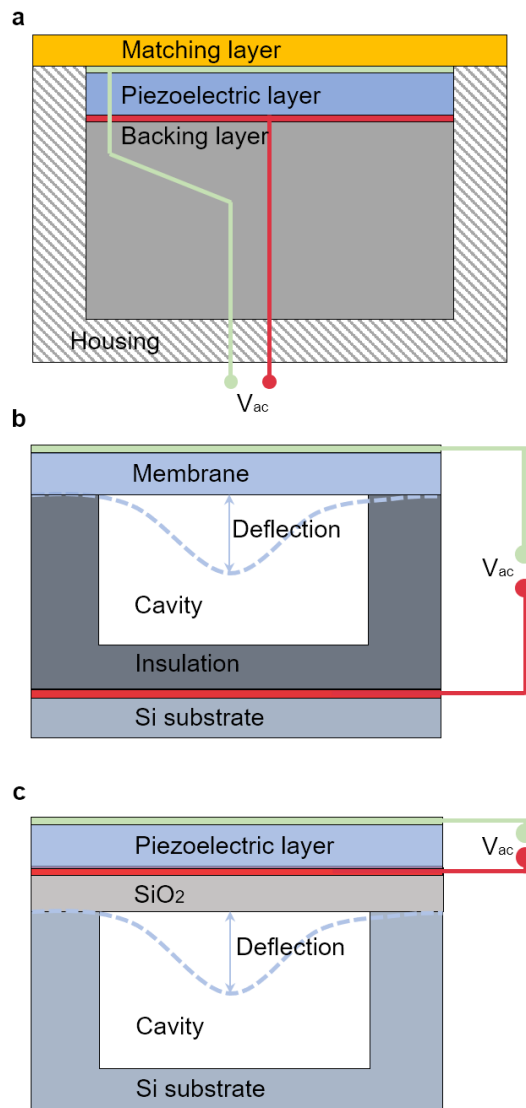
Supplementary Fig. 50. Influence of the PRF on BP waveform morphology. (a) BP waveforms with 10, 20, 50, 100, 200, 1000, and 2000 Hz PRFs, respectively. **(b)** Correlation of the BP waveform with different PRFs with the best measurement at 5000 Hz.



Supplementary Fig. 51. The circuit diagram for multi-channel sensing. The circuit allows multichannel, simultaneous, and continuous measurements of the pulse pressures from different body parts.



Supplementary Fig. 52. Illustration of the PAT and PTT calculated from ECG and BP waveforms. The PTT and PAT can be calculated from simultaneously measured ECG and BP waveforms. Both PTT and PAT can be used to calculate the PWV.



Supplementary Fig. 53. Schematic illustration of piezoelectric ultrasound transducers (PUTs) and micromachined ultrasound transducers (MUTs). The MUTs family includes capacitive micromachined ultrasound transducers (cMUTs) and piezoelectric micromachined ultrasound transducers (pMUTs). The structural layout of (a) PUTs, (b) cMUTs, and (c) pMUTs.

References

- 1 Mendelson, Y. & Ochs, B. D. Noninvasive pulse oximetry utilizing skin reflectance photoplethysmography. *IEEE Trans. Biomed. Eng.* **35**, 798-805 (1988).
- 2 Hertzman, A. B. The blood supply of various skin areas as estimated by the photoelectric plethysmograph. *Am. J. Physiol. Cell Physiol.* **124**, 328-340 (1938).
- 3 Kamal, A., Harness, J., Irving, G. & Mearns, A. Skin photoplethysmography—a review. *Comput. Methods Programs Biomed.* **28**, 257-269 (1989).
- 4 Maeda, Y., Sekine, M. & Tamura, T. Relationship between measurement site and motion artifacts in wearable reflected photoplethysmography. *J. Med. Syst.* **35**, 969-976 (2011).
- 5 Sanyal, D. & Maji, N. Thermoregulation through skin under variable atmospheric and physiological conditions. *J. Theor. Biol.* **208**, 451-456 (2001).
- 6 Daanen, H., Van de Linde, F., Romet, T. & Ducharme, M. The effect of body temperature on the hunting response of the middle finger skin temperature. *Eur. J. Appl. Physiol.* **76**, 538-543 (1997).
- 7 Gardner-medwin, J., Macdonald, I., Taylor, J., Riley, P. & Powell, R. Seasonal differences in finger skin temperature and microvascular blood flow in healthy men and women are exaggerated in women with primary Raynaud's phenomenon. *Br. J. Clin. Pharmacol.* **52**, 17-23 (2001).
- 8 Cowie, B. The cardiac patients perception of his heart attack. *Soc. Sci. Med.* **10**, 87-96 (1976).
- 9 Xing, X. & Sun, M. Optical blood pressure estimation with photoplethysmography and FFT-based neural networks. *Biomed. Opt. Express.* **7**, 3007-3020 (2016).
- 10 Pogue, B. W. *et al.* Quantitative hemoglobin tomography with diffuse near-infrared spectroscopy: pilot results in the breast. *Radiology* **218**, 261-266 (2001).
- 11 Drabkin, D. L. Spectrophotometric studies XIV. The crystallographic and optical properties of the hemoglobin of man in comparison with those of other species. *J. Biol. Chem.* **164**, 703-723 (1946).
- 12 Terry, S., Eckerle, J., Kornbluh, R., Low, T. & Ablow, C. Silicon pressure transducer arrays for blood-pressure measurement. *Sensors and Actuators A: Physical* **23**, 1070-1079 (1990).
- 13 Pang, C. *et al.* Highly skin-conformal microhairly sensor for pulse signal amplification. *Adv. mater.* **27**, 634-640 (2015).
- 14 Zhou, Q., Lam, K. H., Zheng, H., Qiu, W. & Shung, K. K. Piezoelectric single crystal ultrasonic transducers for biomedical applications. *Prog. Mater. Sci.* **66**, 87-111 (2014).
- 15 Akasheh, F., Myers, T., Fraser, J. D., Bose, S. & Bandyopadhyay, A. Development of piezoelectric micromachined ultrasonic transducers. *Sens. Actuators. A Phys.* **111**, 275-287 (2004).
- 16 Ladabaum, I., Jin, X., Soh, H. T., Atalar, A. & Khuri-Yakub, B. Surface micromachined capacitive ultrasonic transducers. *IEEE Trans. Ultrason. Ferroelectr. Freq. Control.* **45**, 678-690 (1998).
- 17 Baborowski, J., Ledermann, N. & Muralt, P. in *Proceedings of IEEE*. 1051-1054 (IEEE, 2004).
- 18 Lee, J. *et al.* Targeted cell immobilization by ultrasound microbeam. *Biotechnol. Bioeng.* **108**, 1643-1650 (2011).
- 19 Soh, H., Ladabaum, I., Atalar, A., Quate, C. & Khuri-Yakub, B. Silicon micromachined ultrasonic immersion transducers. *Appl. Phys. Lett.* **69**, 3674-3676 (1996).
- 20 Qiu, Y. *et al.* Piezoelectric micromachined ultrasound transducer (PMUT) arrays for integrated sensing, actuation and imaging. *Sensors* **15**, 8020-8041 (2015).
- 21 Mills, D. M. in *Ultrasonics Symposium, IEEE*. 384-390 (IEEE, 2004).
- 22 Khuri-Yakub, B. T. & Oralkan, Ö. Capacitive micromachined ultrasonic transducers for medical imaging and therapy. *J. Micromech. Microeng.* **21**, 054004 (2011).
- 23 Bayram, B., Hæggstrom, E., Yaralioglu, G. G. & Khuri-Yakub, B. T. A new regime for operating capacitive micromachined ultrasonic transducers. *IEEE Trans. Ultrason. Ferroelectr. Freq. Control.* **50**, 1184-1190 (2003).

- 24 Akasheh, F., Fraser, J. D., Bose, S. & Bandyopadhyay, A. Piezoelectric micromachined ultrasonic transducers: Modeling the influence of structural parameters on device performance. *IEEE Trans. Ultrason. Ferroelectr. Freq. Control.* **52**, 455-468 (2005).
- 25 Qiu, Y. *et al.* Piezoelectric Micromachined Ultrasound Transducer (PMUT) Arrays for Integrated Sensing, Actuation and Imaging. *Sensors* **15**, 8020-8041 (2015).
- 26 Chang, M.-W., Deng, H.-C., Pang, D.-C. & Chen, M.-Y. in *Ultrasonics Symposium, IEEE.* 527-530 (IEEE, 2007).
- 27 Joshi, S., Yazadi, S., Henneken, V., Dekker, R. & Sanders, R. in *Conference of Electronics Packaging and Technology Conference (EPTC), IEEE.* 1-4 (IEEE, 2015).
- 28 Singh, R. *et al.* *Acoustical Imaging* (Springer, 2011).
- 29 Caronti, A. *et al.* in *Ultrasonics Symposium, IEEE.* 2092-2095 (IEEE, 2008).
- 30 Zhuang, X., Lin, D.-S., Oralkan, Ö. & Khuri-Yakub, B. T. Fabrication of flexible transducer arrays with through-wafer electrical interconnects based on trench refilling with PDMS. *J. Microelectromech. Syst.* **17**, 446-452 (2008).
- 31 Zhuang, X., Lin, D.-S., Oralkan, O. & Khuri-Yakub, B. T. in *Conference of Micro Electro Mechanical Systems, IEEE.* 73-76 (IEEE, 2007).
- 32 Kim, D.-H. *et al.* Epidermal Electronics. *Science* **333**, 838-843, (2011).
- 33 Casula, O., Poidevin, C., Cattiaux, G. & Dumas, P. Control of complex components with smart flexible phased arrays. *Ultrasonics* **44**, e647-e651 (2006).
- 34 Bowen, C., Bradley, L., Almond, D. & Wilcox, P. Flexible piezoelectric transducer for ultrasonic inspection of non-planar components. *Ultrasonics* **48**, 367-375 (2008).
- 35 Pickering, T. G., Shimbo, D. & Haas, D. Ambulatory blood-pressure monitoring. *N. Engl. J. Med.* **354**, 2368-2374 (2006).
- 36 Kim, D.-H. *et al.* Dissolvable films of silk fibroin for ultrathin conformal bio-integrated electronics. *Nat. Mater.* **9**, 511-517 (2010).
- 37 Kim, C.-S., Carek, A. M., Mukkamala, R., Inan, O. T. & Hahn, J.-O. Ballistocardiogram as proximal timing reference for pulse transit time measurement: Potential for cuffless blood pressure monitoring. *IEEE Trans. Biomed. Eng.* **62**, 2657-2664 (2015).
- 38 Mukkamala, R. *et al.* Toward ubiquitous blood pressure monitoring via pulse transit time: theory and practice. *IEEE Trans. Biomed. Eng.* **62**, 1879-1901 (2015).
- 39 Milne, L. *et al.* Central aortic blood pressure from ultrasound wall-tracking of the carotid artery in children: comparison with invasive measurements and radial tonometry. *Hypertension* **65**, 1141-1146 (2015).
- 40 Shau, Y.-W., Wang, C.-L., Shieh, J.-Y. & Hsu, T.-C. Noninvasive assessment of the viscoelasticity of peripheral arteries. *Ultrasound Med. Biol.* **25**, 1377-1388 (1999).
- 41 Arndt, J. O., Klauske, J. & Mersch, F. The diameter of the intact carotid artery in man and its change with pulse pressure. *Pflugers Arch Gesamte Physiol. Menschen Tiere* **301**, 230-240 (1968).
- 42 Valdez-Jasso, D. *et al.* Linear and nonlinear viscoelastic modeling of aorta and carotid pressure–area dynamics under in vivo and ex vivo conditions. *Ann. Biomed. Eng.* **39**, 1438-1456 (2011).
- 43 Kitakule, M. M. & Mayo, P. Use of ultrasound to assess fluid responsiveness in the intensive care unit. *Open Crit. Care Med. J.* **3**, 33-37 (2010).
- 44 Lyon, M. & Verma, N. Ultrasound guided volume assessment using inferior vena cava diameter. *Open. Emerg. Med. J.* **3**, 22-24 (2010).
- 45 Lipton, B. Estimation of central venous pressure by ultrasound of the internal jugular vein. *Am. J. Emerg. Med.* **18**, 432-434 (2000).
- 46 Keller, A. S. *et al.* Diagnostic accuracy of a simple ultrasound measurement to estimate central venous pressure in spontaneously breathing, critically ill patients. *J. Hosp. Med.* **4**, 350-355 (2009).
- 47 Donahue, S. P., Wood, J. P., Patel, B. M. & Quinn, J. V. Correlation of sonographic measurements of the internal jugular vein with central venous pressure. *Am. J. Emerg. Med.* **27**, 851-855 (2009).

- 48 Albright, B. *et al.* in *A1663 ASA Annual Meeting*.
- 49 Ogum, C., Hariharan, S. & Chen, D. Non-invasive central venous pressure estimation by ultrasound-guided internal jugular vein cross-sectional area measurement. *Biomed. Phys. Eng. Express* **2**, 025004 (2016).
- 50 Meinders, J. M. & Hoeks, A. P. Simultaneous assessment of diameter and pressure waveforms in the carotid artery. *Ultrasound Med. Biol.* **30**, 147-154 (2004).
- 51 Instrumentation, A. f. t. A. o. M. American national standard. Manual, electronic or automated sphygmomanometers. *ANSI/AAMI SP10-2002/A1* (2003).
- 52 Arumugam, V., Naresh, M. & Sanjeevi, R. Effect of strain rate on the fracture behaviour of skin. *J. Biosci. Med.* **19**, 307-313 (1994).
53. http://www.smartmedical.co.uk/images/Upload/Product_Literature/Atcor/SphygmoCor_CPV.pdf
- 54 <https://www.mdfinstruments.com/mdf-calibra-pro-sphygmomanometer-double-bellow>.
- 55 <https://physics.nist.gov/cuu/Uncertainty/typea.html>.
- 56 Farrance, I. & Frenkel, R. Uncertainty of measurement: a review of the rules for calculating uncertainty components through functional relationships. *Clin. Biochem. Rev.* **33**, 49-75 (2012).
- 57 [http://www.atcormedical.com.au/download/Active/Research_Manual_\(CVMS\).pdf](http://www.atcormedical.com.au/download/Active/Research_Manual_(CVMS).pdf).
- 58 O'Brien, E. *et al.* The British Hypertension Society protocol for the evaluation of blood pressure measuring devices. *J. Hypertens.* **11**, S43-S62 (1993).
- 59 Lyons, T. J. *et al.* Analysis of mission and aircraft factors in G-induced loss of consciousness in the USAF: 1982-2002. *Aviat. Space Environ. Med.* **75**, 479-482 (2004).
- 60 Chambers, D., Huang, C. & Matthews, G. *Basic physiology for anaesthetists*. (Cambridge Univ. Press, 2015).
- 61 Brath, P. C. Atlas of Cardiovascular Monitoring. *Anesthesiology: Am. J. Soc. Anesthesiol.* **93**, 312-312 (2000).
- 62 Agabiti-Rosei, E. *et al.* Central blood pressure measurements and antihypertensive therapy: a consensus document. *Hypertension* **50**, 154-160 (2007).
- 63 Elgendi, M. On the analysis of fingertip photoplethysmogram signals. *Curr. Cardiol. Rev.* **8**, 14-25 (2012).
- 64 Amelard, R. *et al.* Non-contact hemodynamic imaging reveals the jugular venous pulse waveform. *Sci. Rep.* **7**, 40150 (2017).
- 65 Camacho, F., Avolio, A. & Lovell, N. Estimation of pressure pulse amplification between aorta and brachial artery using stepwise multiple regression models. *Physiol. Meas.* **25**, 879-889 (2004).
- 66 McEniery, C. M. *et al.* Normal vascular aging: differential effects on wave reflection and aortic pulse wave velocity: the Anglo-Cardiff Collaborative Trial (ACCT). *J. Am. Coll. Cardiol.* **46**, 1753-1760 (2005).
- 67 Wilkinson, I. B. *et al.* Heart rate dependency of pulse pressure amplification and arterial stiffness. *Am. J. Hypertens.* **15**, 24-30 (2002).
- 68 Albaladejo, P. *et al.* Heart rate, arterial stiffness, and wave reflections in paced patients. *Hypertension* **38**, 949-952 (2001).
- 69 Williams, B. *et al.* Differential impact of blood pressure-lowering drugs on central aortic pressure and clinical outcomes: principal results of the Conduit Artery Function Evaluation (CAFE) study. *Circulation* **113**, 1213-1225 (2006).
- 70 McEniery, C. M., Cockcroft, J. R., Roman, M. J., Franklin, S. S. & Wilkinson, I. B. Central blood pressure: current evidence and clinical importance. *Eur. Heart J.* **35**, 1719-1725 (2014).
- 71 Xu, S. *et al.* Soft microfluidic assemblies of sensors, circuits, and radios for the skin. *Science* **344**, 70-74 (2014).
- 72 Wibmer, T. *et al.* Pulse transit time and blood pressure during cardiopulmonary exercise tests. *Physiol. Res.* **63**, 287-296 (2014).
- 73 Thomas, J. A method for continuously indicating blood pressure. *J. Physiol.* **129**, 75-76 (1955).
- 74 Steptoe, A., Smulyan, H. & Gribbin, B. Pulse wave velocity and blood pressure change:

calibration and applications. *Psychophysiology* **13**, 488-493 (1976).